NUCLEATION, GROWTH, AND ETCHING OF NOBLE-METAL NANOCRYSTALS

A Dissertation
Presented to
The Academic Faculty

by

Aleksey Ruditskiy

In Partial Fulfillment
of the Requirements for the Degree
of Doctor of Philosophy in the
School of Chemistry and Biochemistry

Georgia Institute of Technology
August, 2017

NUCLEATION, GROWTH, AND ETCHING OF NOBLE-METAL NANOCRYSTALS

Approved by:

Dr. Younan Xia, Advisor
Department of Biomedical Engineering
Georgia Institute of Technology

Dr. Angus P. Wilkinson
School of Chemistry and Biochemistry
Georgia Institute of Technology

Dr. Z. John Zhang
School of Chemistry and Biochemistry
Georgia Institute of Technology

Dr. Joseph Sadighi
School of Chemistry and Biochemistry
Georgia Institute of Technology

Dr. Michael Filler
School of Chemical and Biomolecular Engineering
Georgia Institute of Technology

Date Approved: April 27, 2017

Dedicated to my parents, Remualda Lebedeva and Mark Ruditskiy, for their love, endless support, and encouragement.

ACKNOWLEDGEMENTS

This has been a long and challenging journey, and now that I stand at its terminus I owe thanks to many. First and foremost, I would like express my deepest gratitude to my advisor, Professor Younan Xia, for his many years of guidance. I have certainly learned much from this experience. I would also like to thank Professors Joseph Sadighi, Angus Wilkinson, John Zhang, and Michael Filler for serving on my dissertation committee. Thank you for all of your support and advice.

My special thanks go to Dr. Hsin-Chieh Peng and Professor Sang-Il Choi, who generously shared their time and experience over the years, particularly in the early days of my studies. Similarly, I am grateful to Madeline Vara, Legna Figueroa-Cosme, and Kyle D. Gilroy for being terrific friends and coworkers. I can attest that there were many days when my sanity remained intact because of them. I am thankful for the support provided by many people at Georgia Tech: Professor Dong Qin, Dr. Wenying Liu, Dr. Bo Pang, Dr. Hongwen Huang, Dr. Xue Wang, Zachary Hood, and many other current and former members of the Xia group, who have helped me tremendously during my dissertation study.

Although this dissertation is dedicated to them, they deserve to be recognized again. I sincerely express my deepest gratitude to my parents, Remualda Lebedeva and Mark Ruditskiy for their endless love and support. Without them I literally would not be around to write these words.

TABLE OF CONTENTS

LIST OF TABLES

Page

LIST OF FIGURES

LIST OF SYMBOLS AND ABBREVIATIONS

A	precursor concentration
AA	ascorbic acid
CN	coordination number
CV	cyclic voltammogram
d	size of decahedral nanocrystal
DEG	diethylene glycol
DFAFC	direct formic acid fuel cell
DFT	density functional theory
Dh	decahedral
DI	deionized
ECSA	electrochemical surface area
EDX	energy dispersive X-ray
EG	ethylene glycol
FAO	formic acid oxidation
fcc	face-centered cubic

FT	Fourier transform
j	the observed current density
JCPDS	joint committee on powder diffraction standards
HAADF	high-angle annular dark-field
HRTEM	high-resolution transmission electron microscopy
ICP-MS	inductively-coupled plasma mass spectrometry
k	rate constant
K_{sp}	solubility product constant
LSPR	localized surface plasmon resonance
MBY	2-methyl-3-butyn-2-ol
MBE	2-methyl-3-buten-2-ol
MBA	2-methyl-3-butan-2-ol
ORR	oxygen reduction reaction
PVP	poly(vinyl pyrrolidone)
RHE	reversible hydrogen electrode
r_o	initial reduction rate
$R_{deposition}$	rate of atomic deposition

$R_{diffusion}$	rate of atomic surface diffusion
SERS	surface-enhanced Raman scattering
STEM	scanning transmission electron microscopy
t	time
TEM	transmission electron microscopy
UPD	underpotential deposition
UV-vis	ultraviolet-visible
XPS	X-ray photoelectron spectroscopy
XRD	X-ray diffraction
γ	specific surface free energy

SUMMARY

Colloidal noble-metal nanocrystals have tremendous potential in applications ranging from medicine to sensing to catalysis. The ultimate utility of these nanomaterials relies on our ability to precisely control their size, shape, and structure, since many of the relevant physiochemical properties emerge as a consequence of these parameters. This dissertation is focused on the roles of nucleation and growth processes in noble-metal nanocrystal synthesis, guided by kinetic considerations and the presence of appropriate capping agents, as well as the impact of oxidative etching. I begin by demonstrating the synthesis of well-defined Ag nanocubes with sub-15 nm edge lengths, achieved through the overgrowth of Ag_2S clusters coupled with the capping of the {100} facets by Br^- ions. In the second project, I conduct a quantitative analysis of the synthesis of Pd decahedra in order to ascertain the impacts of reduction kinetics and post-nucleation coalescence process on the formation and growth of the decahedral nanocrystals, respectively, and in an attempt to maximize both the precursor conversion and morphology yields. With the insights gained during this study, I proceed to demonstrate the synthesis of Pd penta-twinned nanowires, achieved through a combination of precisely tuned reduction kinetics and the capping of {100} facets by I^- ions. Finally, I carry out a systematic study to understand the impact of oxidative etching by the O_2/I^- pair on the morphology of Pd decahedral nanocrystals. The mechanistic understanding achieved in this dissertation helps lay the foundation for the rational design and deterministic synthesis of nanocrystals with desired and controlled size, shapes, and structures.

CHAPTER 1

INTRODUCTION

1.1 Overview of Noble-Metal Nanocrystals and Their Applications

Noble-metal nanocrystals have been extensively explored for many decades due to their use in a plethora of applications related to catalysis [1−4], electronics [5−8], photonics [9−12], information storage [13−15], energy conversion/storage [16−18], environmental protection [19, 20], and medicine [21−24]. Due to the extremely low abundance of these metals in the Earth's crust and their consequently high prices, there is a pressing need to develop more efficient methods for utilizing them. In recent years, a number of strategies have been demonstrated for the efficient utilization of noble-metals, focusing primarily on shaping them into nanocrystals with extensive control over their size, shape, and internal twin structure.

The hallmark of nanotechnology is not only the access to small sizes but more importantly the size-and-shape dependent physicochemical properties [25]. Several novel features will arise when bulk metals are transformed into nanocrystals, including a drastically increased specific surface area, a higher density of lowly-coordinated surface atoms, quantum-size effects, the emergence of localized surface plasmon resonance (LSPR), changes to phase-stability, and novel magnetic phenomena such as superparamagnetism. While the effects of nano encompass all materials, the prototypical example of size-dependent physicochemical properties can be found in Au, a classically inert bulk material. When the dimensions of Au are reduced down to the nanoscale, interesting effects arise that have led to the discovery of extraordinary catalytic activity for low-temperature oxidation of carbon monoxide [26] and the hydrochlorination of acetylene to vinyl chloride [27]. Changing concurrently with the catalytic effectiveness are the optical properties. Au nanocrystals with sizes below 100 nm readily absorb visible light

and give rise to an intense localized surface plasmon resonance. If the Au nanocrystal is further reduced in size to a scale comparable to the Fermi wavelength of Au (~0.5 nm), the electronic structure becomes discretized and photoluminescence is observed. These novel properties have led to innovative applications, including those related to drug delivery and cancer theranostics, plasmonically enhanced chemistry, plasmonic nanocrystal solar cells and a wide variety of sensing modalities.

Over the past decade, focus has shifted from syntheses aimed at size control to those centered on simultaneous size and shape control. Nanocrystals with a well-defined shape provides a means to access the shape-dependent (or facet-dependent) catalytic properties. For example, research has progressed to the point where it is now feasible to produce highly uniform nanocrystals with great shape or facet specificity (*e.g.*, nanocubes with all {100} facets, octahedra with all {111} facets, or shapes with an intermediate cuboctahedral shape and varying ratios of {100} to {111} facets). Their implementation as catalysts has led to the overwhelming observation that catalytic performance is closely tied to the coordination and spatial arrangement of atoms at the surface, largely defined by the expressed facets. Sun and co-workers demonstrated that well-defined Pt tetrahexahedra nanocrystals, enclosed by 24 high-index facets such as {730}, {210} and/or {520}, showed more than four-fold enhancement for the electro-oxidation of small organic fuels such as formic acid and ethanol as compared to Pt nanospheres and commercial Pt/C catalysts [28]. The type of facet can also give rise to improved catalytic selectivity. For example, Somorjai and co-workers demonstrated that the hydrogenation of benzene on Pt nanocrystals covered by {111} facets resulted in the formation of both cyclohexane and cyclohexene while those enclosed by {100} facets generated solely cyclohexene [29]. As another means of control, selectivity can also be tuned by controlling the population of surface atoms that have low coordination numbers, which is characteristic of edges, corners, and vertices. This concept was demonstrated by Kiwi-Minsker and co-workers, who used uniform Pd nanocrystals with cubic, octahedral, and cuboctahedral shapes to study the hydrogenation of 2-methyl-

3-butyn-2-ol (MBY) [30]. They found that semi-hydrogenation to 2-methyl-3-buten-2-ol (MBE) occurred on both the {100} and {111} facets, whereas over hydrogenation to 2-methyl-3-butan-2-ol (MBA) mainly occurred at the edge sites. From these few examples, it is clear that advances in synthetic control has ultimately led the discovery of very fundamental atomic-scale structure-function relationships.

These and many other examples clearly illustrate the critical importance of shape control to the effective use of noble-metal nanocrystals in a wide variety of applications. Thanks to the efforts of many research groups, the past decade has witnessed spectacular advances in the development of methods for the shape-controlled syntheses of colloidal metal nanocrystals [25, 31]. Metal nanocrystals with many distinctive shapes can now be readily prepared, with notable examples including two-dimensional (2-D) nanocrystals such as thin plates or prisms with triangular, hexagonal, or circular projections; 1-D nanocrystals such as rods, bars, and wires with circular, square, rectangular or pentagonal cross sections; as well as 0-D nanocrystals such as spheres, spheroids, cubes, cuboctahedrons, octahedrons, tetrahedrons, rhombic dodecahedrons, bipyramids, decahedrons, and icosahedrons. In addition, nanocrystals with concave surfaces, facets of high Miller index (containing indices > 1) or branched arms have also become increasingly common in recent years [32−34].

1.2 Controlling the Lifecycle of a Nanocrystal

The formation of metal nanocrystals can be divided into two major steps: *i*) development of seeds with a specific internal structure through homogeneous nucleation from metal atoms and *ii*) evolution of the seeds into nanocrystals through growth. Figure 1.1 shows the typical seeds available to an face-centered cubic (*fcc*) metal, as well as some of the nanocrystals with diversified shapes. It is worth noting that seeds with the same internal structure can evolve into nanocrystals with different shapes depending on the

capping agent and growth kinetics. For instance, the single-crystal seeds can grow into either cubes or octahedra in

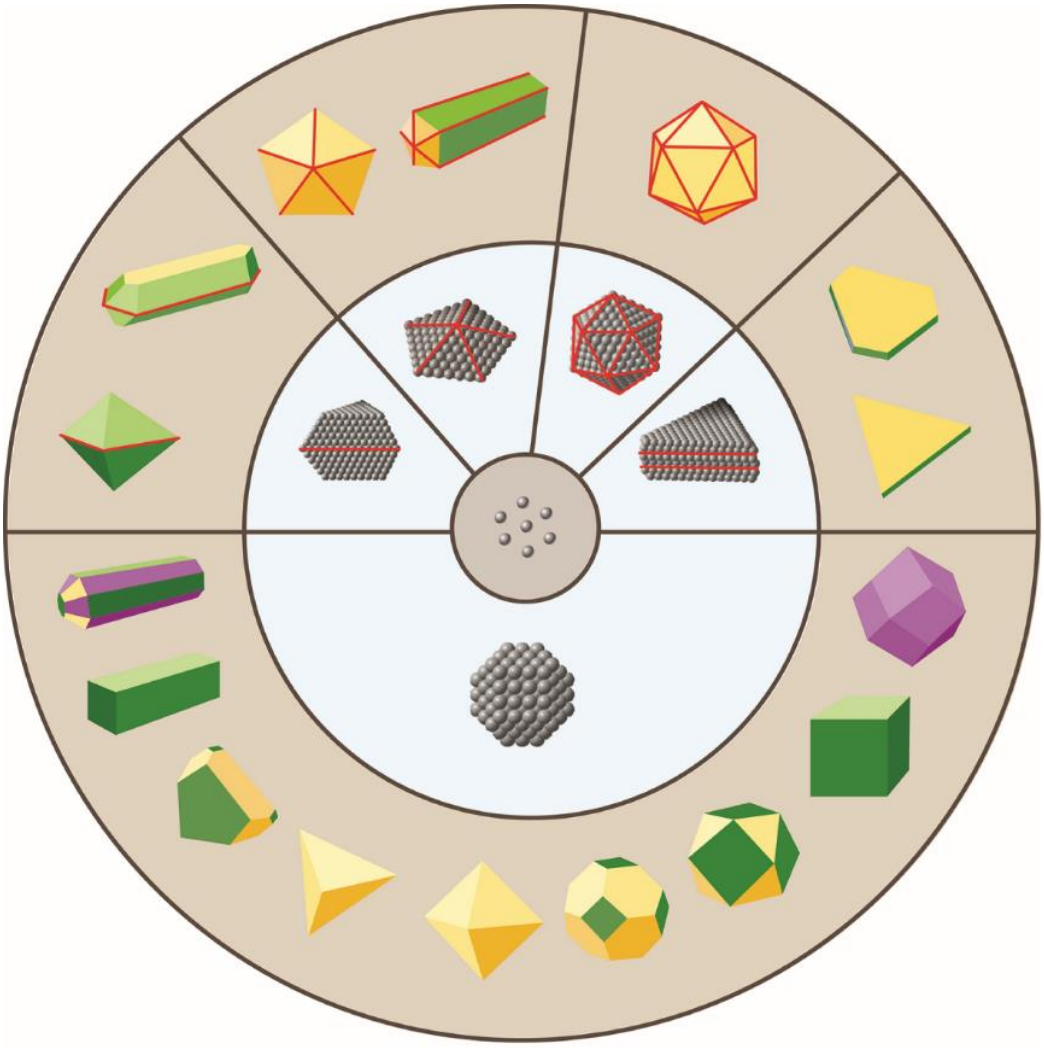

Figure 1.1. Examples of metal nanocrystals with different shapes (the outer ring) and their corresponding seeds with different internal structures (the inner ring). The green, yellow, and purple colors correspond to {100}, {111}, {110} facets, respectively, while the twinned planes are delineated by red lines. (Reprinted with permission from [61]. Copyright 2016 Annual Reviews.)

the presence of capping agents for the {100} and {111} facets, respectively. At a proper reduction rate for the precursor, the cubic symmetry can be broken to generate nanocrystals such as tetrahedra and rectangular or octagonal bars [35, 36]. Concurrently with the growth processes that build-up the nanocrystal through atomic addition, oxidative etching acts to

dissolve its constituent atoms through the interaction of an etchant species with the metal surface. If left unchecked, this mechanism can remove nanocrystal features or dissolve the nanocrystal entirely. However, harnessing the power of oxidative etching can provide a powerful method for shaping nanocrystal morphology, as well as a means of controlling product purity.

1.2.1 Nucleation and the Formation of Seeds

The formation of nanocrystals begins with nucleation—the birth of a new thermodynamic phase in a reaction system. According to a model proposed by LaMer in the 1950's, nucleation can be divided into three major steps: *i*) production of monomers or building blocks for the nanocrystals, *ii*) rapid aggregation of the monomers into nuclei, and *iii*) growth of the nuclei into seeds [37]. For metal nanocrystals, the monomers are typically zero-valent atoms produced *via* the reduction or decomposition of a precursor. As the atoms steadily grow in concentration and reach supersaturation, they will rapidly aggregate to generate nuclei. This process is known as homogenous nucleation, which is driven by the free energy associated with the level of supersaturation, as well as the reaction temperature [38]. The resultant nuclei are composed of just a handful of atoms, and their structure (and thus geometric shape and symmetry) tends to fluctuate over time [25].

While the atomistic detail involved in the formation of seeds remains a poorly understood subject, several methods for experimentally controlling the population of various types of seeds have been developed. On the one hand, the formation of seeds with different internal twin structures can be understood from a thermodynamic perspective [39]. Figure 1.2A shows a typical phase diagram computed for Au seeds as functions of particle size and temperature, suggesting that multiply-twinned and single-crystal seeds are favored at relatively small and large sizes, respectively [40]. On the other hand, it has been recently discovered that the initial reduction rate of a precursor is crucial to the formation of seeds with a particular internal structure in high purity [41]. Specifically, the initial

reduction rates necessary for generating different types of seeds tend to decrease in the order of single-crystal, singly-twinned, multiply-twinned, and stacking-fault-lined. Figure 1.2B shows the percentages of Pd seeds with different internal structures as a function of the initial rate for the reduction of $PdCl_4^{2-}$. Of particular interest is the existence of different ranges of reduction rate, within which the purity of seeds could approach 100%. The reduction rate could be experimentally adjusted by temperature, as well as the type and concentration of reducing agent and precursor involved in the synthesis.

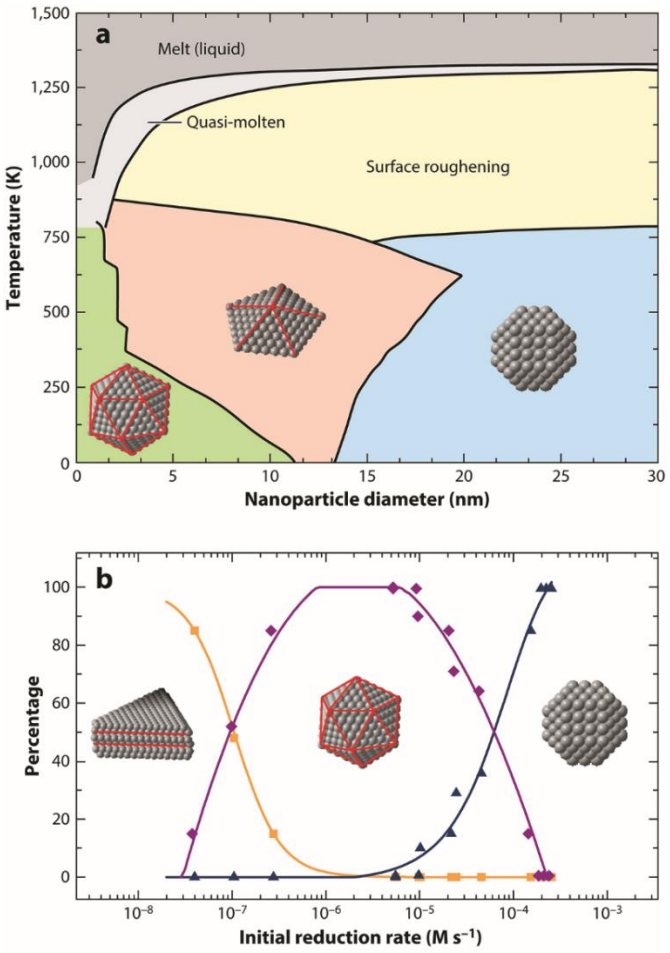

Figure 1.2. Thermodynamic and kinetic approaches to controlling the internal structure of seeds. (A) Phase diagram of Au seeds as functions of temperature and nanoparticle size. (B) Population of Pd nanocrystals as a function of the initial reduction rate. Green data points correspond to plates with stacking faults, black to multiple-twinned icosahedra, and blue to single-crystal cuboctahedra. (Reprinted with permission from [61]. Copyright 2016 Annual Reviews.)

1.2.2 Nanocrystal Growth and the Development of Shape and Structure

The second step in a nanocrystal synthesis involves the growth of the initially formed seeds *via* constant deposition of metal atoms. The evolution of shape can be manipulated through the use of multiple strategies: *i*) addition of a capping agent to selectively bind to a specific type of facet and thus promote the growth of other facets; *ii*) control of the atomic deposition rate relative to the rate of atom diffusion on the surface of a growing nanocrystal; and *iii*) inclusion of oxidative etching to alter the growth rates along different directions. By employing these three approaches separately or together, in conjunction with a tight control over the seeds, it is possible to attain metal nanocrystals with a specific shape and thus a single type of facet on the surface. Figure 1.3 shows transmission electron microscopy images of some example Pd nanocrystals generated through these methods.

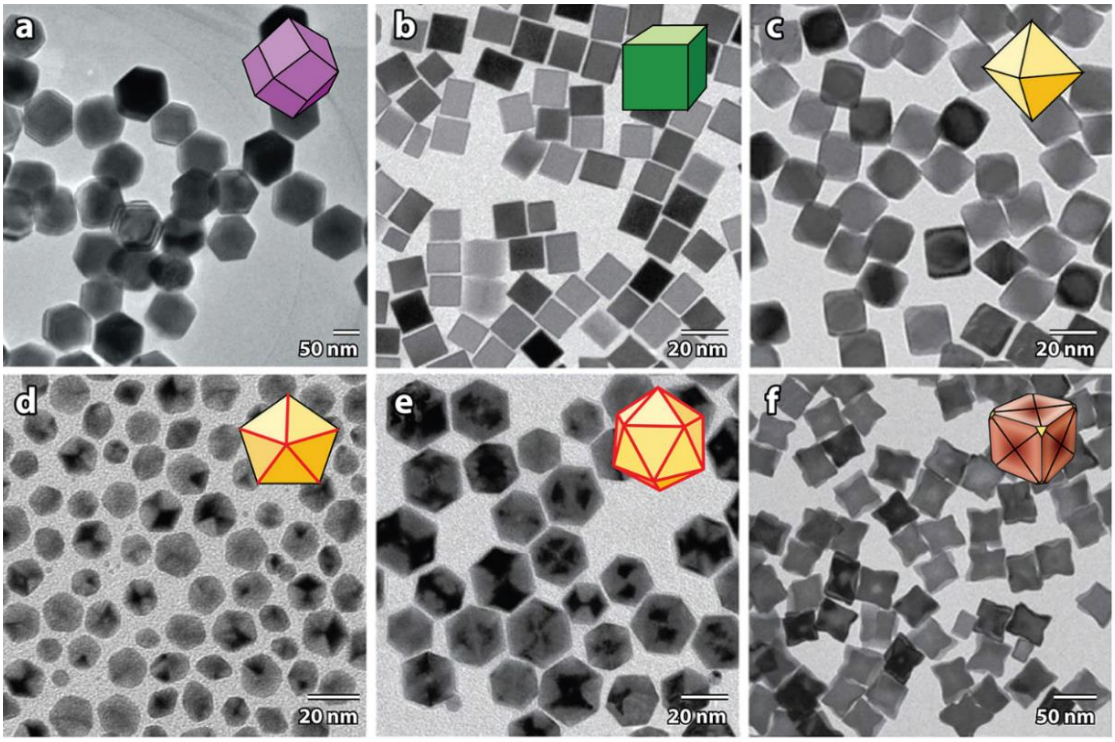

Figure 1.3. TEM images of Pd nanocrystals prepared using the solution-based synthetic approach. (A) Rhombic dodecahedra, (B) cubes, (C) octahedra, (D) decahedra, (E) icosahedra, and (F) concave cubes. (Reprinted with permission from [61]. Copyright 2016 Annual Reviews.)

A facet-selective capping agent works by altering the specific surface free energy of the facet it binds to through chemisorption, thereby changing the relative energy hierarchy of the facets involved [25]. The growth of a nanocrystal is directed and dictated by the minimization of the total surface free energy, with the surface area covered by the facet with lower energy growing at a faster rate. For example, when single-crystal, cuboctahedral Ag seeds, enclosed by both {111} and {100} facets, are allowed to grow in the presence of poly(vinyl pyrrolidone) (PVP), {100}-enclosed nanocubes will be obtained as the final product [42]. This is a result of the selective capping of Ag{100} facets by PVP. Alternatively, Ag octahedra, enclosed by {111} facets, will be obtained when sodium citrate or citric acid is used as a capping agent, due to their selective affinity toward Ag{111} facets [43]. Significantly, a capping agent can also be used to block certain regions on the surface of a seed, forcing the newly formed atoms to nucleate and grow from the bare facets only [44]. This approach can be used to create bimetallic nanocrystals with a precise control over the spatial distribution of atoms deposited during the growth process, which may prove useful in generating a tandem catalyst to work with a set of reactions simultaneously, together with enhanced thermal stability.

During the growth of a nanocrystal, it is the interplay between the rates of atom deposition ($R_{deposition}$) and surface diffusion ($R_{diffusion}$) that ultimately determines the final shape [45]. Figure 1.4 illustrates this principle by offering examples of different shapes derived from the same Pd cubic seed subjected to growth conditions with varying ratios of $R_{deposition}$ to $R_{diffusion}$. The side {100} facets of the Pd cubic seed are covered by chemisorbed Br^-, effectively preventing newly formed atoms from being directly deposited onto these sites. Consequently, the atoms are forced to grow from the unprotected corners covered by bare {111} facets. When the ratio of $R_{deposition}$ to $R_{diffusion}$ is high, the newly deposited atoms remain at the corner sites, eventually transforming the cubic seed into an octapod due to the successive deposition of atoms. Increasing $R_{diffusion}$, or decreasing $R_{deposition}$, allows the newly deposited atoms to migrate to the edges of a seed and, at even lower rate ratios, to

the side faces. These scenarios result in the formation of concave cubes, truncated cubes, and cuboctahedra, respectively. Generally, $R_{deposition}$ can be readily tuned by changing the reduction rate of a precursor by varying the type or concentration of the precursor or the reducing agent. On the other hand, $R_{diffusion}$ can be conveniently altered by the temperature, with a higher temperature corresponding to a higher $R_{diffusion}$.

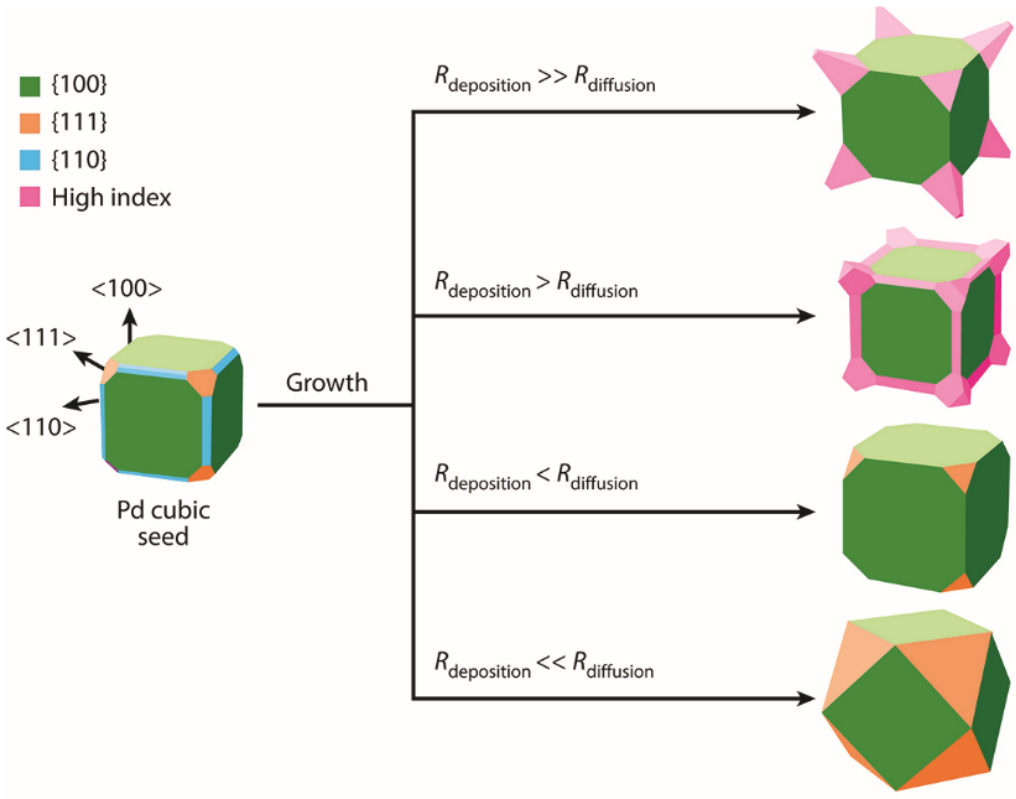

Figure 1.4. Shape control through the manipulation of atom deposition rate ($R_{deposition}$) relative to surface diffusion rate ($R_{diffusion}$). (Reprinted with permission from [61]. Copyright 2016 Annual Reviews.)

Besides atomic addition, there exist two other notably different growth pathways. The first is aggregative growth. Generally, this mechanism can be defined as the fusion of two nanocrystals to generate a larger one [46−48]. As with atomic addition, aggregative growth is also driven by minimizing the total free energy of a system. In general, smaller nanocrystals, such as nuclei and seeds, are more susceptible to aggregation because of their

larger specific surface areas and thus the corresponding higher surface free energies. The nanocrystals subject to aggregation need not be the same size. Over time, this process results in a bi-modal size distribution for the nanocrystals but eventually narrower distributions at longer reaction times due to the focusing effect. The aggregation process itself can be further separated into two categories: *i*) coalescence, which is defined as the random aggregation of nanocrystals, and *ii*) oriented attachment, which is a result of the fusion of specific nanocrystal facets to produce non-interrupted crystal planes. Interestingly, *in situ* transmission electron microscopy studies have shown that oriented attachment is preceded by the rotation of corresponding nanocrystals prior to aggregation until a proper orientation is achieved [49]. The specifics of aggregative growth have a great impact on both the shape and crystallinity of the final products, with some materials inherently preferring the aggregation pathway over the other. Finally, it should be noted that aggregative growth could follow, or accompany, atomic addition, resulting in a small number of very large nanocrystals.

The final growth pathway worth discussing is known as Ostwald ripening [50]. This mechanism typically becomes relevant after both atomic addition and aggregative growth have ceased due to the complete consumption of available monomers or precursors. Fundamentally, Ostwald ripening can be defined as the growth of larger nanocrystals at the expense of smaller ones. The driving force lies in the higher surface free energy and therefore greater solubility associated with the smaller nanocrystals relative to the larger ones. This process is typically slow and results in a broad size distribution for the final products. In order to achieve a narrower size distribution for the nanocrystals, it is desirable to avoid this growth regime. However, it should be noted that if the initial nanocrystals are polydispersed in size, Ostwald ripening could be employed to effectively reduce the degree of variation using a process commonly known as “aging”.

1.2.3 Oxidative Etching

Oxidative etching is an electrochemical process by which metal atoms are converted to cations, followed by their stabilization through complexation with ligands. Although the focus of this thesis work lies with noble-metals, it should be emphasized that oxidative etching is also involved in the synthesis of other types of nanomaterials, including those made of carbon [51, 52] and metal oxides [53]. The most common example of oxidative etching can be found in rust formation when steel is brought into contact with both air and water. In this case, the Fe^0 atoms are oxidized into Fe^{2+}/Fe^{3+} ions, while oxygen molecules are reduced into oxide/hydroxide ions. The presence of an electrolyte, such as halide ions, greatly accelerates the rate of oxidation by providing a salt bridge for the shuttled electrons. Like all corrosion processes, oxidative etching is characterized by the pitting phenomenon, a type of localized corrosion that creates discrete holes in a metal surface. This process is self-driving and capable of causing extensive damage to metal-based infrastructure, such as bridges and pipework, unless discovered and addressed.

The critical role of oxidative etching toward the formation of metal nanocrystals was initially discovered during a polyol synthesis of Ag nanocrystals [54]. When combined with oxygen from air, the presence of Cl^- impurity could cause significant changes to the morphology and purity of the final products. In particular, seeds lined with twin defects appeared in the initial stage of a synthesis but were dissolved as the reaction proceeded, with the final products dominated by Ag nanocrystals in the single-crystal structure. In addition, Ag nanocrystals with a singly-twinned structure could be produced in relatively high purity by weakening the etching strength with the use of oxygen/Br^- pair [55]. Further studies established that oxidative etching is universally involved in the solution-phase synthesis of nanocrystals from essentially all metals, including Cu, Au, Pd, Pt, Ir, and Rh [56]. To this end, it was demonstrated that oxidative etching can serve as a simple and effective method for manipulating the population of seeds, and therefore nanocrystals with

different twin structures, greatly improving the uniformity, purity, and diversity of metal nanocrystals.

The atoms that make up the surface of a nanocrystal are not all equal. In fact, there exists a considerable difference in terms of free energy, and thus reactivity, among the surface atoms depending on their locations within the topmost layer. As a general rule, the atoms with the highest free energy are the most susceptible to oxidative etching. This correlation can be employed to initiate and direct an etching process to carve metal nanocrystals into a myriad of different designs.

One of the most important parameters in determining the free energy of an atom is the number of bonds connecting that atom with its nearest neighbors. This is known as the coordination number (CN), with the free energy of an atom increasing as the CN decreases. Atoms located at the edges and vertices of a nanocrystal intrinsically possess lower CNs than those found within the faces. Likewise, the atoms found in different types of facets on the surface also differ in CN and thus in their relative free energies. For instance, the free energies of the ideal, low-index facets of a face-centered cubic (*fcc*) nanocrystal follow the order of $\gamma_{\{110\}} > \gamma_{\{100\}} > \gamma_{\{111\}}$ when situated in vacuum. If the surfaces are passivated with capping agents, the energy hierarchy will be altered, as well as the susceptibility of various surfaces toward oxidative etching [57].

Crystallographic defects, such as lattice vacancies and grain boundaries, are also spots with high propensity toward oxidative etching [58]. A vacancy is characterized by the absence of an atom from the lattice, resulting in lower CNs for all of the atoms surrounding the vacancy, while a grain boundary appears due to misalignment at the intersection of multiple crystal grains. Interestingly, unlike most other surface features of a nanocrystal, these are not static and are capable of shifting around the surface in response to the increase in kinetic energy or temperature. During this process, the defects may migrate and merge together, resulting in areas of concentrated dissolution when etching is applied.

Another factor relevant to the discussion of surface energy inhomogeneity is the lattice strain effect [59]. This phenomenon can be described as the distortion of a crystal lattice away from its ideal configuration, caused by tension at the interface between two different phases, such as facet and twin defect boundaries. Briefly, a twin defect can be defined as an atomic plane that disrupts the ideal stacking sequence of a crystal lattice, with the lattice mirrored across the defect plane. Lattice strain can be either expansive or compressive and is quantified as the percentage change in bond length for surface atoms relative to their ideal bulk value. The effect is felt strongest at the interface and diminishes rapidly as the distance from the interface increases. Strained features increase the surface free energy of a nanocrystal considerably, making it far more prone to oxidative etching compared to its low-strain counterparts. This is the very inhomogeneity that was exploited to create the aforementioned pure samples of Ag nanocrystals [54, 55]. Significantly, mild etching could be used to target nanocrystals possessing multiple twinned defects within their structure, while leaving behind the single-crystal or singly-twinned structures.

Finally, surface composition is a vital parameter in determining the etching behavior of a nanocrystal [60]. The propensity of an element to dissolution is governed by its reduction potential. In a surface composed of two different metals, the metal with the lower reduction potential will be more readily dissolved upon exposure to an etchant. By tailoring the surface composition of a nanocrystal, we can selectively promote or inhibit the etching at certain sites. For instance, by depositing a metal with a higher reduction potential at the corners or edges of an existing nanocrystal, we can protect these normally vulnerable sites from dissolution, while promoting the etching of the unprotected zones.

1.3 Scope of This Work

The aim of this dissertation is to develop further understanding of the mechanisms responsible for the size, shape, and structural evolution of colloidal noble-metal nanocrystals, as well as to apply these mechanisms to the rational development of robust

synthetic protocols. While significant progress has been made over the past decade, the synthesis of noble-metal nanocrystals has remained largely reliant on trial-and-error. A better understanding of the underlying forces guiding the formation and development of noble-metal nanocrystals will help avoid the waste of time and precious feedstock, and ultimately accelerate the adoption of these nanomaterials in widespread applications. This dissertation will focus on the roles of nucleation and growth processes in noble-metal nanocrystal synthesis, guided by kinetic considerations and the presence of appropriate capping agents, as well as the impact of oxidative etching.

In Chapter 2, I describe a polyol method for the facile synthesis of Ag nanocubes having sharp edges and edge lengths below 15 nm. The rapid nucleation of Ag atoms was facilitated through the addition of a trace amount of SH^- to generate Ag_2S clusters while the corners and edges of the nanocubes were sharpened through the introduction of Br^- as a regulator of the growth kinetics and a capping agent for the Ag(100) surface. The mechanistic roles of these additives, along with the effects of their interactions with other species present in the reaction solution, were all systematically investigated. The concentration of SH^- was found to be a particularly effective parameter for tuning the edge length of the nanocubes.

In Chapter 3, I report a systematic study of the sulfate-mediated polyol synthesis of Pd decahedra in an attempt to maximize both the conversion and morphology yields. Quantitative analyses of the as-obtained products revealed the presence of nanocrystal populations with distinct ranges of size. Samples collected in the early stage of a standard synthesis indicated that this size distribution is likely caused by the coalescence of the initially formed decahedral nuclei. Kinetic measurements clearly showed the impact of the sulfate additive on the initial reduction rate, and thus the yield of decahedral nuclei. Based on the mechanistic understanding developed over the course of this work, I was able to significantly improve the conversion and morphology yields of the Pd decahedra synthesis by introducing a second reducing agent after the completion of homogeneous nucleation.

In Chapter 4, my coworkers and I develop the rational design and successful implementation of a one-pot, polyol method for the synthesis of penta-twinned Pd nanowires with diameters below 8 nm and aspect-ratios of up to 100. The key to the success of this protocol was the controlled reduction of Na_2PdCl_4 by diethylene glycol and ascorbic acid through the introduction of NaI and HCl. The I^- and H^+ ions could slow down the reduction kinetics by forming PdI_4^{2-} and inhibiting ascorbic acid dissociation, respectively. When the initial reduction rate was tuned into the proper regime, Pd decahedral seeds with a unique penta-twinned structure emerge during nucleation. In the presence of I^- ions as a selective capping agent toward the Pd(100) surface, the decahedral seeds were directed to grow axially into penta-twinned nanorods and then nanowires. In terms of applications, the Pd nanowires were demonstrated as an effective electrocatalyst for formic acid oxidation, with a specific current density three times greater than that of a commercial Pd/C catalyst due to the presence of both {100} facets and twin boundaries on the surface. The Pd nanowires could also serve as sacrificial templates for the conformal deposition of Pt atoms to generate Pd@Pt core-sheath nanowires and then Pd-Pt nanotubes with a well-defined surface structure.

In Chapter 5, I report a systematic study of the oxidative etching of penta-twinned Pd decahedral nanocrystals by O_2/I^- under different conditions and its impact on their subsequent growth behavior. Analysis by transmission electron microscopy showed significant rounding of the decahedral structure. More specifically, the etching was found to begin at the equatorial vertices, due to their high surface free energy, with the formation of re-entrant grooves and proceed along the adjacent, equatorial edges through the dissolution of low-coordination atoms. Comparison of the etching behaviors under different conditions revealed the critical role of a reductive environment for the initiation of oxidative etching, likely due to the presence of a protective oxide layer on the surface of Pd decahedra. Overgrowth on the seeds with a rounded profile generated penta-twinned Pd nanorods with an asymmetric, tapered structure as a result of simultaneous axial and

radial growth. In comparison, the original decahedral seeds only showed axial growth, leading to the formation of penta-twinned nanorods with a uniform size along the axial direction.

1.4 Notes to Chapter 1

Parts of this chapter are adapted from "Bimetallic Nanocrystals: Syntheses, Properties, and Applications" published in *Chemical Reviews* [60], "Shape-Controlled Metal Nanocrystals for Heterogeneous Catalysis" published in the *Annual Reviews of Chemical and Biochemical Engineering* [61], "The Science and Art of Carving Metal Nanocrystals" published in *ACS Nano* [62], "Toward the Synthesis of Sub-15 nm Ag Nanocubes with Sharp Corners and Edges: The Roles of Heterogeneous Nucleation and Surface Capping" published in the *Journal of the American Chemical Society* [63], and "Toward a Quantitative Understanding of the Sulfate-mediated Synthesis of Pd Decahedral Nanocrystals with High Conversion and Morphology Yields" published in the *Chemistry of Materials* [64]. All of these publications were co-atuthrored by me.

1.5 References

[1] Lewis, L. N. *Chem. Rev.* **1993**, *93*, 2693−2730.

[2] Somorjai, G. A. *Chem. Rev.* **1996**, *96*, 1223−1236.

[3] Aiken III, J. D.; Finke, R. G. *J. Mol. Catal. A-Chem.* **1999**, *145*, 1−44.

[4] Ertl, G. *Handbook of Heterogeneous Catalysis*, Wiley-VCH, Weinheim, **2008**.

[5] N. M. Davey, R. J. Seymour, *Platinum Met. Rev.* **1985**, *29*, 2.

[6] Okinaka, Y.; Hoshino, M. *Gold Bull.* **1998**, *31*, 3−13.

[7] Jeong, S.; Woo, K.; Kim, D.; Lim, S.; Kim, J. S.; Shin, H.; Xia, Y.; Moon, *J. Adv. Funct. Mater.* **2008**, *18*, 679−686.

[8] Talapin, D. V.; Lee, J.-S.; Kovalenko, M. V.; Shevchenko, E. V. *Chem. Rev.* **2010**, *110*, 389−458.

[9] Maier, S. A.; Brongersma, M. L.; Kik, P. G.; Meltzer, S.; Requicha, A. A. G.; Atwater, H. A. *Adv. Mater.* **2001**, *13*, 1501−1505.

[10] Kauranen, M.; Zayats, A. V. *Nat. Photonics* **2012**, *6*, 737−748.

[11] Gupta, M. C.; Ballato, J. *The Handbook of Photonics*, CRC Press, Taylor & Francis Group, Boca Raton, **2006**.

[12] Koenderink, A. F.; Alù, A.; Polman, A. *Science* **2015**, *348*, 516−521.

[13] Murray, C. B.; Sun, S.; Doyle, H.; Betley, T. *MRS Bull.* **2001**, *26*, 985−991.

[14] Kozicki, M. N; Mitkova, M.; Park, M.; Balakrishnan, M.; Gopalan, C. *Superlattices Microst.* **2004**, *34*, 459−465.

[15] Ditlbacher, H.; Lamprecht, B.; Leitner, A.; Aussenegg F. R. *Optics Lett.* **2000**, *25*, 563−565.

[16] Nozik, A. J.; Miller, J. *Chem. Rev.* **2010**, *110*, 6443−6445.

[17] Linic, S. Christopher, P.; Ingram, D. B. *Nat. Mater.* **2011**, *10*, 911−921.

[18] Jena, P. J. *Phys. Chem. Lett.* **2011**, *2*, 206−211.

[19] Cohn, J. G. *Environ. Health Perspect.* **1975**, *10*, 159−164.

[20] Parks II, J. E. *Science* **2010**, *327*, 1584−1585.

[21] Alivisatos, P. *Nat. Biotechnol.* **2004**, *22*, 47−52

[22] Jain, P. K.; El-Sayed, I. H.; El-Sayed, M. A. *Nano Today* **2007**, *2*, 18−29.

[23] Burda, C.; Chen, X.; Narayanan, R.; El-Sayed, M. A. *Chem. Rev.* **2005**, *105*, 1025−1102.

[24] Xia, Y.; Li, W.; Cobley, C. M.; Chen, J. ; Xia, X.; Zhang, Q.; Yang, M.; Cho, E. C.; Brown P. K. *Acc. Chem. Res.* **2011**, *44*, 914−924.

[25] Xia, Y.; Xiong, Y. J.; Lim, B.; Skrabalak, S. E. *Angew. Chem. Int. Ed.* **2009**, *48*, 60−103.

[26] Hutchings, G. J. *J. Catal.* **1985**, *96*, 292−295.

[27] Haruta, M.; Daté, M. *Appl. Catal., A* **2001**, *222*, 427−437.

[28] Tian, N.; Zhou, Z. Y.; Sun, S. G.; Ding, Y.; Wang, Z. L. *Science* **2007**, *316*, 732−735.

[29] Bratlie, K. M.; Lee, H.; Komvopoulos, K.; Yang, P.; Somorjai, G. A. *Nano Lett.* **2007**, *7*, 3097−3101.

[30] Crespo-Quesada, M.; Yarulin, A.; Jin, M.; Xia, Y.; Kiwi-Minsker, L. *J. Am. Chem. Soc.* **2011**, *133*, 12787−12794.

[31] Tao, A. R.; Habas, S.; Yang, P. *Small* **2008**, *4*, 310−325.

[32] Zhang, H.; Jin, M.; Xia, Y. *Angew. Chem., Int. Ed.* **2012**, *51*, 7656−7673.

[33] Lim, B.; Xia, Y. *Angew. Chem., Int. Ed.* **2011**, *50*, 76−85.

[34] Quan, Z.; Wang, Y.; Fang, J. *Acc. Chem. Res.* **2013**, *46*, 191−202.

[35] Wang, Y.; Xie, S.; Liu, J.; Park, J.; Huang, C. Z.; Xia, Y. *Nano Lett.* **2013**, *13*, 2276–2281.

[36] Xiong, Y.; Cai, H.; Wiley, B. J.; Wang, J. M.; Kim, M. J.; Xia, Y. *J. Am. Chem. Soc.* **2007**, *129*, 3665–3675.

[37] LaMer, V. K.; Dinegar R. H. *J. Am. Chem. Soc.* **1950**, *72*, 4847−4854.

[38] Thanh, N. T. K.; Maclean, N.; Mahidine, S. *Chem. Rev.* **2014**, *114*, 7610−7630.

[39] Xia, Y.; Xia, X.; Peng, H.-C. *J. Am. Chem. Soc.* **2015**, *137*, 7947–7966.

[40] Barnard, A. S.; Young, N. P.; Kirkland, A. I.; van Huis, M. A.; Xu, F. *ACS Nano*, **2009**, *3*, 1431–1436.

[41] Wang, Y.; Peng, H.-C.; Liu, J.; Huang, C.Z.; Xia, Y. *Nano Lett.*, **2015**, *15*, 1445–1450.

[42] Zeng, J.; Zheng, Y.; Rycenga, M.; Tao, J.; Li, Z. Y.; Zhang, Q.; Zhu, Y.; Xia, Y. *J. Am. Chem. Soc.*, **2010**, *132*, 8552–8553.

[43] Wang, Y.; Wan, D.; Xie, S.; Xia, X.; Huang, C. Z.; Xia, Y. *ACS Nano*, **2013**, 4586–4594.

[44] Xie, S.; Lu, N.; Xie, Z.; Wang, J.; Kim, M. J.; Xia, Y. *Angew. Chem., Int. Ed.* **2012**, *51*, 10266−10270.

[45] Xia, X.; Xie, S.; Liu, M.; Peng, H.-C.; Lu, N.; Wang, J.; Kim, M. J.; Xia, Y. *Proc. Natl. Acad. Sci. USA* **2013**, *110*, 6669−6673.

[46] Wang, F.; Richards, V. N.; Shields, S. P.; Buhro, W. E. *Chem. Mater.* **2014**, *26*, 5−21.

[47] Zhang, J.; Huang, F.; Lin, Z. *Nanoscale* **2010**, *2*, 18−34.

[48] Yuk, J. M.; Park, J.; Ercius, P.; Kim, K.; Hellebusch, D. J.; Crommie, M. F.; Lee, J. Y.; Zettl, A.; Alivisatos, A. P. *Science* **2012**, *336*, 61−64.

[49] Li, D.; Nielsen, M. H.; Lee, J. R. I.; Frandsen, C.; Banfield, J. F.; De Yoreo, J. J. *Science* **2012**, *336*, 1014−1018.

[50] Ratke, L.; Voorhees, P. W. *Growth and Coarsening: Ostwald Ripening in Materials Processing*, Springer, Berlin, **2002**.

[51] Moon, C.-Y.; Kim, Y.-S.; Lee, E.-C.; Jin, Y.-G.; Chang, K. *J. Phys. Rev. B* **2002,** *65*, 155401.

[52] Yoshimoto, M.; Yoshida, K.; Maruta, H.; Hishitani, Y.; Koinuma, H.; Nishio, S.; Kakihana, M.; Tachibana, T. *Nature* **1999**, *399*, 340–342.

[53] Sui, Y.; Fu, W.; Zeng, Y.; Yang, H.; Zhang, Y.; Chen, H.; Li, Y.; Li, M.; Zou, G. *Angew. Chem., Int. Ed.* **2010**, *49*, 4282–4285.

[54] Wiley, B.; Herricks, T.; Sun, Y.; Xia, Y. *Nano Lett.* **2004**, *4*, 1733−1739.

[55] Wiley, B.J.; Xiong, Y.; Li, Z.-Y.; Yin, Y.; Xia, Y. *Nano Lett.* **2006**, *6*, 765–768.

[56] Zheng, Y.; Zeng, J.; Ruditskiy, A.; Liu, M.; Xia, Y. *Chem. Mater.* **2014**, *26*, 22−33.

[57] Ortiz, N.; Skrabalak, S. E. *Langmuir* **2014**, *30*, 6649–6659.

[58] Hines, M.A. *Annu. Rev. Phys. Chem.* **2003**, *54*, 29–56.

[59] Sneed, B. T.; Young, A. P.; Tsung, C.-K. *Nanoscale* **2015**, *7*, 12248−12265.

[60] Gilroy, K. D.; Ruditskiy, A.; Peng, H.-C. Qin, D.; Xia, Y. *Chem. Rev.* **2016**, *116*, 10414–10472.

[61] Ruditskiy, A.; Peng, H.-C.; Xia, Y. *Annu. Rev. Chem. & Biomol. Eng.* **2016**, *7*, 327−348.

[62] Ruditskiy, A.; Xia, Y. *ACS Nano*, **2017**, *11*, 23–27.

[63] Ruditskiy, A.; Xia, Y. *J. Am. Chem. Soc.* **2016**, *138*, 3161–3167.

[64] Ruditskiy, A.; Zhao, M.; Gilroy, K. D.; Vara, M.; Xia, Y. *Chem. Mater.* **2016**, *28*, 8800–8806.

CHAPTER 2

SYNTHESIS OF SUB-15 NM SILVER NANOCUBES WITH SHARP EDGES: THE ROLES OF HETEROGENEOUS NUCLEATION AND SURFACE CAPPING

2.1 Introduction

For over a decade, intense research has been directed toward the development and refinement of protocols used for the synthesis of Ag nanocrystals with a broad range of well-controlled sizes and shapes [1−11]. The driving force stems from the potential utility of these nanocrystals in diverse applications, including photonics, electronics, catalysis, sensing, and medicine [12−23]. Among those Ag nanocrystals, nanocubes with sharp corners and edges, together with tunable edge lengths, have garnered particular attention owning to their superb performance in applications involving localized surface plasmon resonance (LSPR) [24−28] and surface-enhanced Raman scattering (SERS) [29−31]. When employed for the epoxidation of ethylene, Ag nanocubes have shown greater selectivity toward the production of ethylene oxide relative to both Ag nanospheres and irregular nanoparticles [32, 33]. This result has been attributed to the fact that the surface of a Ag nanocube is almost completely covered by {100} facets, whereas the surface of a nanosphere or irregular nanoparticle is covered by a mix of {100} and {111} facets. Moreover, Ag nanocubes have been used as sacrificial templates to generate hollow nanostructures (*e.g.*, nanoboxes and nanocages) composed of Au, Pd, and Pt, which show promise as platform nanomaterials for drug delivery, imaging contrast enhancement, photothermal treatment, as well as plasmon-enhanced catalysis [34, 35].

The synthetic methods for the preparation of well-defined Ag nanocubes with narrow size distributions have been constantly refined over the past decade or so. In 2002, a one-pot protocol involving the use of ethylene glycol (EG) as both the solvent and reductant

was reported [4]. In the following years, various refinements were introduced to optimize this synthesis. These include the introduction of HCl as an oxidative etchant [36], the addition of sulfide (S^{2-}) and bisulfide (SH^-) ions to promote the formation of single-crystal seeds [37], and the substitution of $AgNO_3$ by CF_3COOAg in an effort to achieve a higher degree of control and better reproducibility [38]. More recently, EG was substituted by diethylene glycol (DEG), enabling the preparation of Ag nanocubes with edge lengths down to 18 nm [39]. Prior attempts to produce Ag nanocubes below this size failed, primarily due to the high reduction rates present in the EG-based system, as well as ineffective surface capping by poly(vinyl pyrrolidone) (PVP), a bulky, polymer-based capping agent for the Ag(100) surface. On the other hand, the Ag nanocubes produced using the DEG-based method displayed significant rounding at the corners and edges, particularly at sizes below 25 nm. Furthermore, the DEG-based synthesis was subsequently shown to be sensitive to variations in impurity levels between different batches of DEG, thereby lowering the overall reproducibility of that protocol.

Herein, I report an EG-based synthesis of Ag nanocubes having sharp corners and edges, together with edge lengths below 15 nm. The success of this synthesis relies on a tight control over the nucleation process through the addition of trace amounts of SH^- and the substitution of HCl by NaCl as the chloride source, as well as the use of Br^- as an effective capping agent for small-sized particles. The mechanistic roles of these additives on the nucleation and growth are systematically studied. The use of Br^- as a capping agent has been previously explored in the aqueous synthesis of Pd nanocubes/nanobars with sizes as small as 6 nm and seeded-growth of Ag nanobars as small as 35 nm in a polyol-based system [31, 40−43]. However, Br^- ions have not been exploited so far for the generation of Ag nanocubes with sharp corners and edges, together with small sizes down to 15 nm. To my knowledge, the Ag nanocubes presented herein are the smallest ever reported, while exhibiting a much higher degree of structural definition compared to previous reports. The potential applications of such small Ag nanocubes include their use as well-defined

catalysts with higher surface-to-volume ratios. They can also serve as sacrificial templates for the production of small nanocages sought by both nanomedicine and catalysis [35].

2.2 Results and Discussion

Synthesis of Small Ag Nanocubes. Figure 2.1 shows TEM images of the Ag nanocubes obtained by allowing different periods of time to pass after the introduction of CF_3COOAg, but before the injection of NaBr solution. For the purposes of clarity, this period will be referred to as the delay time, while the time elapsed after the addition of NaBr will be referred to as the growth time. For the standard synthesis, the delay time and growth time were 5 min and 15 min, respectively, and I obtained Ag nanocubes with an average edge length of 13.4±0.4 nm, as shown in Figure 2.1A. A histogram showing the edge length distribution for this sample can be found in Figure 2.2. Extending the delay time to 10, 15, and 25 min, while keeping the growth time fixed, resulted in larger Ag nanocubes with average edge lengths of 15.3±0.6, 15.8±0.4, and 18.6±0.7 nm, respectively, as shown in Figure 2.1, B−D. At longer delay times, the edge length was capped at ~23 nm, likely due to the depletion of all CF_3COOAg precursor. Further shortening the delay time did not generate Ag nanocubes with significantly shorter edge lengths when compared with the standard synthesis. For instance, the use of a delay time of 1 min produced Ag nanocubes 12.7±0.6 nm in edge length, as well as a large number of relatively large multiply-twinned nanoparticles, as shown in Figure 2.3. Similarly, extending the growth time from 15 min to 60 min only resulted in a marginal increase in edge length by 1.0 nm (Figure 2.4). The longer growth time did not compromise the corner and edge sharpness of the nanocubes. However, TEM images showed the formation of sub-5 nm particles in the solution when the growth time was increased, suggesting additional nucleation.

In order to study the evolution of corners and edges on small Ag nanocubes, I conducted syntheses at short growth times. Figure 2.5, A−D, shows TEM images of the products obtained by varying the growth time from 0 to 15 min, with an increment of 5 min.

Immediately after the addition of NaBr solution (Figure 2.5A), the product consisted of 11.7±1.0 nm Ag cuboctahedra. In addition, a large number of sub-5 nm nanoparticles were observed. As the reaction continued, a fraction of cuboctahedra (*i.e.*, nanocrystals with rounded corners and edges) would emerge, most noticeably at a growth time of 10 min (Figure 2.5C). Notably, the cuboctahedra then developed into nanocubes without any significant change to the edge length.

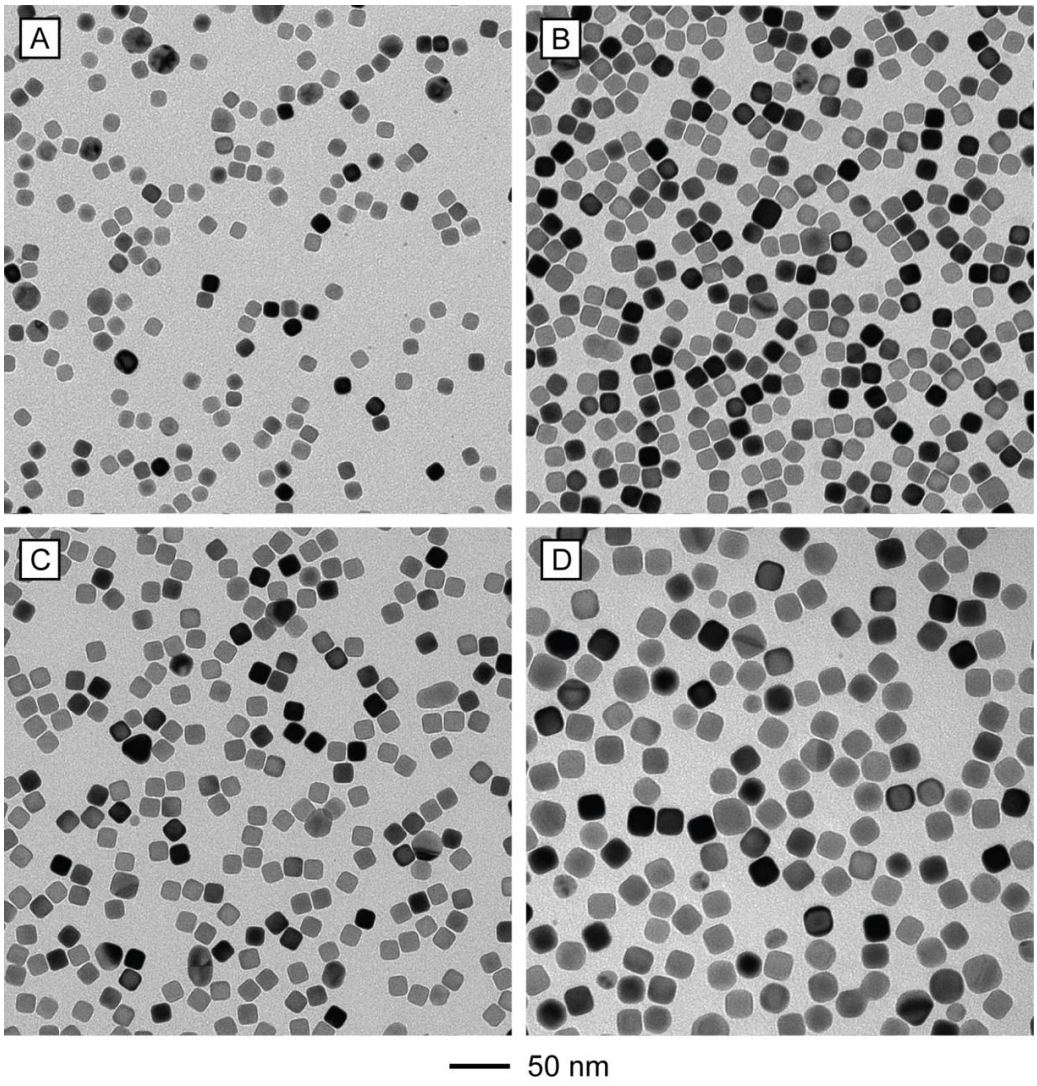

Figure 2.1. TEM images of Ag nanocubes synthesized with the use of different delay times before the introduction of Br^- ions: (A) 5, (B) 10, (C) 15, and (D) 25 min. The average edge lengths of the nanocubes were (A) 13.4±0.4, (B) 15.3±0.6, (C) 15.8±0.4, and (D) 18.6±0.7 nm. (Reprinted with permission from [50]. Copyright 2016 American Chemical Society.)

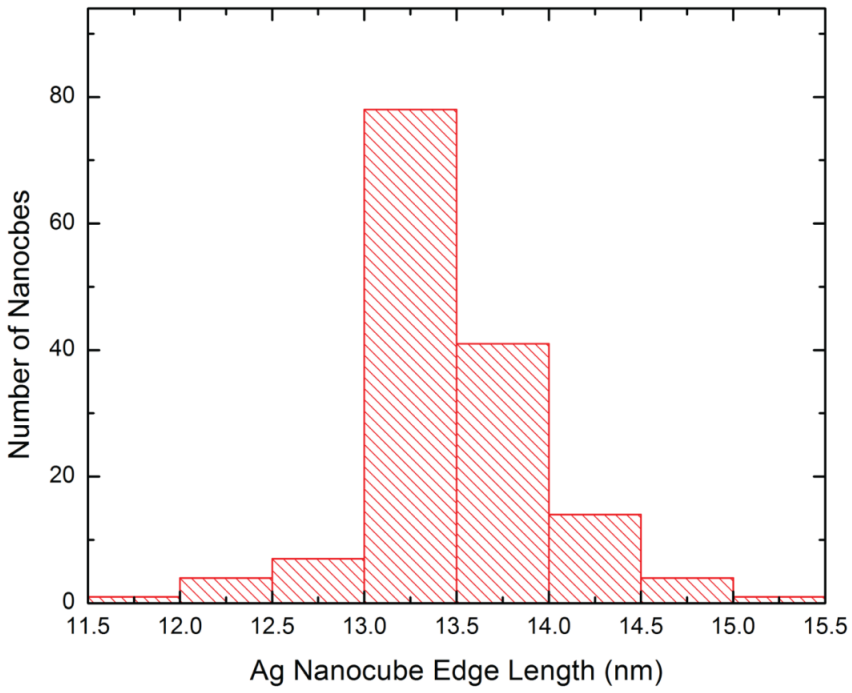

Figure 2.2. A histogram showing the edge length distribution of Ag nanocubes shown in Figure 2.1A. (Reprinted with permission from [50]. Copyright 2016 American Chemical Society.)

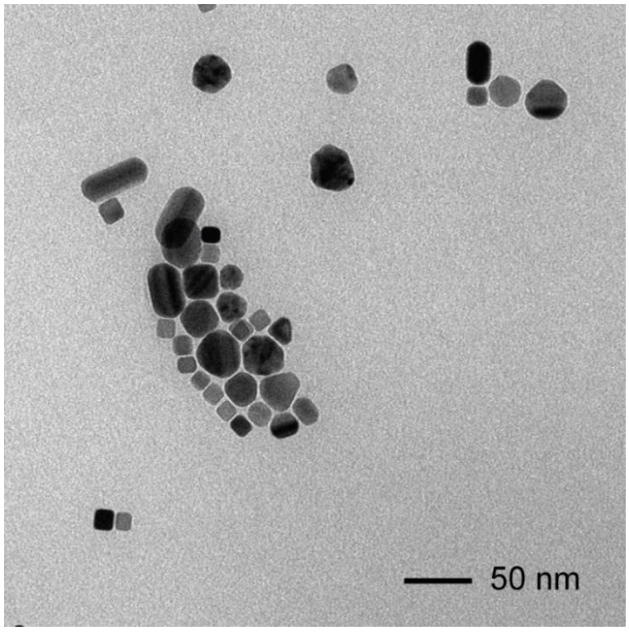

Figure 2.3. TEM image of the reaction product synthesized with a delay time of 1 min, while all other parameters were kept the same as in the standard synthesis. (Reprinted with permission from [50]. Copyright 2016 American Chemical Society.)

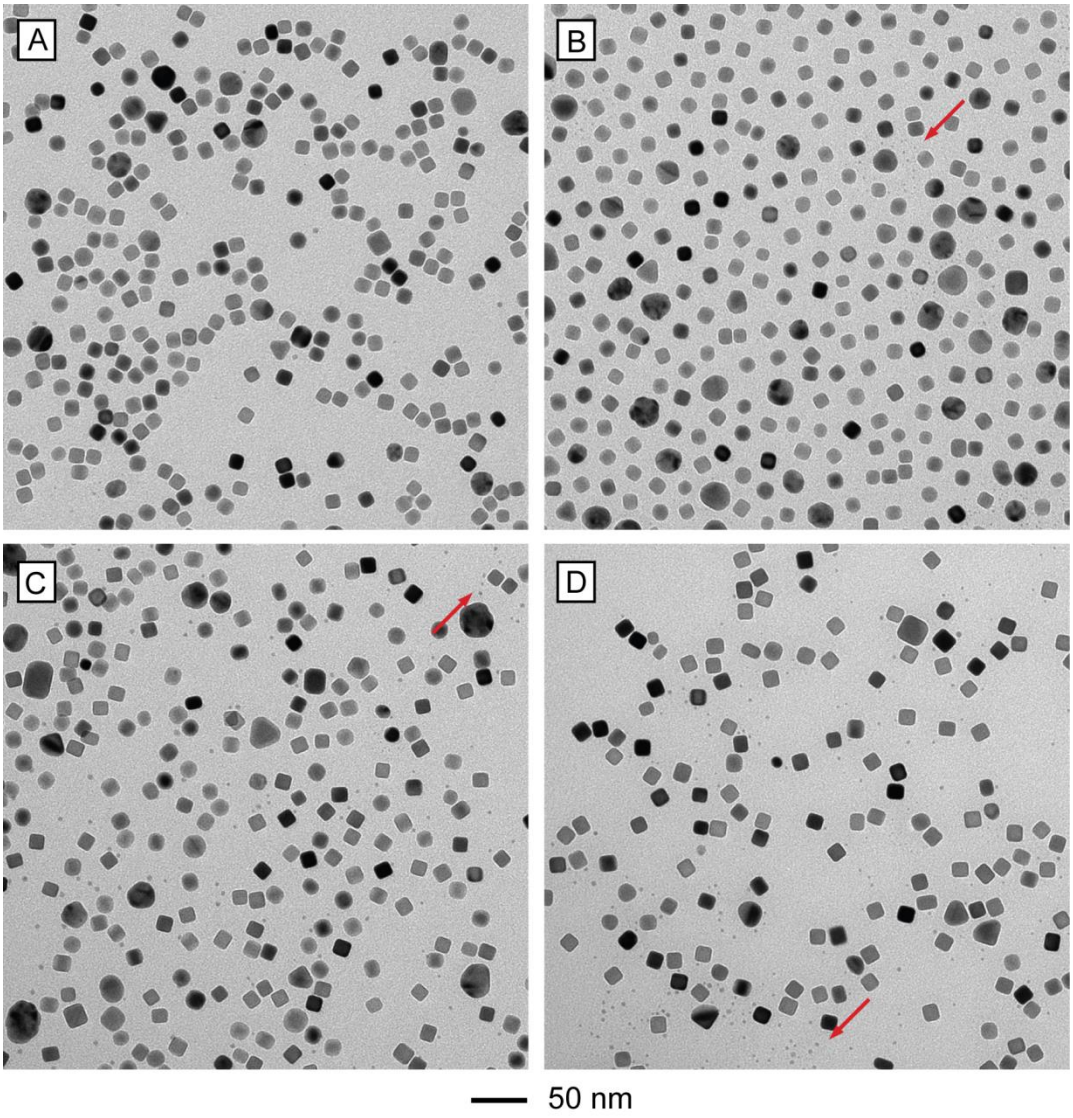

Figure 2.4. TEM images of reaction products obtained with prolonged growth times: (A) 15, (B) 30, (C) 45, and (D) 60 min, whereas all other parameters were kept the same as in the standard synthesis. The average edge lengths were: (A) 13.3±0.6, (B) 13.4±0.6, (C) 13.8±0.7, and (D) 14.3±0.6 nm. Note the formation of sub-5 nm particles, as denoted by red arrows. (Reprinted with permission from [50]. Copyright 2016 American Chemical Society.)

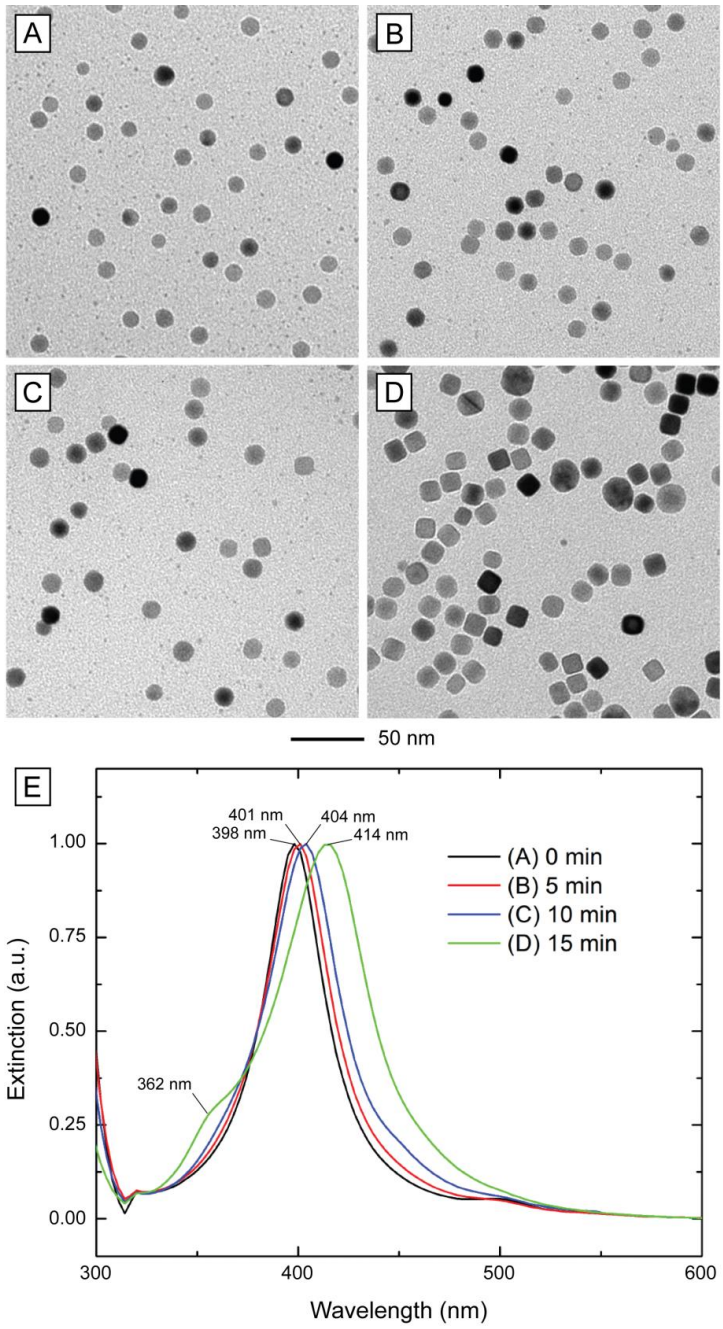

Figure 2.5. (A-D) TEM images of samples obtained using different growth times after the addition of Br^- ions: (A) 0, (B) 5, (C) 10, and (D) 15 min. (E) UV-vis spectra of the samples shown in (A-D). Note that the appearance of a shoulder peak at ~360 nm, along with a 10 nm red-shift for the major peak, coincides with the emergence of sharp corners and edges on the nanocubes as revealed by TEM. The shoulder peak around 500 nm can be attributed to the presence of large irregular particles and/or aggregation of nanocrystals in the product. (Reprinted with permission from [50]. Copyright 2016 American Chemical Society.)

Furthermore, the fraction of sub-5 nm particles decreased significantly, likely due to the Ostwald ripening effect. After 15 min of growth (Figure 2.5D), the product consisted of 13.1±0.5 nm Ag nanocubes with sharp corners and edges, as well as a smaller fraction of irregular, multiply-twinned particles of ~20 nm in size. Overall, the purity of Ag nanocubes was over 90%. UV-vis spectra taken from the products after different growth times (Figure 2.5E) revealed little change to the optical features during the initial 10 min after the introduction of NaBr, with a single absorption peak positioned around 404 nm. However, after growth for 15 min, the absorption peak was red-shifted to 414 nm, and a shoulder peak appeared at 360 nm. This phenomenon coincided with the appearance of sharp structural features, such as corners and edges, for the majority of Ag nanocrystals present in the sample. A shoulder peak around 500 nm can be attributed to the presence of large irregular particles and/or aggregation of nanocrystals in the product, as has been noted in previous studies [36−38]. I further confirmed the good reproducibility of the standard procedure by comparing the UV-vis spectra recorded from three different batches of a synthesis of 13-nm Ag nanocubes. As shown in Figure 2.6, the UV-vis spectra overlap reasonably well, indicating good agreement in size and structural definition between the distinct batches.

I have also used TEM imaging to analyze the corner/edge sharpness of the final Ag nanocubes. First, a square outline was manually fitted over the 2-D TEM image of a Ag nanocube, simulating the perimeter of a completely sharp nanocube face. The area occupied by the truncated Ag nanocube in the TEM image was determined by manually subtracting the triangular areas of the missing corners from the area of the fitted square outline. An example is shown in Figure 2.7. I define the measure of nanocube sharpness as the ratio of the area of the Ag nanocube in the TEM image to the area of the fitted square outline, with the value of 1 denoting perfect sharpness. This can also be thought of as the extent of nanocube surface coverage by {100} facets. The final reported value is the simple average of measurements collected for 100 randomly selected nanocubes. For Ag

nanocubes with edge lengths of 13.4±0.4, 15.3±0.6, and 18.6±0.7 nm (Figure 2.1, A−C), they were found to exhibit sharpness on the order of 0.96, 0.95, and 0.95, respectively.

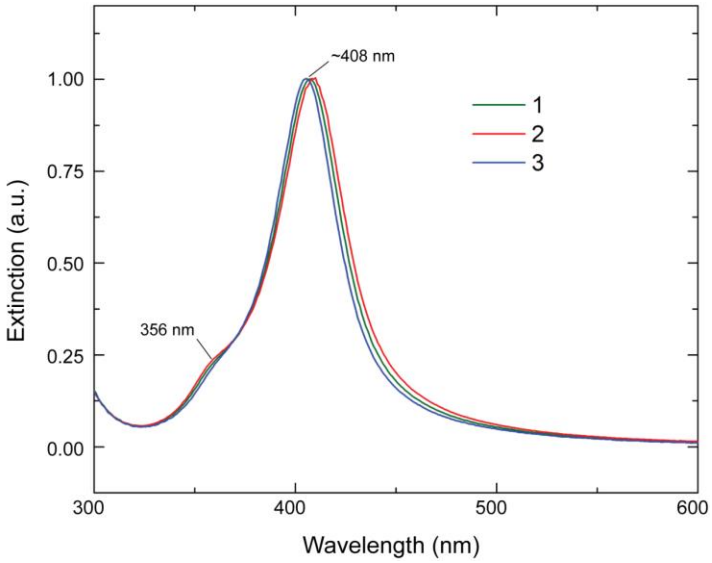

Figure 2.6. UV-vis spectra of three different batches of 13-nm Ag nanocubes, as a demonstration of reproducibility for standard synthesis. (Reprinted with permission from [50]. Copyright 2016 American Chemical Society.)

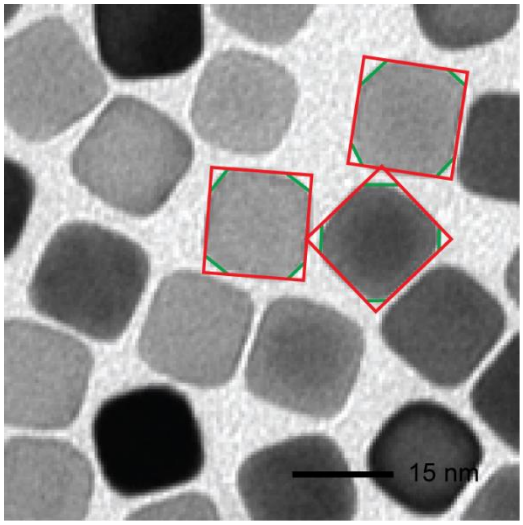

Figure 2.7. Illustration showing how TEM imaging is used to determine the edge sharpness of the 15-nm Ag nanocubes. The fitted square outline is denoted in red. The 2-D area of the Ag nanocube is determined by manually subtracting the triangular areas of the missing corners, marked in green, from the area of the fitted square outline. The measure of edge sharpness is defined as the ratio between the area occupied by a Ag nanocube and the area of the fitted square outline. I obtained an average value by analyzing 100 randomly selected nanocubes. (Reprinted with permission from [50]. Copyright 2016 American Chemical Society.)

In comparison, the previously reported smallest 18 nm Ag nanocubes prepared using the DEG-based method, only gave a sharpness measure of 0.90, thus highlighting the improvement of the new approach [39].

The Effects of SH^- on Ag Nucleation. In principle, there exists two different pathways for Ag atoms to nucleate: homogeneous and heterogeneous. Homogeneous nucleation necessitates the presence of a supersaturated concentration of free Ag atoms, which can be obtained through steady reduction of a salt precursor. Once supersaturation has been achieved, the free Ag atoms coalesce into small clusters, which then serve as nuclei for further growth. The rapid growth quickly consumes the available Ag atoms, thereby bringing down the concentration of Ag atoms below the supersaturation threshold and ultimately quenching the nucleation process. In contrast, heterogeneous nucleation is characterized by the deposition of Ag atoms onto locally available surfaces, without requiring a supersaturated environment. This is due to an intrinsically lower free energy barrier for heterogeneous nucleation as compared to homogenous nucleation. As a consequence of this imbalance, heterogeneous nucleation occurs much more rapidly when compared with its counterpart. Based on this information, it should be possible to create a large number of Ag nanocrystals by purposely introducing cluster-sized, insoluble impurities, analogous to those produced by homogeneous nucleation, into the reaction solution to serve as sites for rapid heterogeneous nucleation and growth. The number of these nucleation sites will determine the size of the final Ag nanocrystals, since the fixed number of Ag atoms available from the precursors are supposed to be evenly divided among the nuclei during growth. Thus, a larger number of nuclei will produce smaller Ag nanocrystals, and vice versa.

The bisulfide-assisted polyol synthesis of monodisperse Ag nanocubes is an example of this approach [37, 38]. In those reports, it was posited that bisulfide (SH^-) and Ag^+ ions quickly react to produce highly insoluble Ag_2S clusters ($K_{sp} = 10^{-52}$), which then serve as sites for the rapid heterogeneous nucleation of Ag atoms and subsequent formation of

single-crystal nanocubes. The produced Ag_2S cluster is too small for the lattice mismatch between Ag_2S (monoclinic) and Ag (face-centered cubic) to impact the crystal structure of the nanocrystal beyond the few initially deposited layers of Ag. As a result, uniform Ag nanocubes with an edge length as short as 30 nm could be prepared in an EG-based system containing a trace amount of SH^- (27 μM). Figure 2.8 shows a mechanistic illustration of this approach. A subsequently developed protocol reduced the edge length of the nanocubes down to 18 nm by replacing EG with DEG [39]. In both cases, an HCl solution was added as a source of Cl^-, necessary to modulate the reaction kinetics and provide a source of mild oxidative etching. Specifically, the addition of Cl^- creates AgCl ($K_{sp} = 10^{-10}$) in solution, which dissolves over time, unlike Ag_2S. This regulates the amount of Ag^+ available for reduction in the initial stages of the synthesis, thereby allowing for control over reaction kinetics. Oxidative etching can be understood as a redox reaction between Ag atoms and dissolved O_2 gas, with Cl^- acting as a charge carrier [44]. Figure 2.9, A and C, shows the products of a standard synthesis taken at 20 and 30 min after the introduction of Ag precursor, respectively, with HCl serving as a source of chloride and without adding any NaBr. The average edge lengths were measured to be 25.4±1.3 and 35.0±1.0 nm at 20 and 30 min post Ag precursor addition, respectively. This corresponds to a 161% change in volume for the Ag nanocubes over a growth time of 10 min, demonstrating very rapid growth, and suggesting that a large number of Ag atoms remained in the reaction solution after nucleation. At first glance, such quick growth appears to be at odds with the idea of a large number of nuclei present in the system, as I expect the available Ag precursors to be rapidly drained *via* heterogeneous nucleation in the early stage of a synthesis.

A closer look at the interactions between the reactants, and their influence on the mechanism responsible for the formation of the initial Ag_2S clusters, may provide the answer. The molar ratio of dissociated H^+ to SH^- present in the final reaction solution was 8.3:1, with HCl being introduced into the system immediately after the introduction of SH^- and before the injection of the Ag precursor. This consecutive addition, coupled with an

excess of H^+, likely results in a rapid recombination reaction between H^+ and SH^- ions, thereby irreversibly producing H_2S and consuming the free SH^- entirely. From previous measurements, the solubility of H_2S in EG at 125 ºC can be estimated to be 1.87 g per kg, which is sufficient to dissolve all the newly produced H_2S gas, even assuming full conversion of SH^- to H_2S [45, 46].

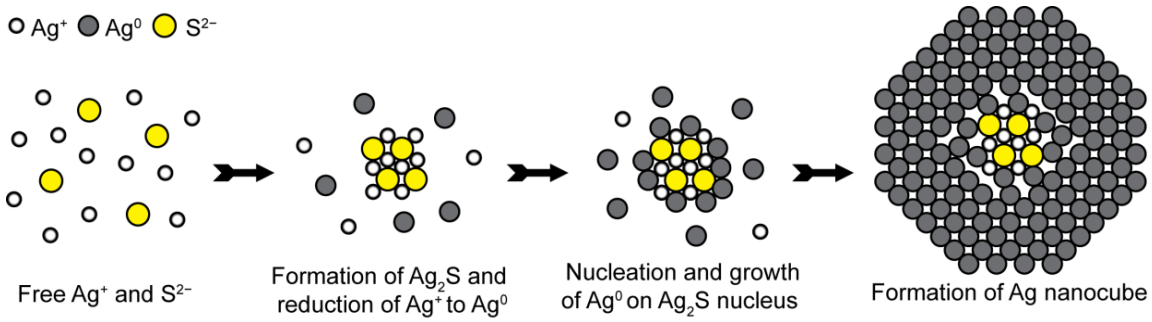

Figure 2.8. Schematic illustration showing the formation of Ag nanocubes through heterogeneous nucleation and growth on Ag_2S-based nuclei, enabled by the addition of a trace amount of SH^-. The Ag_2S nuclei are immediately formed upon the introduction of a Ag^+ precursor, followed by the deposition of Ag^0 atoms to yield Ag nanocubes. (Reprinted with permission from [50]. Copyright 2016 American Chemical Society.)

The removal of free SH^- ions essentially blocks the initial formation of Ag_2S clusters. As a result, the initial nucleation of Ag atoms has to proceed through a homogenous route, with the newly formed Ag^0 atoms being likely oxidized back to Ag^+ *via* a combination of the dissolved H_2S and O_2 to generate insoluble Ag_2S. However, due to the higher energies needed to drive homogeneous nucleation relative to heterogeneous nucleation, this indirect process produces far fewer Ag_2S clusters when compared with the proposed direct formation of Ag_2S from Ag^+ and SH^- ions. In turn, this allows for a high concentration of Ag precursor to remain in the reaction solution, resulting in rapid growth for the nanocrystals and the formation of large Ag nanocubes, as shown in Figure 2.9, A and B. I have attempted to quantify the amount of S present in the Ag nanocubes with both inductively coupled plasma mass spectrometry (ICP-MS) and energy-dispersive X-ray spectroscopy (EDX) elemental mapping. In the case of the former, the S signal was

interfered with by signals from Ar and O_2, both of which are present in large quantities during a measurement under ambient conditions, thus precluding accurate analysis. In the case of the latter, the collected S signal was below the noise level of the EDX measurement, due to a very small S/Ag elemental ratio.

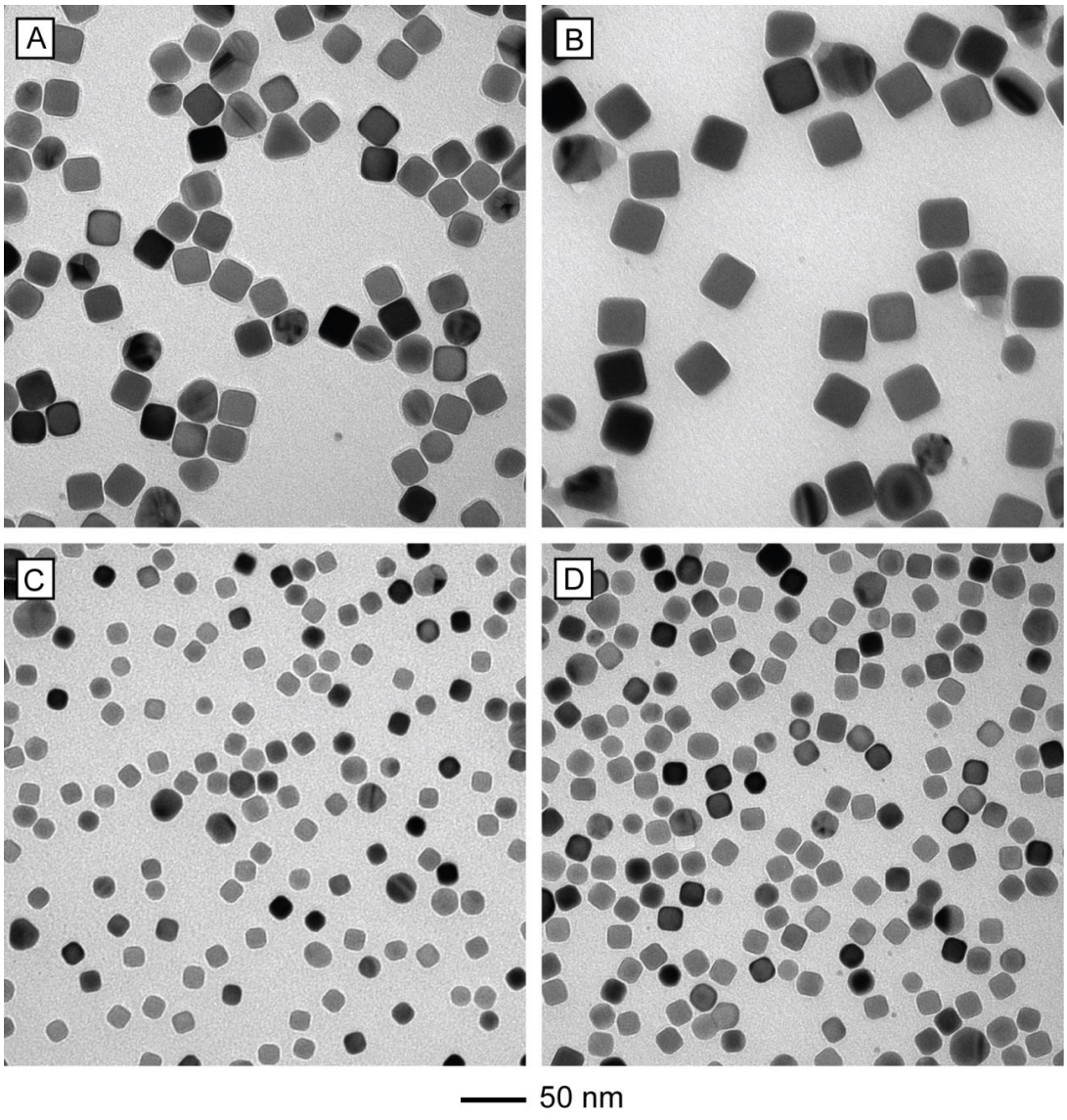

Figure 2.9. TEM images of reaction products obtained in the presence of (A, B) HCl and (C, D) NaCl, together with growth times of (A, C) 15 min and (B, D) 25 min, respectively. All other conditions were kept the same as in the standard synthesis. (Reprinted with permission from [50]. Copyright 2016 American Chemical Society.)

By substituting HCl with NaCl, the source of protons would be removed from the system, thus restoring the original Ag_2S cluster formation mechanism. Figure 2.9, C and D, shows the product of a standard synthesis collected at 20 and 30 min after the addition of the Ag precursor, respectively, with NaCl substituting HCl as the source of Cl^- while no NaBr was added. The average edge length was measured to be 15.2±0.6 and 18.1±0.5 nm at 20 and 30 min post Ag precursor addition, respectively, corresponding to a 69% increase in volume for the Ag nanocubes over 10 min. This value is less than half of the rate of growth seen in the HCl-mediated synthesis. The significantly slower growth rate suggests the formation of a larger number of Ag_2S clusters during the nucleation stage as compared to the HCl system. The result is the rapid consumption of available Ag precursor, slowing down the growth and thus generating smaller Ag nanocubes.

Previous work has shown that EG oxidizes into glycolaldehyde in the presence of dissolved O_2 and temperatures above 100 °C [47, 48]. The glycolaldehyde acts as the primary reducing agent, being oxidized further into a carboxylic acid and producing protons in the process. Additional H^+, introduced by the HCl, can slow the oxidation of glycolaldehyde, thus inhibiting the reduction process and slowing the nanocube nucleation and growth. The removal of these protons in the case of the NaCl-based synthesis would have the opposite effect. In either case, however, the trace amounts of H^+ (~191 μM) introduced with the HCl should have no significant impact on pH and reduction kinetics. Furthermore, previous attempts to increase the reduction kinetics by increasing temperature have not produced smaller Ag nanocubes [38]. Therefore, the decrease in size for the nanocubes can be largely attributed to the increased number of heterogeneous nucleation sites in the reaction system.

To further study the influence of SH^- on the size of Ag nanocubes, I conducted syntheses at various concentrations of NaSH without the addition of NaBr. Figure 2.10 shows TEM images of the products obtained from syntheses that were undersupplied (Figure 2.10A) and oversupplied with SH^- (Figure 2.10B) compared to the standard SH^-

concentration. Specifically, the nanoparticles in Figure 2.10A were prepared using a 0.58 mM NaSH solution, which corresponds to one-sixth the standard concentration, and those in Figure 2.10B were obtained with a 7 mM NaSH solution, corresponding to twice the standard concentration. In the former case, Ag nanocubes with an average edge length of ~23 nm were obtained, along with a large fraction of multiply-twinned nanoparticles. The latter produced a majority fraction of ~7 nm spherical particles and a minor fraction of ~30 nm cuboctahedra, shown in the inset of Figure 2.10B.

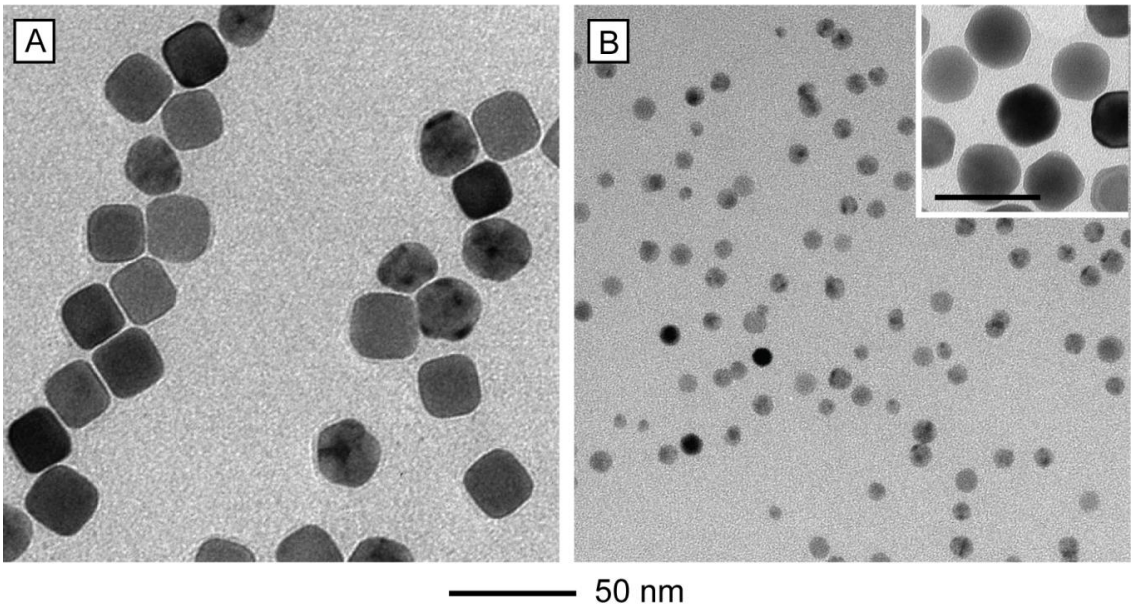

Figure 2.10. TEM images of reaction products obtained with the use of NaSH solutions at different concentrations: (A) 0.6 mM and (B) 6 mM, respectively. All other conditions were kept the same as in the standard synthesis. The inset in (B) shows the minority product fraction, consisting of ~30 nm Ag cuboctahedra. The cuboctahedra in the minority fraction formed a coffee ring pattern on the TEM grid, thereby isolating them from the bulk of the imaged sample. The scale bar in the inset corresponds to 50 nm. (Reprinted with permission from [50]. Copyright 2016 American Chemical Society.)

The cuboctahedra in the minority fraction formed a coffee ring pattern on the TEM grid, thereby effectively isolating them from the bulk of the imaged sample. Notably, the larger cuboctahedra were likely produced in the first moments after the mixing of the Ag precursor, with the slow subsequent growth failing to narrow the overall size distribution of the product. These results are consistent with my established hypothesis: a lower

concentration of SH^- resulted in fewer Ag_2S clusters for heterogeneous nucleation and thus larger Ag nanocubes, while a higher-than-standard concentration of SH^- produced too many Ag_2S nuclei, which consumed the Ag precursor too quickly and resulted in smaller cuboctahedra. These cuboctahedra likely failed to develop into nanocubes due to the lack of sufficient Ag for growth, as well as the inability of the long-chain PVP macromolecules to stabilize the {100} facets at such a small size.

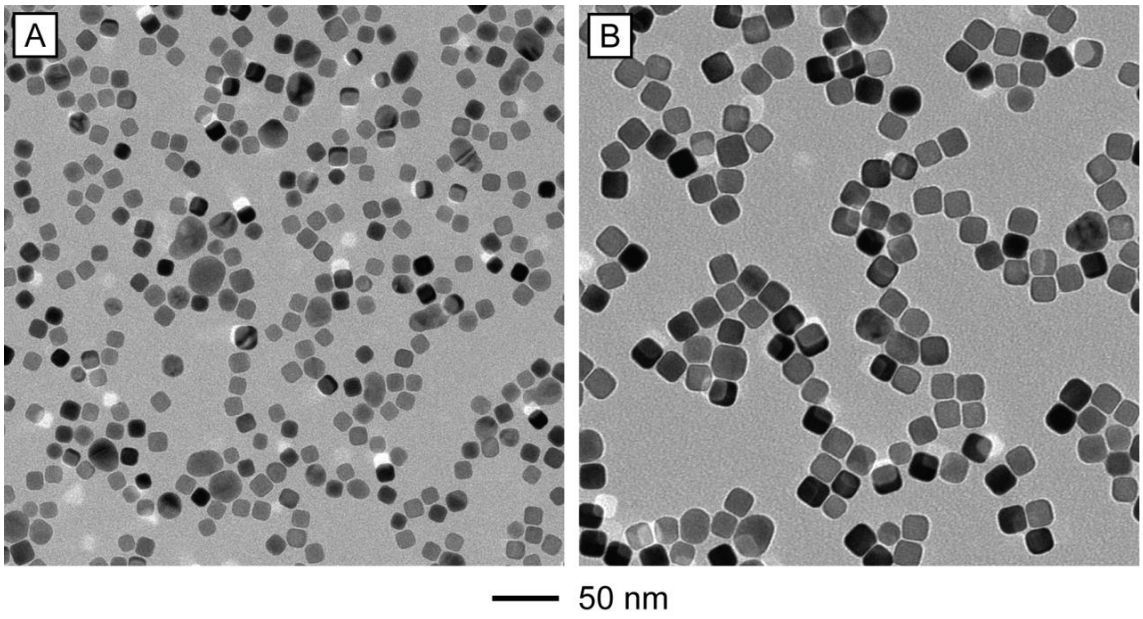

Figure 2.11. TEM images of Ag nanocubes produced by substituting the $NaHS \cdot 1.5H_2O$ used in the standard procedure with an equal molar concentration of $Na_2S \cdot 9H_2O$, with different delay times. The average edge lengths of the nanocubes were: (A) 12.7±0.5 and (B) 18.1±0.7 nm. The delay times used were: (A) 5 and (B) 25 min. (Reprinted with permission from [50]. Copyright 2016 American Chemical Society.)

Finally, in order to rule out the possible influence of the sulfide source, I performed a set of control experiments, in which I substituted $NaHS \cdot 1.5H_2O$ in the standard procedure with the same molar concentration of $Na_2S \cdot 9H_2O$. Figure 2.11 shows TEM images of Ag nanocubes with average edge lengths of 12.7±0.5 and 18.1±0.7 nm produced with the addition of Na_2S by varying the delay time from 5 to 25 min, respectively. These results suggest that good quality nanocubes could be produced irrespective of whether S^{2-} or SH^- was introduced into the reaction system, which is consistent with previous findings [37].

However, it should be pointed out that $NaHS \cdot 1.5H_2O$ is less hygroscopic and therefore much easier to accurately weight out in small quantities during preparation, allowing for greater synthetic reproducibility.

The Influence of Br^- Ions. The impact of introducing a trace amount of Br^- into the reaction system is twofold. Firstly, the bromide ions can act as a selective capping agent toward the Ag{100} facets, thereby promoting the formation of nanocrystals with a cubic shape. This behavior has been well studied with regard to the one-pot synthesis of Pd nanocubes/nanobars and seeded growth of Ag nanospheres into nanobars [31, 43]. In contrast to the latter, the product of the synthesis presented herein consists largely of nanocubes, with some nanobars emerging at extended growth times (Figure 2.4, C and D). Secondly, the Br^- ions quickly bind with the remaining Ag^+ ions in the reaction solution, forming largely insoluble AgBr ($K_{sp} = 10^{-14}$) and effectively abstracting nearly all available Ag precursor from the reaction. The addition of NaBr after a certain delay time effectively delineates the point between fast and slow reduction kinetics, with the formation of single-crystal seeds occurring during the former and the growth of nanocubes proceeding during the latter. The AgBr precipitate can be easily collected and removed through centrifugation after the reaction has been completed. The remaining Ag atoms grow on the {111} facets of the nucleated Ag cuboctahedra, as directed by the capping of Br^- toward the Ag(100) surface, to generate the corners on the final nanocubes. As discussed previously, all subsequent growth for the nanocubes was extremely slow, with Ag atoms involved in the growth likely released through the dissolution of initially formed AgCl precipitates and Cl^--mediated oxidative etching. Additionally, the lack of a significant population of Ag nanobars, even at prolonged growth times, is likely due to the rapid rate of diffusion for Ag atoms on the surface, significantly exceeding the rate of growth [49]. As a result, there is a more or less even distribution of Ag atoms across the entire surface of a growing nanocrystal, thus producing nanocubes rather than nanobars as the major product fraction.

In order to explore the influence of Br^- concentration on the morphology of final

products, I conducted a set of experiments with different amounts of Br^- being introduced. Figure 2.12 shows the products obtained using the standard procedure, except for the variation in NaBr concentration. When no NaBr was added, the synthesis yielded a mixture of Ag cuboctahedra and nanocubes, with an average edge length of 15.3±0.7 nm, as shown in Figure 2.12A. When the concentration of NaBr was increased, a decrease in both nanocube uniformity and product purity was observed (Figure 2.12, B−D). The polydispersity of size, in the range of 13-23 nm, as well as the emergence of a significant fraction of large, rounded nanoparticles, suggests that higher concentrations of NaBr further slow down the reaction kinetics in the growth stage of the synthesis. While the exact mechanism is still unclear, it is possible that the excessive Br^- ions could abstract the Ag^+ ions produced by secondary pathways, such as oxidative etching and Oswald ripening, effectively starving the system of growth material and thereby leading to the aberrant growth regimes seen in Figure 2.12, C and D.

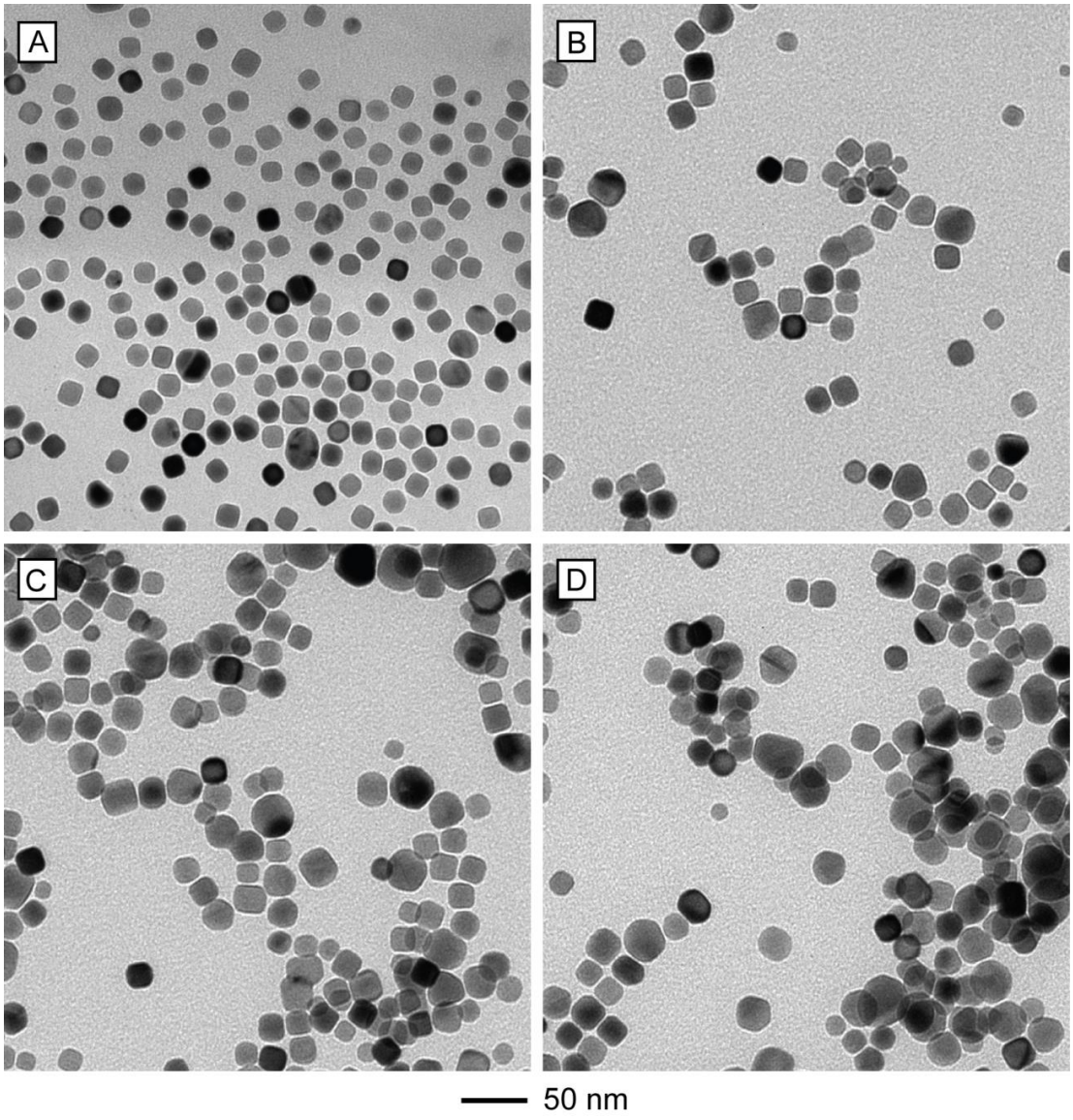

Figure 2.12. TEM images of reaction products obtained with the use of NaBr solutions at different concentrations: (A) 0, (B) 15, (C) 30, and (D) 90 mM. The growth time was 15 min, while all other parameters were kept the same as in the standard synthesis. (Reprinted with permission from [50]. Copyright 2016 American Chemical Society.)

2.3 Conclusion

In summary, I have successfully developed an EG-based method for generating well-defined Ag nanocubes with edge lengths below 15 nm. The success of this method relies on a combination of the effective capping of small Ag{100} facets by Br^- ions and control over the number of nuclei initially formed in the reaction system. The latter was enabled

by a new understanding of the mechanistic effects of SH^- additives, achieved over the course of this work. The substitution of HCl by NaCl as the chloride source, improved upon previous synthetic methods, resulting in a greatly enhanced effectiveness of the SH^- additive in controlling the nucleation of Ag atoms. As a result, the variation of SH^- concentration was shown to be the most effective means for controlling the edge length of Ag nanocubes. The Br^- ions acted both as a capping agent toward the Ag(100) surface, and as a kinetic regulator by limiting the number of free Ag^0 atoms present in the reaction solution. The resultant Ag nanocubes are both smaller and sharper at edges when compared with those reported in previous work. The edge length of the nanocubes could be readily varied from 13 to 23 nm by quenching the synthesis after different periods of growth. The nanocube yield was estimated to be ~90%, and subsequent experiments have shown this approach to be both highly reproducible and readily scalable.

2.4 Experimental Section

Chemicals and Materials. Ethylene glycol (EG, ≥99.0%) was obtained from J. T. Baker (batch no. 0000034605). Silver trifluoroacetate (CF_3COOAg, ≥99.99%), sodium hydrosulfide hydrate ($NaHS \cdot 1.5H_2O$), aqueous hydrochloric acid solution (HCl, 37%), poly(vinyl pyrrolidone) (PVP, MW≈55,000), sodium chloride (NaCl, ≥99.0%), sodium bromide (NaBr, ≥99.0%) and sodium sulfide nonahydrate ($Na_2S \cdot 9H_2O$) were all obtained from Sigma-Aldrich. All chemicals were used as received. Deionized (DI) water with a resistivity of 18.2 MΩ·cm was used throughout the experiment. The synthesis of Ag nanocrystals was carried out in a 100 mL flask with round bottom (ACE Glass).

Synthesis of Ag Nanocubes. In a standard synthesis, 25 mL of EG was added into a flask and heated for 40 min under magnetic stirring in an oil bath set to 142 °C. A stable temperature of approximately 135°C was measured for the reaction solution. Other reagents were separately dissolved in EG and sequentially introduced into the flask using a pipet. Specifically, 0.3 mL of NaSH solution (3.5 mM) was added first. After 4 min, 2.5

mL of NaCl solution (3 mM) was introduced, followed by 6.25 mL of PVP solution (20 mg/mL) 2 min later. After another 2 min, 2 mL of CF_3COOAg solution (282 mM) was introduced. Finally, 2.5 mL of NaBr solution (3 mM) was added after 5 min of delay. Note that the NaSH solution was prepared immediately before its injection. During the entire process, the flask was capped with a glass stopper except during the addition of reagents. The synthesis was quenched by immersing the flask in an ice-water bath. The solution was split into four portions and 125 mg of PVP was dissolved in each fraction. This is necessary in order to prevent aggregation during the washing steps. The products were precipitated with acetone and collected by centrifugation at 6000 RPM for 10 min, followed by washing with DI water and centrifuging at 15000 RPM for 15 min twice to remove the remaining precursor, EG, and excess PVP. If NaBr was used during the synthesis, the product solution was twice centrifuged at 4000 RPM for 30 min in order to separate the insoluble AgBr precipitate from the Ag nanocube solution.

Instrumentation. Transmission electron microscopy images were obtained using a Hitachi HT7700 microscope operated at 120 kV. UV-vis absorption spectra were recorded with a Lambda 750 spectrometer (PerkinElmer). An Eppendorf centrifuge (5430) was used for the collection and washing of all samples.

Nanocube Edge Length Analysis Methodology. The edge lengths of the produced Ag nanocubes were determined by analyzing TEM images with ImageJ software, with the averages and standard deviations calculated using functions built into Microsoft Excel. For each edge length analysis, 150 randomly selected (*i.e.* picked by the ImageJ software) nanocubes were used and the large, irregular nanoparticles were excluded from the analysis.

2.5 Notes to Chapter 2

Part of this chapter is adapted from the paper “Toward the Synthesis of Sub-15 nm Ag Nanocubes with Sharp Corners and Edges: The Roles of Heterogeneous Nucleation and

Surface Capping" published in the *Journal of the American Chemical Society* [50].

2.6 References

[1] Rycenga, M.; Cobley, C. M.; Zeng, J.; Li, W.; Moran, C. H.; Zhang, Q.; Qin, D.; Xia, Y. *Chem. Rev.* **2011**, *111*, 3669−3712.

[2] Jin, R.; Cao, Y.; Mirkin, C. A.; Kelly, K. L.; Schatz, G. C.; Zheng, J. G. *Science* **2001**, *294*, 1901−1903.

[3] Jana, N. R.; Gearheart, L.; Murphy, C. J. *Chem. Commun.* **2001**, 617−618.

[4] Sun, Y.; Xia, Y. *Science* **2002**, *298*, 2176−2179.

[5] Tao, A. R.; Sinsermsuksakul, P.; Yang, P. *Angew. Chem., Int. Ed.* **2006**, *45*, 4597−4601.

[6] Zhang, J.; Li, S.; Wu, J.; Schatz, G. C.; Mirkin, C. A. *Angew. Chem. Int. Ed.* **2009**, *48*, 7787−7791.

[7] Murshid, N.; Kitaev, V. *Chem. Commun.* **2014**, *50*, 1247-1249.

[8] Keunen, R.; Cathcart, N.; Kitaev, V. *Nanoscale* **2014**, *6*, 8045–8051.

[9] Xia, X.; Zeng, J.; Zhang, Q.; Moran, C. H.; Xia, Y. *J. Phys. Chem. C* **2011**, *116*, 21647-21656.

[10] Langille, M. R.; Personick, M. L.; Mirkin, C. A. *Angew. Chem. Int. Ed.* **2013**, *52*, 2–33.

[11] Wiley, B. J.; Im, S. H.; Li, Z.-Y.; McLellan, J.; Siekkinen, A.; Xia, Y. *J. Phys. Chem. B* **2006**, *110*, 15666-15675.

[12] Lu, G.; Keersmaecker, H. D.; Su, L.; Kenens, B.; Rocha, S.; Fron, E.; Chen, C.; Dorpe, P. V.; Mizuno, H.; Hofkens, J.; Hutchsion, J. A.; Uji-I, H. *Adv. Mater.* **2014**, *26*, 5124–5128.

[13] Zeng, S.; Baillargeat, D.; Ho, H.-P.; Yong, K.-T. *Chem. Soc. Rev.* **2014**, *43*, 3426-3452.

[14] Xue, B.; Wang, D.; Zuo, J.; Kong, X.; Zhang, Y.; Liu, X.; Tu, L.; Chang, Y.; Li, C.;

Wu, F.; Zeng, Q.; Zhao, H.; Zhao, H.; Zhang, H. *Nanoscale* **2015**, *7*, 8048-8057.

[15] Lee, S.; Shin, S.; Lee, S.; Seo, J.; Lee, J.; Son, S.; Cho, H. J.; Algadi, H.; Al-Sayari, S.; Kim, D. E.; Lee, T. *Adv. Funct. Mater.* **2015**, *25*, 3114–3121.

[16] Mayousse, C.; Celle, C.; Fraczkiewicz, A.; Simonato, J.-P. *Nanoscale* **2015**, *7*, 2107-2115.

[17] Kawawaki, T.; Wang, H.; Kubo, T.; Saito, K.; Nakazaki, J.; Segawa, H.; Tatsuma, T. *ACS Nano*, **2015**, *9*, 4165-4172.

[18] Linic, S.; Christopher, P.; Xin, H.; Marimuthu, A. *Acc. Chem. Res.* **2013**, *46*, 1890–1899.

[19] Stark, W. J.; Stoessel, P. R.; Wohlleben, W.; Hafner, A. *Chem. Soc. Rev.* **2015**, *44*, 5793-5805.

[20] Verano-Braga, T.; Miethling-Graff, R.; Wojdyla, K.; Rogowska-Wrzesinska, A.; Brewer, J. R.; Erdmann, H.; Kjeldsen, F. *ACS Nano* **2014**, *8*, 2161–2175.

[21] Mu, Q.; Jiang, G.; Chen, L.; Zhou, H.; Fourches, D.; Tropsha, A.; Yan, B. *Chem. Rev.* **2014**, *114*, 7740–7781.

[22] Liang, R.; Wei, M.; Evans, G. E.; Duan, X. *Chem. Commun.* **2014**, *50*, 14071-14081.

[23] Le Ouay, B.; Stellacci, F.; *Nanotoday* **2015**, *10*, 339-354.

[24] Sherry L. J.; Chang, S.-H.; Schatz, G. C.; Van Duyne, R. P. *Nano Lett.* **2005**, *5*, 2034–2038.

[25] Konig, T. A. F.; Ledin, P. A.; Kerszulis, J.; Mahmoud, M. A.; El-Sayed, M. A.; Reynolds, J. R.; Tsukruk, V. V. *ACS Nano* **2014**, *8*, 6182–6192.

[26] Klimov, V.; Guo, G.-Y.; Pikhota, M. *J. Phys. Chem. C*, **2014**, *118*, 13052–13058.

[27] Bordley, J. A.; Hooshmand, N.; El-Sayed, M. A. *Nano Lett.* **2015**, *15*, 3391–3397.

[28] Li, G.; Cherqui, C.; Bigelow, N. W.; Duscher, G.; Straney, P. J.; Millstone, J. E.; Masiello, D. J.; Camden, J. P. *Nano Lett.* **2015**, *15*, 3465–3471.

[29] Yang, Y.; Matsubara, S.; Xiong, L.; Hayakawa, T.; Nogami, M. *J. Phys. Chem. C* **2007**, *111*, 9095-9104.

[30] Prezgot, D.; Ianoul, A. *J. Phys. Chem. C*, **2015**, *119*, 3293–3301.

[31] Zhang, Q.; Moran, C. H.; Xia, X.; Rycenga, M.; Li, N.; Xia, Y. *Langmuir* **2012**, *28*, 9047-9054.

[32] Christopher, P.; Linic, S. *J. Am. Chem. Soc.* **2008**, *130*, 11264-11265.

[33] Christopher, P.; Linic, S. *ChemCatChem* **2010**, *2*, 78-83.

[34] Skrabalak, S. E.; Chen, J.; Sun, Y.; Lu, X.; Au, L.; Cobley, C. M.; Xia, Y. *Acc. Chem. Res.* **2008**, *41*, 1587-1595.

[35] Xia, X.; Wang, Y.; Ruditskiy, A.; Xia, Y. *Adv. Mater.* **2013**, *25*, 6313-6333.

[36] Im, S. H.; Lee, Y. T.; Wiley, B.; Xia, Y. *Angew. Chem. Int. Ed.* **2005**, *44*, 2154 – 2157.

[37] Siekkinen, A. R.; McLellan, J. M.; Chen, J.; Xia, Y. *Chem. Phys. Lett.* **2006**, *432*, 491-496.

[38] Zhang, Q.; Li, W.; Wen, L.-P.; Chen, J.; Xia, Y. *Chem. Eur. J.* **2010**, *16*, 10234-10239.

[39] Wang, Y.; Zheng, Y.; Huang, C. Z.; Xia, Y. *J. Am. Chem. Soc.* **2013**, *135*, 1941-1951.

[40] Wiley, B. J.; Chen, Y.; McLellan, J. M.; Xiong, Y.; Li, Z.-Y.; Ginger, D.; Xia, Y. *Nano. Lett.* **2007**, *7*, 1032-1036.

[41] Wiley, B. J.; Xiong, Y.; Li, Z.-Y.; Yin, Y.; Xia, Y. *Nano Lett.* **2006**, *6*, 765-768.

[42] Jin, M.; Liu, H.; Zhang, H.; Xie, Z.; Liu, J.; Xia, Y. *Nano Res.* **2011**, *4*, 83-91.

[43] Peng, H.-C.; Xie, S.; Park, J.; Xia, X.; Xia, Y. J. Am. *Chem. Soc.* **2013**, *135*, 3780-3783.

[44] Zheng, Y.; Zeng, J.; Ruditskiy, A.; Liu, M.; Xia Y. *Chem. Mater.* **2014**, *26*, 22-33.

[45] Jou, F.-Y.; Deshmukh, R. D.; Otto, F. D.; Mather, A. E. *Chem. Eng. Comm.* **1990**, *87*, 223-231.

[46] Short, I.; Sahgal, A.; Hayduk, W. *J. Chem. Eng. Data* **1983**, *28*, 63-66.

[47] Skrabalak, S. E.; Wiley, B. J.; Kim, M; Formo, E. V.; Xia, Y. *Nano Lett.* **2008**, *8*, 2077–2081.

[48] Zhang, Q.; Cobley, C.; Au, L.; McKiernan, M.; Schwartz, A.; Wen, L.-P.; Chen, J.; Xia, Y. *ACS Appl. Mater. Interfaces* **2009**, *1*, 2044–2048.

[49] Xia, X.; Xie, S.; Liu, M.; Peng, H.-C.; Lu, N.; Wang, J.; Kim, M. J.; Xia, Y. *Proc. Natl. Acad. Sci. U. S. A.* **2013**, *110*, 6669–6673.

[50] Ruditskiy, A.; Xia, Y. *J. Am. Chem. Soc.* **2016**, *138*, 3161–3167.

CHAPTER 3

A QUANTITATIVE UNDERSTANDING OF THE SULFATE-MEDIATED SYNTHESIS OF PALLADIUM DECAHEDRAL NANOCRYSTALS

3.1 Introduction

Shape-controlled syntheses of noble-metal nanocrystals have been a subject of active research, as discussed in Chapter 1. In particular, there is a strong interest in producing Pd nanocrystals with multi-twinned structures, such as icosahedra [1−7] and decahedra [5−7], which can be used in a number of applications such as electrocatalysis [2, 8] and hydrogen storage [9]. Furthermore, these multi-twinned nanocrystals can serve as seeds or templates for the generation of more complex and/or multi-metallic nanostructures, such as core-shells [10−14], nanoframes [14−16], and nanorods [17−19]. The ultimate utility of decahedral nanocrystals relies on the ability to produce them with high conversion and morphology yields, together with a high degree of consistency.

The most commonly used method for the synthesis of noble-metal nanocrystals is based upon the one-pot approach. The outcome of such an approach depends on two major aspects: *i*) the synthesis itself, which produces the desired nanocrystals and *ii*) the washing process, which serves to purify the products by removing excess chemical species. The latter step is often achieved through repeated centrifugation of the products and re-dispersion of the precipitated material in a proper solvent, while discarding the supernatant. However, the specifics of this process, such as the centrifugation speed and duration, can often obscure the true nature of the nanocrystal product. In particular, the discarded supernatant may often contain nanocrystals that are too small to be effectively collected at a certain centrifugation speed. As such, these small particles are often ignored in the published work, portraying an incomplete picture of the synthetic process. One example of

this problem can be found in the recently developed sulfate-mediated synthesis of multi-twinned Pd decahedra [6]. While the standard procedure generates uniform decahedral nanocrystals with high purity, the significant loss of Pd during the washing step results in the waste of a precious material. Furthermore, the identity of the discarded nanocrystals, as well as the reasons behind their formation, remain unexplored.

In this work, I conducted a systematic and quantitative study of the sulfate-mediated polyol synthesis of Pd decahedra. Inductively coupled plasma mass spectrometry (ICP-MS) was used to quantify the Pd contents for both the typically recovered and discarded Pd nanocrystal populations present in the synthetic products at different reaction times, as well as that of the unreacted Pd precursor. The initial nucleation process was analyzed with transmission electron microscopy (TEM) in order to ascertain the cause behind the size disparity between the Pd nanocrystal populations. Kinetic data was collected with UV-vis spectroscopy in an attempt to quantify the impact of the sulfate additive on the initial reduction rates in the standard synthesis. Finally, the addition of ascorbic acid (AA) as a secondary reducing agent after the initial polyol-induced nucleation of Pd nanocrystals was demonstrated as an effective means to improve the conversion efficiency of the precursor without compromising the quality of the final decahedral products.

3.2 Results and Discussion

Figure 3.1 shows the ICP-MS-derived Pd contents in the various product fractions for a standard polyol synthesis of Pd decahedra. The products were physically separated into three fractions through centrifugation at different speeds, as detailed in the experimental section. The three fractions can be generally classified as the larger Pd decahedra with sizes >12 nm, smaller Pd particles with sizes of 4-11 nm, and the unreacted Na_2PdCl_4 precursor remaining in the reaction mixture. It should be noted that the decahedra constitute the products typically collected at the end of a standard synthesis protocol, while the0 smaller particles and the unreacted precursor were discarded. The unreacted precursor may include

some Pd clusters and Pd ultrafine particles. The products were collected after different periods of time ranging from 3 to 48 h, with 3 h being the typical reaction time previously reported in the literature [7].

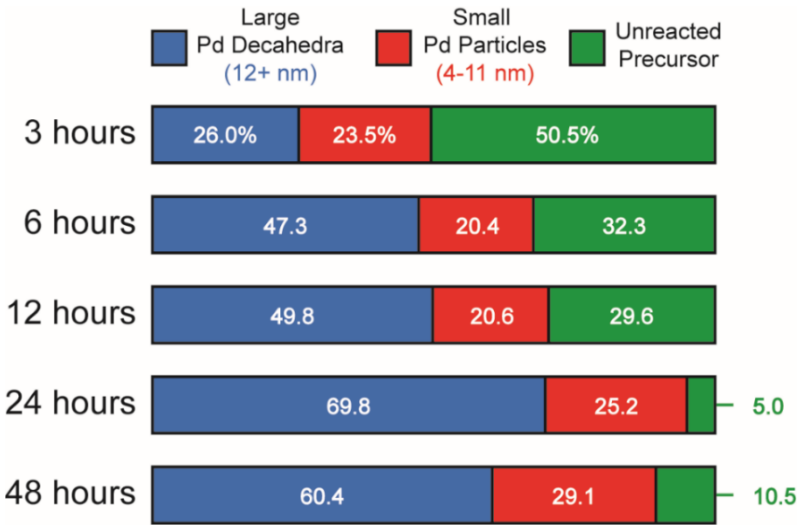

Figure 3.1. ICP-MS-derived Pd contents in the various fractions separated from the products of a standard synthesis terminated at 3, 6, 12, 24, and 48 h. The larger Pd decahedra were separated from the reaction solution by centrifugation at 16500 RPM for 25 min, while the smaller particles were isolated by centrifugation of the recovered supernatant at 55000 RPM for 90 min. Here the "unreacted precursor" may include the original Na_2PdCl_4 precursor, Pd clusters, and ultrafine Pd particles. (Reprinted with permission from [32]. Copyright 2016 American Chemical Society.)

The ICP-MS results for a reaction time of 3 h revealed that only 26% of the initially added Pd(II) precursor was converted into the larger decahedra, with 23.5% and 50.5% of the remainder contained in the smaller particles and unreacted precursor, respectively. Increasing the reaction time to 6, 12, and 24 h resulted in marked increases in the yield of larger decahedra to 47.3, 49.8, and 69.8%, respectively. The percentage of Pd contained in the unreacted precursor fell concomitantly with the increase in decahedra yield. Interestingly, the percentage of the smaller particles present in the products remained at a relatively constant level for these different reaction times, decreasing by ~2% after 6 and 12 h and increasing by ~1.5% after 24 h, relative to the standard reaction time of 3 h. Increasing the reaction time to 48 h, resulted in a 60.4% yield for the larger decahedra,

which showed a decrease of 9.4% as compared to the 24 h reaction. This was likely caused by oxidative etching, a process occurring after the concentration of available Pd(II) precursor dropped below a critical level [20]. Figure 3.2 shows TEM images of the recovered decahedra, suggesting increase in size polydispersity with increasing reaction time indicative of the involvement of Ostwald ripening in the reaction system at longer reaction times.

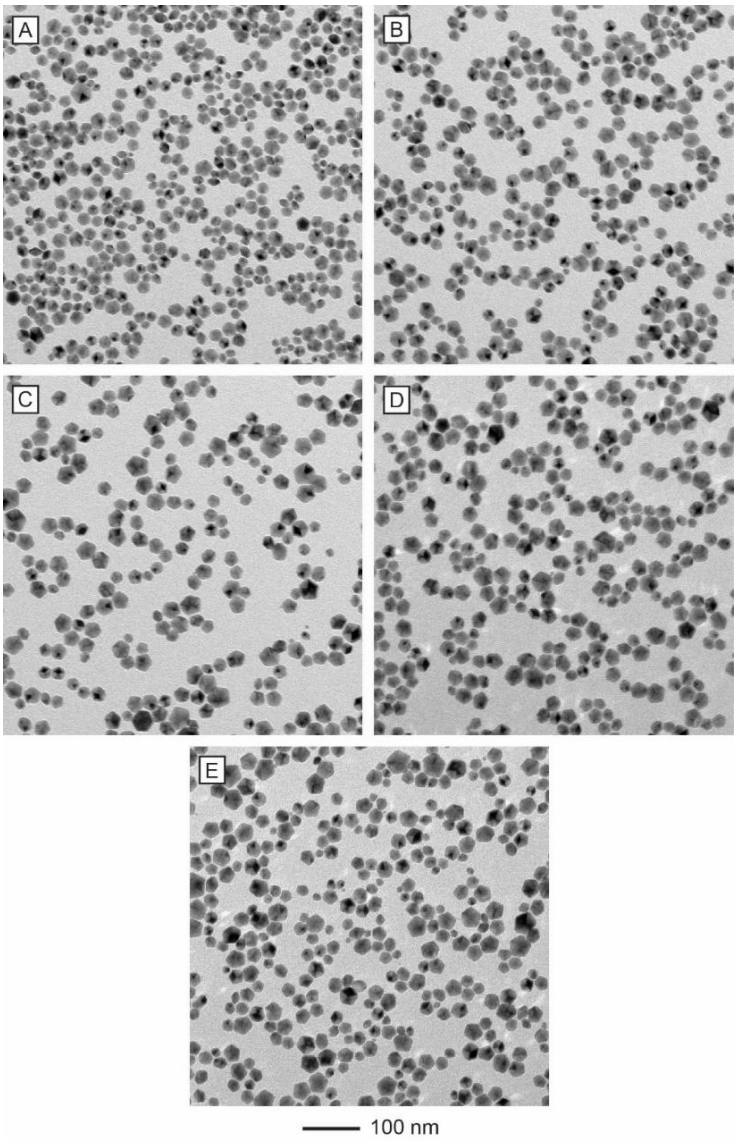

Figure 3.2. TEM images of the Pd decahedra obtained by terminating the standard synthesis after different periods of time: (A) 3 h (14-21 nm in size), (B) 6 h (16-24 nm), (C) 12 h (18-26 nm), (D) 24 h (17-28 nm), and (E) 48 h (16-29 nm). (Reprinted with permission from [32]. Copyright 2016 American Chemical Society.)

Characterizing, and thus determining, the exact morphology of the smaller Pd particles has proven to be technically difficult. Attempts to image the small particles using HRTEM and HAADF-STEM were inconclusive (Figure 3.3). The difficulty stemmed from the small size of the particles in question, as well as the need for extensive washing of the sample prior to imaging. Such treatment may result in degradation of the particle morphology, thereby lowering the reliability of the data. As such, it was necessary to rely on indirect methods for identifying the morphology of the smaller particles. To this end, I employed the recently developed seed-mediated growth of pentagonal Pd nanorods as a proxy for particle identification, since the nanorod synthesis requires decahedra as the seeds [19]. Figure 3.4A shows the as-obtained mixture of both decahedra and smaller particles used as seeds for the synthesis of Pd nanorods. As shown in Figure 3.4B, the products indeed consisted of nanorods with nearly a 100% yield. To ensure that the decahedra were not exclusively responsible for the formation of the nanorods, I used centrifugation to separate them out from the smaller particles prior to their use for nanorod synthesis (Figure 3.4C). The products of the subsequent seed-mediated growth still consisted mostly of nanorods (Figure 3.4D), with a small fraction of single-crystal nanocubes mixed in. The nanocube by-products were likely formed due to the self-nucleation of Pd single-crystal nuclei in the early stage of a nanorod synthesis, with the I^- ions introduced as part of the seeded growth process acting as a capping agent for the {100} side faces [21]. Interestingly, the average diameter of the nanorods seeded using the isolated smaller particles was significantly smaller than that derived from the mixture of seeds. It should be noted that Ag icosahedral particles have been previously used as seeds for the preparation of pentagonal Ag nanorods, due to the similar five-fold twinning structure present in both decahedra and icosahedra [22]. However, the Ag nanorods produced using the latter as seeds showed a pronounced "pin-like" structure, with the icosahedral seed clearly located at one of the nanorod's ends. Such structures were not observed in Figure 3.4, B and D. These results led me to conclude

that the fraction of the smaller particles was itself largely composed of decahedral nanocrystals.

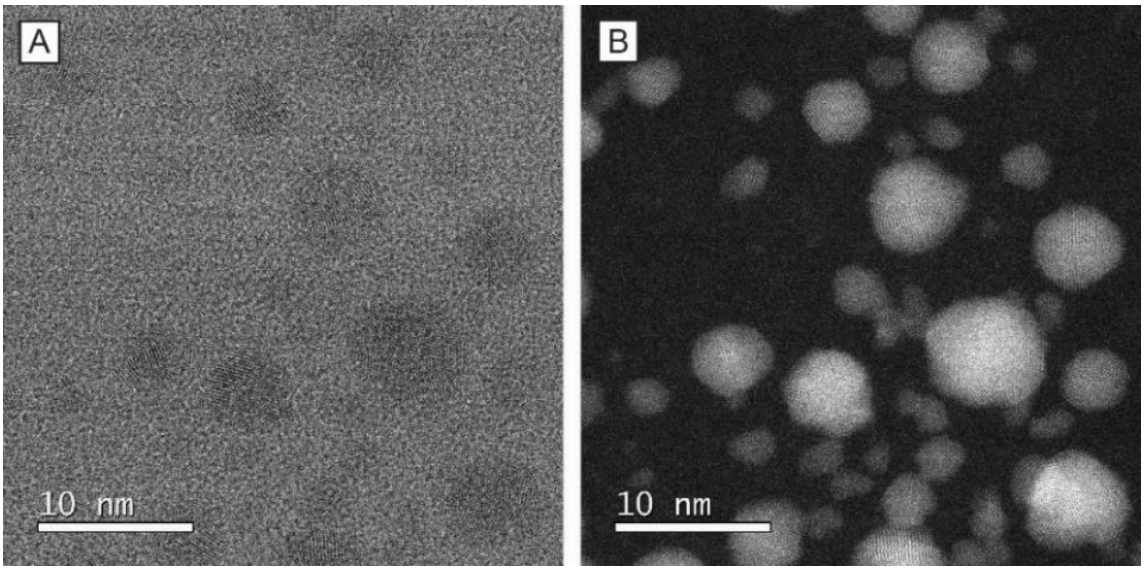

Figure 3.3. (A) HRTEM and (B) HAADF-STEM images of the smaller Pd particles with sizes in the range of 4-11 nm. (Reprinted with permission from [32]. Copyright 2016 American Chemical Society.)

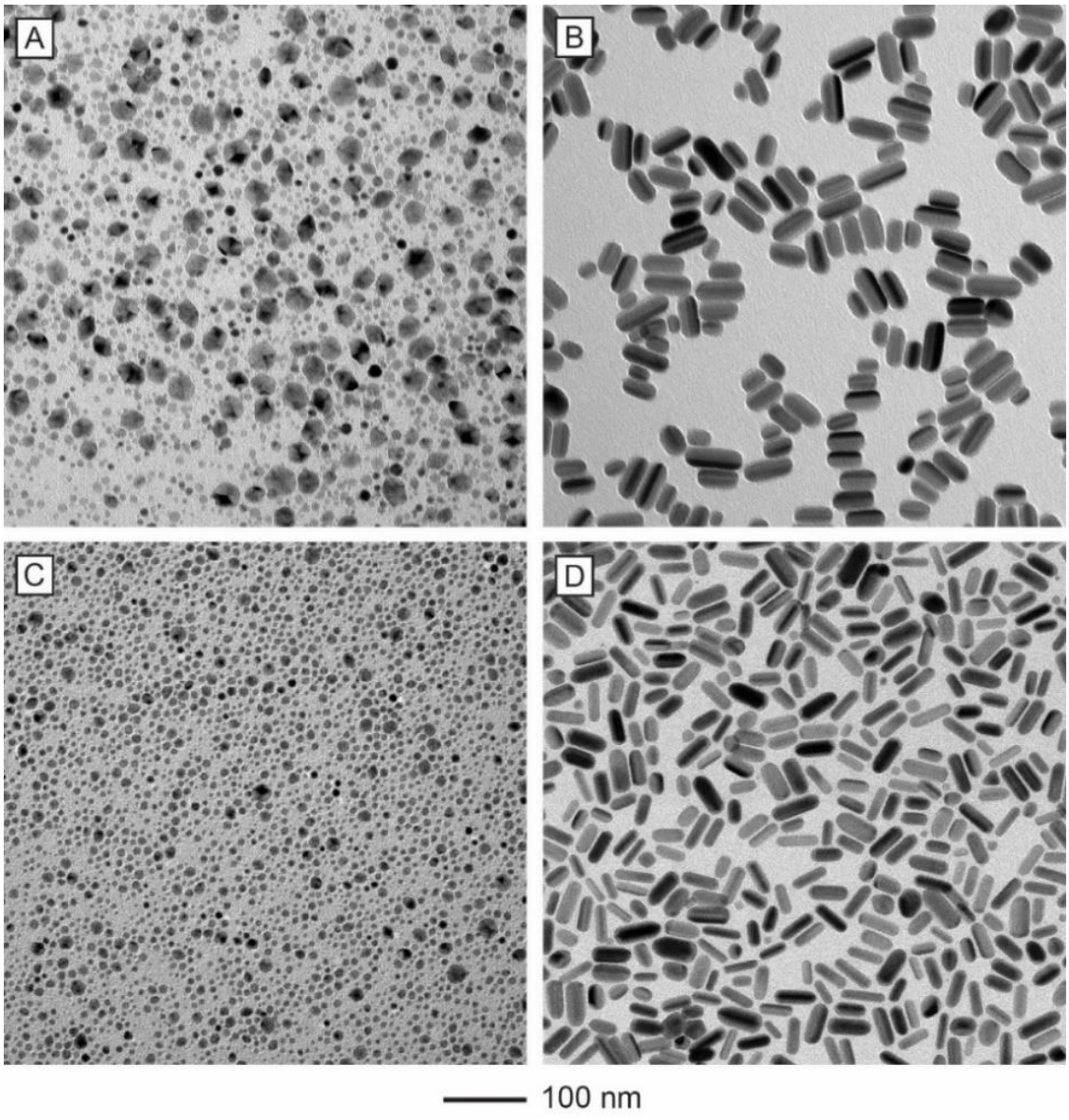

Figure 3.4. TEM images of (A, C) the Pd decahedral seeds and (B, D) the resultant pentagonal nanorods: (A) the as-prepared mixture of products recovered from a standard synthesis through centrifugation at 55000 RPM for 90 min, and (C) the 4-11 nm Pd particles isolated from the mixture in (A) by retaining the supernatant after centrifugation at 16500 RPM for 25 min. (Reprinted with permission from [32]. Copyright 2016 American Chemical Society.)

Since both particle fractions are composed of Pd decahedra, the difference between the two primarily comes down to the disparity in size. In order to investigate this phenomenon, I collected particle samples 5 min after the introduction of the Na_2PdCl_4 precursor and in 5 min intervals thereafter. After the first 5 min (Figure 3.5A), the sample consisted of distinct, pseudo-spherical particles of ~3 nm in diameter. As mentioned previously, it is difficult to ascertain the internal defect structure in this size regime by TEM imaging. To gain some insights into the thermodynamically preferred structure, I took a look at the theoretically derived phase diagram for Pd nanocrystals, which suggests that icosahedra are favored at sizes less than ~2 nm, decahedra at sizes of 2–8 nm, and single-crystals for sizes greater than ~8 nm [23]. Moreover, computationally and experimentally derived phase diagrams of Au particles with different internal defect structures suggest that the size of the particles recovered at 5 min of reaction lies in the border region between the icosahedral and decahedral morphologies at 103 °C [24]. Furthermore, molecular dynamic simulations of Ag nuclei show that the energy barrier to the transformation from icosahedral to decahedral morphology is high beyond the particle size of ~3 nm, making such a transition increasingly energetically unfavorable as the particles grow in size [25]. Taken together, this information implies that the particles recovered after a reaction time of 5 min were decahedral in nature. At 10 min (Figure 3.5B), the particle diameter increased to ~4 nm, while the overall size distribution remained relatively narrow and the particles remained distinct. At 15 min (Figure 3.5C), a population of dumbbell-shaped particles appeared in the sample. These particles were comprised of ~4-5 nm spheres connected by a narrow neck. These structures have been previously shown to be the intermediates of a coalescence process for Au decahedra [26]. At 20 min (Figure 3.5D), the dumbbells largely disappeared and the sample consisted of pseudo-spherical particles with diameters of 4-10 nm. This size disparity persisted throughout the remainder of the time study, as shown in Figure 3.6. Crucially, the ~3 nm spherical particles shown in Figure 3.5A were not present in significant numbers after a reaction time of 5 min. This observation suggests that

homogeneous nucleation did not occur to an appreciable degree after the initial nucleation event, under the standard reaction conditions.

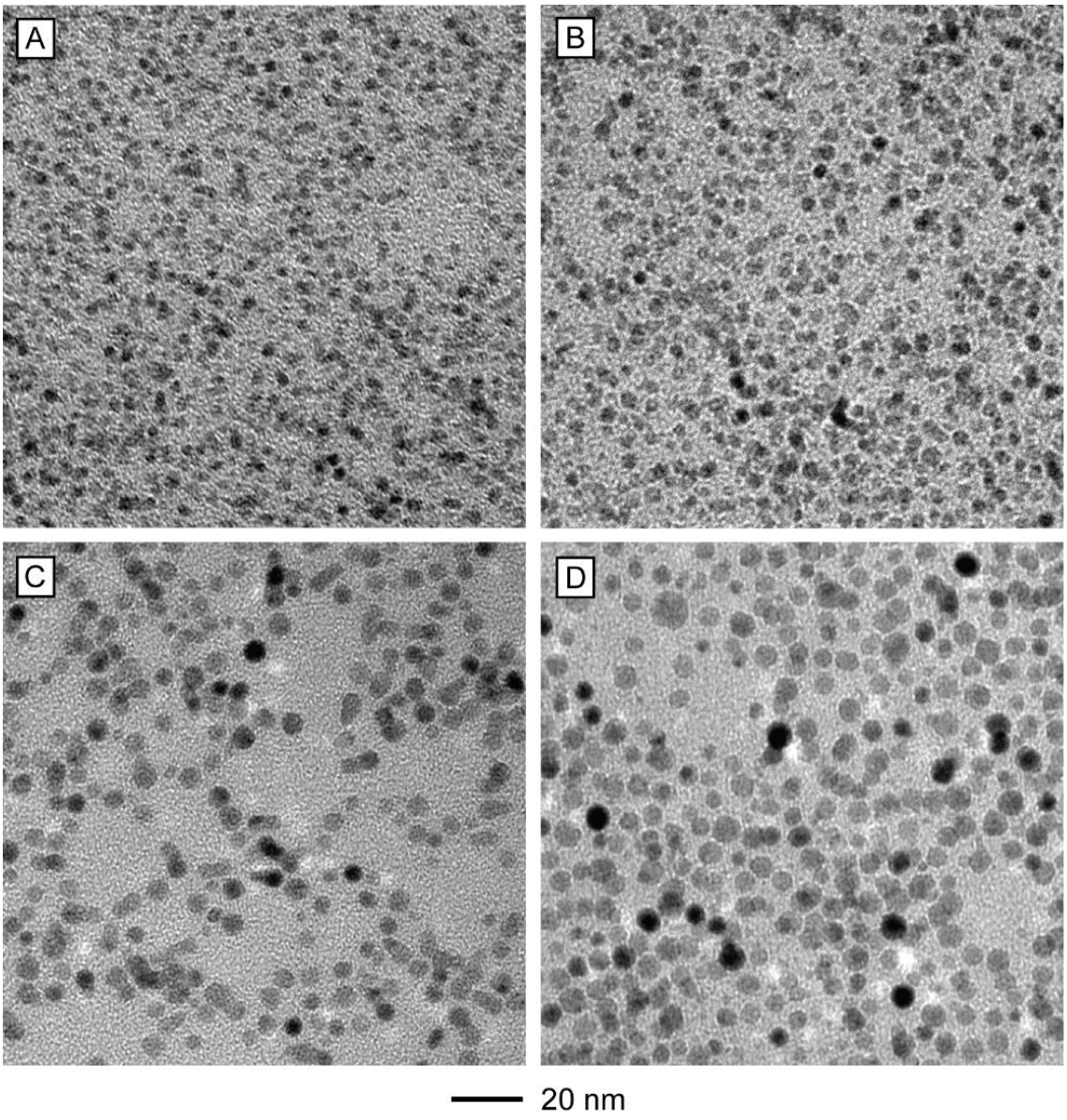

Figure 3.5. TEM images of the Pd particles collected after different periods of time into a standard synthesis: (A) 5, (B) 10, (C) 15, and (D) 20 min. Images for samples collected at subsequent reaction times can be found in Figure 3.6. (Reprinted with permission from [32]. Copyright 2016 American Chemical Society.)

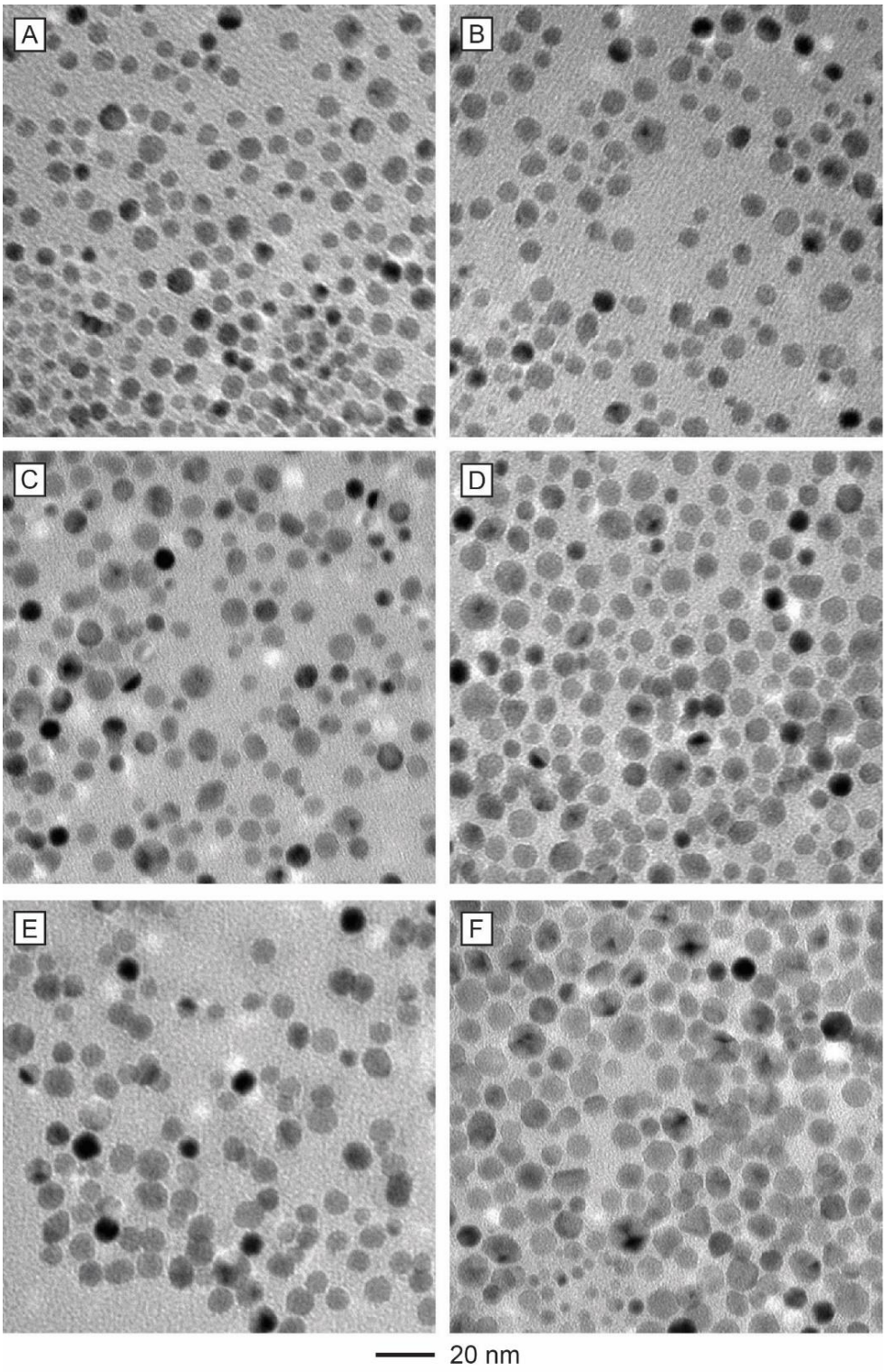

Figure 3.6. TEM images of the Pd particles collected at various time points during a standard synthesis: (A) 25, (B) 30, (C) 35, (D) 40, (E) 45, and (F) 50 min. Images collected at earlier reaction times can be found in Figure 3.5. (Reprinted with permission from [32]. Copyright 2016 American Chemical Society.)

Taken together, I can propose a mechanism to account for the particle size distribution in the polyol synthesis of Pd decahedra. Figure 3.7 shows a mechanistic summary of this process. Initially, the $PdCl_4^{2-}$ precursor is reduced in the polyol environment to produce Pd(0) atoms. When their concentration reaches the level of supersaturation, homogeneous nucleation occurs, thereby forming the ~3 nm decahedral particles with a narrow size distribution. After a period of growth, some of the decahedral particles begin to coalesce, producing the observed dumbbell intermediates. The subsequent internal reorganization of the dumbbells results in the creation of significantly larger decahedral particles relative to their initial components [27]. While the details of the reorganization process are still unclear, I posit that the neck formed during the initial merging event acts as a bridge for the diffusion of Pd atoms from the smaller to the larger component particle, akin to Oswald ripening [26]. Such a process would readily explain the consistent formation of larger decahedra from the coalesced decahedral components at the given reaction temperature. Simultaneously, both the merged and component decahedral particles continue to grow in size due to heterogeneous nucleation and deposition of Pd(0) on their surfaces. This growth halts the coalescence process, since the larger decahedral particles exhibit lower collision frequencies and surface energies at the given reaction temperature [28, 29]. Both particle populations continue to grow in size due to heterogeneous nucleation until the reaction is terminated.

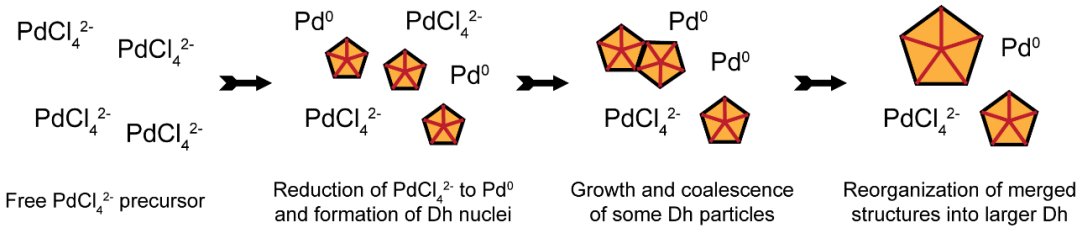

Figure 3.7. Schematic illustration showing the formation of Pd decahedra with two different sizes in the initial stages of a synthesis. The larger decahedra (Dh) are formed through the coalescence of smaller decahedral units, followed by the simultaneous growth of both smaller and larger decahedra. (Reprinted with permission from [32]. Copyright 2016 American Chemical Society.)

As mentioned previously, the nuclei formed during the initial stages of a synthesis are likely decahedral in nature. However, the precise parameters necessary for their formation have not been rigorously studied. Recent work has shown that the morphology of Pd nanocrystals can be controlled by varying the initial reduction rate of a Pd(II) precursor, with the overall reaction modelled as pseudo-first-order [30]. In order to further quantify the nature of the sulfate-mediated synthesis of Pd decahedra, I repeated the kinetic studies by using UV-vis spectroscopy to track the concentration of the remaining Pd(II) precursor over the course of a 2 h reaction. The experiment was conducted for both the standard procedure and a modified procedure that omitted the Na_2SO_4 in order to explore the impact of this component on the reaction kinetics. Unlike the previous study, however, the characteristic absorption peak of $PdCl_4^{2-}$ at 279 nm could not be used due to its overlap with peaks stemming from (PVP) present in the UV spectrographic region. As such, the characteristic peak of the Pd(II) precursor was shifted by quenching the drawn samples in a concentrated solution of NaBr, thereby producing $PdBr_4^{2-}$ with a characteristic absorption peak at 332 nm. The potential presence of Pd clusters and ultra-fine particles is not expected to impact the absorption spectrum since Pd particles of such small sizes are expected to have LSPR features primarily below 300 nm [1, 31]. The reaction was sampled in 5 min intervals for the duration of the study. Figure 3.8A shows the UV-vis spectra collected over the 2 h period for the sulfate-mediated synthesis. As expected from a pseudo-first-order reaction, the absorption at 332 nm declined monotonically over the course of the study. The absorption at the characteristic peak is directly proportional to the concentration of the Pd(II) precursor remaining in solution. Using this information, the rate constant for this reaction could be obtained by plotting the integrated form of the pseudo-first-order reaction rate law, which is written as follows:

$$\ln[\mathrm{A}]_t = -kt + \ln[\mathrm{A}]_0 \qquad (1)$$

where $[A]_0$ and $[A]_t$ represent the concentrations of the Pd(II) precursor at the beginning of a synthesis and at a specific time point, respectively; *k* is the rate constant; and *t* is time.

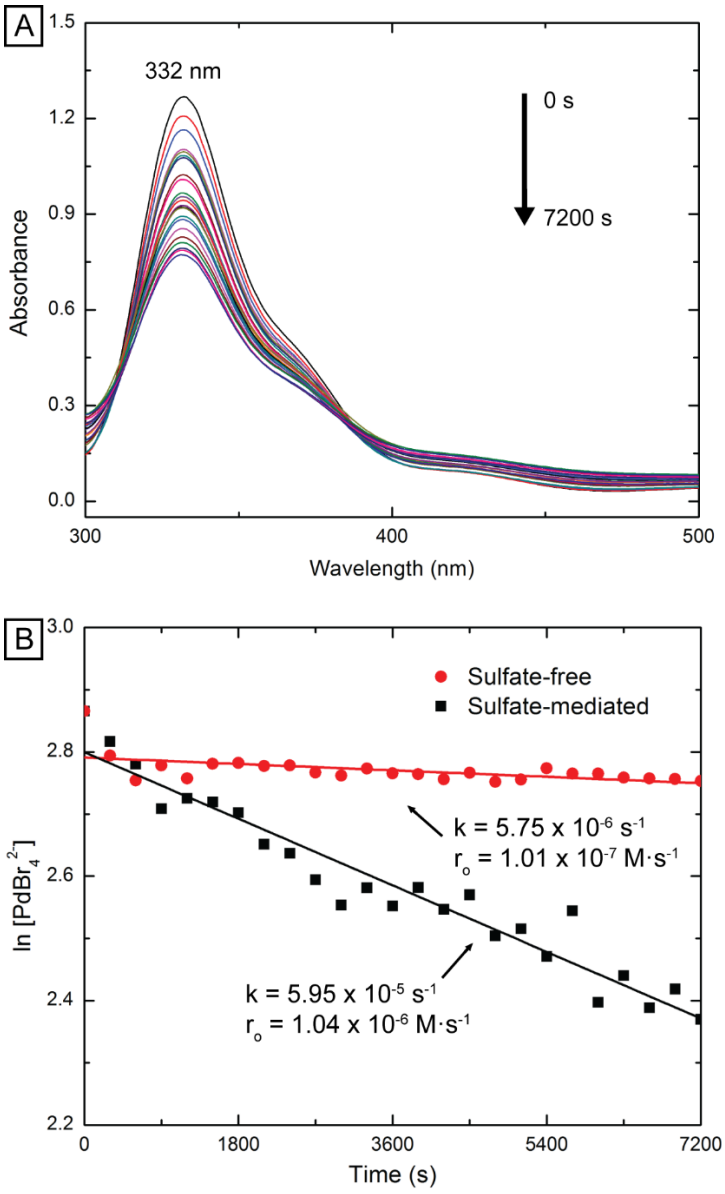

Figure 3.8. Quantitative analysis of the reaction kinetics involved in the standard sulfate-mediated synthesis. (A) UV-vis spectra of the Pd(II) precursor, upon conversion to $PdBr_4^{2-}$, remaining in the reaction solution. The reaction was sampled over a 2 h period in 5 minute intervals. The $PdCl_4^{2-}$ samples were added into a concentrated NaBr solution to quench the reduction and shift the absorption peak to 332 nm. (B) Plot showing the natural log of $PdBr_4^{2-}$ concentration over time for the sulfate-free and sulfate-mediated synthesis. The rate constant (*k*) and initial reduction rate (r_o) are labeled on the fitting curves. (Reprinted with permission from [32]. Copyright 2016 American Chemical Society.)

The derived plots for both the sulfate-mediated and sulfate-free syntheses are shown in Figure 3.8B. The *k* values, derived from the slope of the fitted lines, were 5.95×10^{-5} and 5.75×10^{-6} s^{-1} for sulfate-mediated and sulfate-free reactions, respectively. The order of magnitude difference between the two rate constants supports the previously-stated hypothesis that the sulfate accelerates the reduction kinetics during the synthesis of Pd decahedra [6]. By multiplying the *k* values by the initial concentration of $PdCl_4^{2-}$ (1.76×10^{-2} M), I obtained the initial reduction rates (r_o), which were found to be 1.04×10^{-6} and 1.01×10^{-7} $M \cdot s^{-1}$ for the sulfate-mediated and sulfate-free reactions, respectively.

With the new mechanistic understanding of the Pd decahedra formation, I attempted to improve the efficiency of the overall synthesis. As stated in the above discussion of the product composition, much of the initial Pd is lost in the unreacted precursor during a standard synthesis. A more efficient conversion of precursor to useful product requires an 8-fold longer reaction time, which would make commercial use of this approach unattractive. Since the decahedra grow through heterogeneous nucleation and deposition of Pd(0) atoms, it will be possible to accelerate the conversion of the unreacted precursor by adding a secondary reducing agent after the initial nucleation event. To this end, I introduced varying amounts of AA into the reaction system 35 min after the addition of Na_2PdCl_4. The delay ensured that the increased rate of reduction, corresponding to the presence of AA, did not interfere with the formation of the decahedral nuclei. Figure 3.9A shows the ICP-MS-derived percentages for the various fractions found in the reaction products after the addition of 100, 200, and 300 mg of AA. The standard reaction time of 3 h was used for all of these studies. The results for the synthesis augmented with 100 mg of AA show a 46% decrease in the amount of unreacted Pd precursor remaining in solution, compared to the reaction conducted without the addition of AA. Concurrently, the percentages of both the larger decahedra and the smaller particle fractions increased by 20.4% and 25.6%, respectively.

The significant increase in the latter population can be attributed to secondary

nucleation induced by the AA. As the amount of the added AA increased, the percentage of smaller particles continued to increase while that of the decahedra decreased. At 300 mg AA, the amount of larger decahedra was only 0.9% above the AA-deprived synthesis, due to significant secondary nucleation.

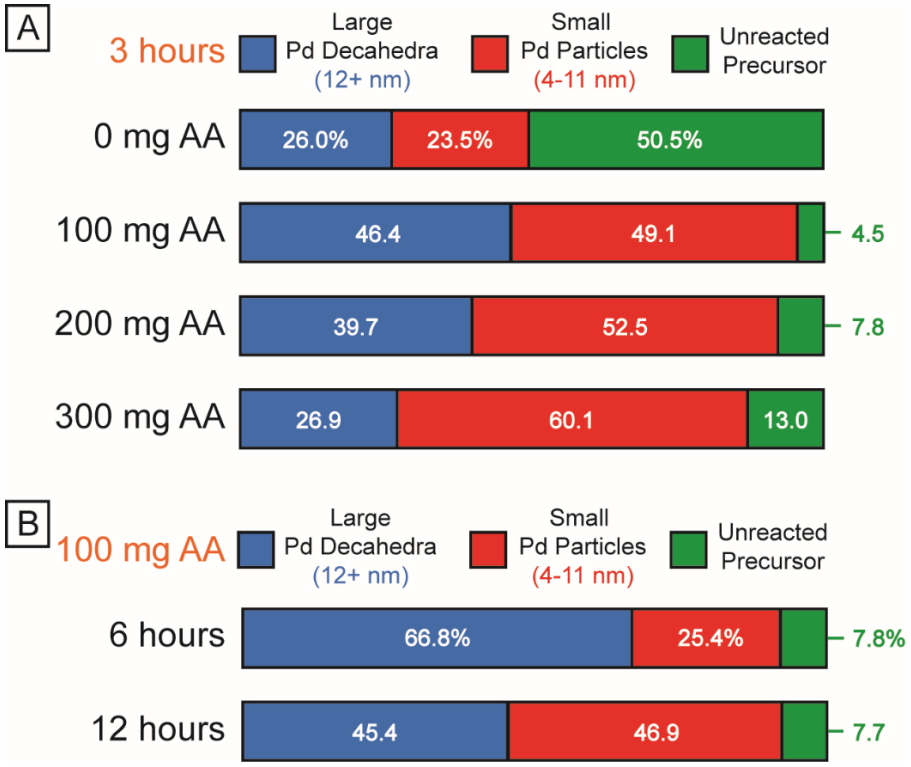

Figure 3.9. (A) ICP-MS-derived Pd contents in the various fractions separated from the products of standard syntheses coupled with the addition of 100, 200, and 300 mg of AA, for 3 h. (B) ICP-MS-derived percentages of Pd found in the various fractions separated from the products of a standard synthesis coupled with the addition of 100 mg of AA after 6 and 12 h of reaction. The larger Pd decahedra were separated from the reaction solution by centrifugation at 16500 RPM for 25 min, while the smaller particles were isolated through centrifugation of the recovered supernatant at 55000 RPM for 90 min. Here the "unreacted precursor" may include the original Na_2PdCl_4 precursor, Pd clusters, and ultrafine Pd particles. (Reprinted with permission from [32]. Copyright 2016 American Chemical Society.)

In order to further improve the conversion efficiency, I paired the addition of AA with an increase in reaction time. Figure 3.9B shows the ICP-MS-derived percentages for the various product fractions recovered after the addition of 100 mg of AA and an increase in reaction time to 6 and 12 h. In the case of the 6 h reaction, the percentage of the larger

decahedra was found to be 66.8%, which is comparable to that of the AA-deprived synthesis after 24 h (69.8%). Moreover, the amount of smaller particles was 23.7% lower and the amount of unreacted precursor was 3.3% higher, when compared to the 3 h synthesis conducted with the addition of 100 mg of AA. This result suggests a synergistic relationship between the increased reduction and oxidative etching at longer reaction time [20]. During this process, the smaller particles were etched away, thereby releasing Pd(II) ions into the solution. These ions were then rapidly reduced by the AA to Pd(0) atoms, which were subsequently deposited onto the surface of the decahedra due to heterogeneous nucleation. Further increasing the reaction time to 12 h resulted in a decrease in the percentage of larger decahedra and an increase in the percentage of the smaller particles. This is likely due to the consumption of the available AA at a longer reaction time and the corresponding weakening of the reduction power relative to that of oxidative etching. Additional studies with different reducing agents, as well as variations in delay and reaction times, should optimize the efficiency of the synthesis further. In order to insure the quality of the Pd decahedra produced with the AA-modified procedure, I separated the larger decahedra and smaller particles using centrifugation and characterized both fractions using TEM. The images of the decahedra are shown in Figure 3.10, highlighting the high product purity and narrow size distribution for all of the various amounts of AA added. The TEM images of the corresponding smaller particles are shown in Figure 3.11, A–C. Interestingly, while these do not appear different from those shown in Figure 3.4C, when these particles were used seeds for the growth of Pd nanorods, the resultant product did not consist primarily of rods [19]. As shown in Figure 3.11, D–F, the sample was instead composed of a mixture of irregular particles and rods. It should be noted that the seeds were washed prior to their use in order to remove any residual AA or its oxidation by-products. This suggests that the secondary nucleation induced by the AA does not produce decahedral particles. As shown in the aforementioned publication, the AA-induced increase in the initial reduction rate during nucleation likely forms particles with icosahedral and single

crystal morphology [30]. However, due to their small size, these undesired particles can be easily removed using centrifugation and thus have little impact on the purity of the final decahedra.

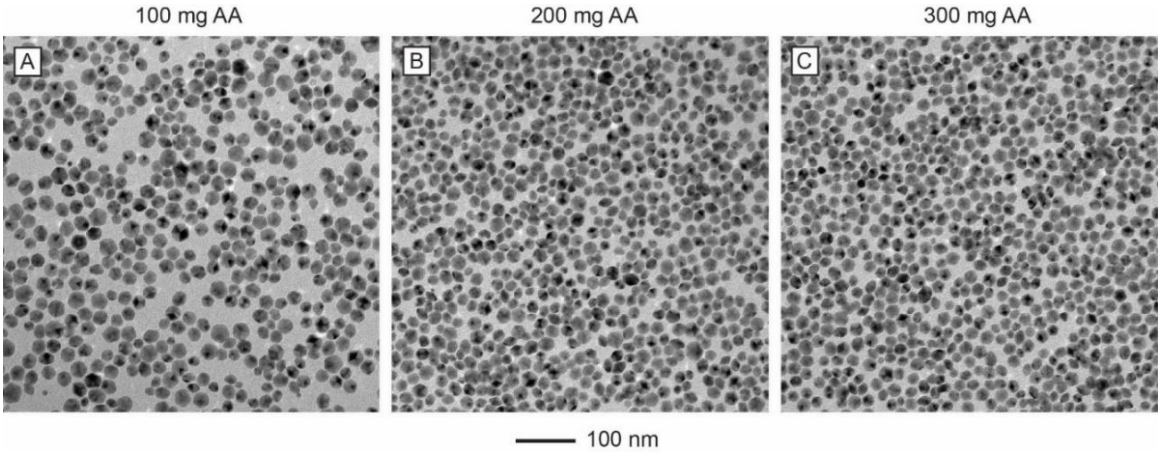

Figure 3.10. TEM images of the decahedra obtained after 3 h into a standard synthesis coupled with different amounts of AA: (A) 100, (B) 200, and (C) 300 mg AA. The decahedral particles were recovered after centrifugation at 16500 RPM for 25 min. (Reprinted with permission from [32]. Copyright 2016 American Chemical Society.)

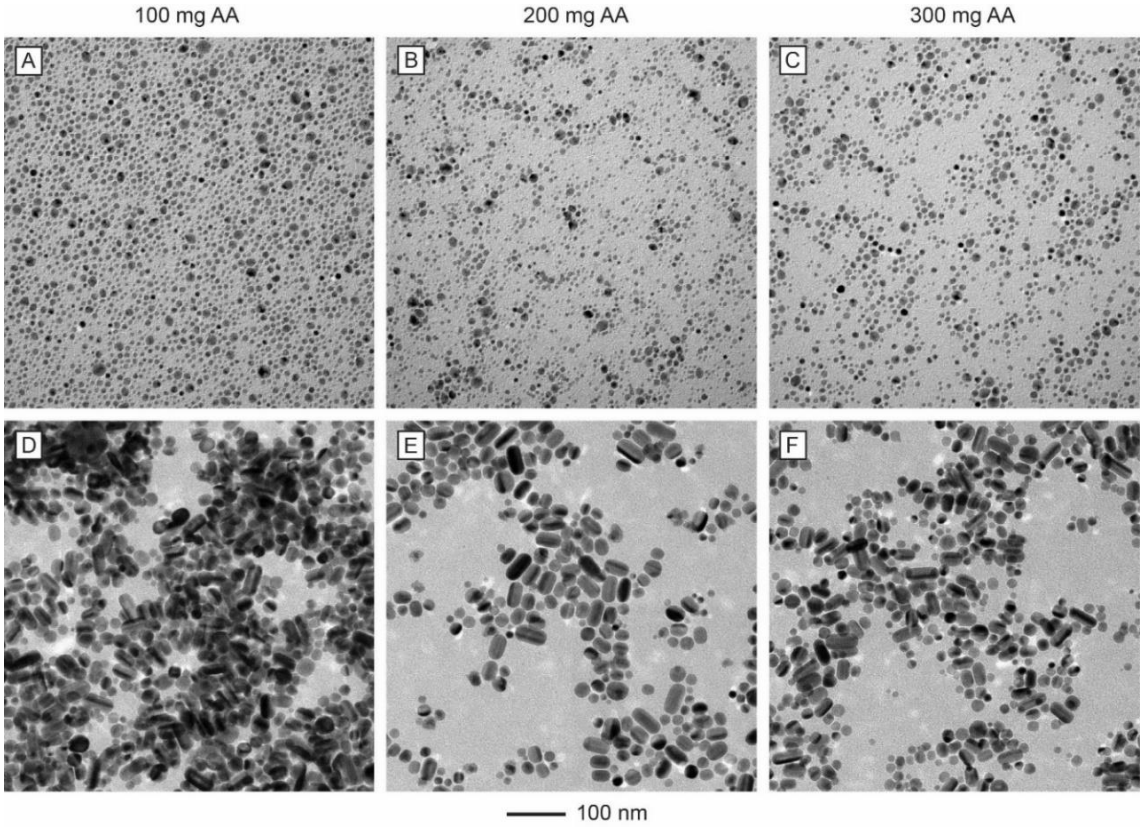

Figure 3.11. TEM images of the smaller particles recovered after 3 h into a standard synthesis coupled with the addition of AA, and the products derived from their use as seeds for the synthesis of Pd nanorods: (A, D) 100, (B, E) 200, and (C, F) 300 mg AA. Panels A-C show the particles recovered after centrifuging the supernatant at 55000 RPM after the larger decahedra have been removed. (Reprinted with permission from [32]. Copyright 2016 American Chemical Society.)

3.3 Conclusion

In summary, I have carried out a systematic, quantitative analysis of the sulfate-mediated polyol synthesis of Pd decahedra. The ICP-MS characterization of the various product fractions revealed that only 26% of the initial Pd precursor was converted into the collected decahedra, with the rest lost as the discarded smaller particles and unreacted precursor. TEM analysis of the products sampled at different reaction times suggested that the size distribution was likely due to the coalescence of some of the initially formed nuclei during the first few minutes of a synthesis. This data, combined with that gathered from a kinetic study, allowed me to propose a mechanism to account for the formation of Pd

decahedra. Drawing on these mechanistic insights, I was able to increase the yield of the collected decahedra to 67% by introducing AA as a second reducing agent meant to rapidly consume the unreacted precursor, thus growing the smaller Pd particles into the desired decahedra.

3.4 Experimental Section

Chemicals and Materials. Diethylene glycol (DEG, ≥99.0%, Lot# BCBP6902V), poly(vinyl pyrrolidone) (PVP, MW≈55000), sodium sulfate (Na_2SO_4, ≥99.0%), L-ascorbic acid (AA, ≥99.0%), sodium bromide (NaBr, ≥99.0%), and sodium iodide (NaI, ≥99.5%) were all procured from Sigma-Aldrich. Sodium tetrachloropalladate(II) (Na_2PdCl_4, ≥99.0%) was obtained from Acros Organics. All chemicals were used as received. Deionized (DI) water with a resistivity of 18.2 MΩ·cm was used throughout the experiments.

Synthesis of Pd Decahedra. In a standard synthesis, 174 mg of Na_2SO_4 was added to a 50 mL three-neck flask equipped with a 6 × 25 mm polygonal, Teflon-coated stirring bar. Next, 8 mL of DEG-based PVP solution (20 mg/mL) was added. The flask was then stoppered and placed in an oil bath heated to 117.5 °C, with stirring speed set to 450 RPM. Note that at this oil temperature, the solution temperature was measured to be 103.3 °C. As soon as the stirring began in the flask, 4 mL of a DEG-based solution of Na_2PdCl_4 (15.5 mg/mL) was introduced and the reaction timer started. The reaction was quenched by immersing the flask in an ice bath. The product was collected by adding acetone in a 3:1 ratio to the reaction solution and centrifuging at 6000 RPM for 10 min. The supernatant and precipitate were separated and the supernatant, containing the majority of the unreacted Na_2PdCl_4 precursor, was saved for analysis. The precipitate was re-dispersed in DI water and centrifuged three times at 16500 RPM for 25 min, with the supernatant gathered after each centrifugation. The collected solid contained the Pd decahedra >12 nm in size. The stored aqueous supernatant was centrifuged at 55000 RPM for 90 min to separate the Pd

particles of 4-11 nm in size from the remaining unreacted Na_2PdCl_4 precursor. The solutions containing the unreacted precursor, >12 nm decahedra, and 4-11 nm particles were analyzed separately by ICP-MS to determine Pd concentration. The mass of Pd present in each component was obtained when the obtained concentration was multiplied by the volume of the corresponding solution. The sum of Pd masses for all components was used as the basis for determining the percentage of each component within the initial product mixture. The Pd concentration, and thus the mass, in the initial Na_2PdCl_4 solution was measured separately in order to insure that there was no significant loss of Pd during the separation and washing steps.

Synthesis of Five-fold Twinned Pd Nanorods. In a standard procedure, 7 mL of DEG containing 105 mg of PVP, 100 mg of AA, and 100 mg of NaI was added to a 20 mL vial equipped with a 10 x 15 mm polygonal, Teflon-coated stirring bar. The vial was then capped and placed in an oil bath held at 160 °C under magnetic stirring (450 RPM). After 10 min, 1 mL of Pd decahedral seeds in DEG was added, immediately followed by 3 mL of a DEG solution of Na_2PdCl_4 (10 mg/mL). The reaction was allowed to proceed for 1 h and was terminated by immersing the vial in an ice-water bath. The product was collected by adding acetone in a 3:1 ratio to the reaction solution and centrifuging at 6000 RPM for 10 min. The collected precipitate was re-dispersed in DI water and centrifuged three times at 16500 RPM for 25 min.

Kinetic Studies of the Pd Decahedral Synthesis. During a standard Pd decahedra synthesis, 100 μL aliquots were drawn with a micropipette in 5 min intervals for 2 h, with the first aliquot drawn immediately after the injection of the Na_2PdCl_4 precursor. The aliquots were thoroughly mixed into 1.4 mL of ice-cold aqueous NaBr solution (200 mg/mL). Immediately afterwards, 100 μL of the quenched solution was injected into 0.9 mL of aqueous NaBr (200 mg/mL) inside a cuvette and the sample was characterized with UV-vis spectroscopy.

Instrumentation. TEM images were obtained using a Hitachi HT7700 microscope

operated at 120 kV. High-resolution TEM (HRTEM) and high-angle annular dark-field scanning transmission electron microscopy (HAADF-STEM) images were collected with a Hitachi HD2700 operated at 200 kV. ICP-MS data was obtained with a NexION 300Q (PerkinElmer). UV-vis absorption spectra were recorded with a Lambda 750 spectrometer (PerkinElmer). An Eppendorf centrifuge (5430) and an Optima MAX-XP Ultracentrifuge (Beckman Coulter) were used for the centrifugation and washing of all samples.

3.5 Notes to Chapter 3

Part of this chapter is adapted from the paper "Toward a Quantitative Understanding of the Sulfate-mediated Synthesis of Pd Decahedral Nanocrystals with High Conversion and Morphology Yields" published in the *Chemistry of Materials* [32].

3.6 References

[1] Li, C.; Sato, R.; Kanehara, M.; Zeng, H.; Bando, Y.; Teranishi, T. *Angew. Chem., Int. Ed.* **2009**, *48*, 6883–6887.

[2] Fu, G.; Jiang, X.; Tao, L.; Chen, Y.; Lin, J.; Zhou, Y.; Tang, Y.; Lu, T. *Langmuir* **2013**, *29*, 4413–4420.

[3] Zhang, Q.; Xie, J.; Yang, J.; Lee, J. Y. *ACS Nano* **2009**, *3*, 139–148.

[4] Wang, H.; Niu, G.; Zhou, M.; Wang, X.; Park, J.; Bao, S.; Chi, M.; Cai, Z.; Xia, Y. *ChemCatChem* **2016**, *8*, 1658–1664.

[5] Lim, B.; Xiong, Y.; Xia, Y. *Angew. Chem., Int. Ed.* **2007**, *46*, 9279–9282.

[6] Niu, Z.; Peng, Q.; Gong, M.; Rong, H.; Li, Y. *Angew. Chem., Int., Ed.* **2011**, *50*, 6315–6319.

[7] Huang, H.; Wang, Y.; Ruditskiy, A.; Peng, H.-C.; Zhao, X.; Zhang, L.; Liu, J.; Ye, Z.; Xia, Y. *ACS Nano* **2014**, *8*, 7041–7050.

[8] Choi, S.-I.; Herron, J. A.; Scaranto, J.; Huang, H.; Wang, Y.; Xia, X.; Lv, T.; Park,

J.; Peng, H.-C.; Mavrikakis, M.; Xia, Y. *ChemCatChem* **2015**, *7*, 2077–2084.

[9] Huang, H.; Bao, S.; Chen, Q.; Yang, Y.; Jiang, Z.; Kuang, Q.; Wu, X.; Xie, Z.; Zheng, L. *Nano Res.* **2015**, *8*, 2698–2705.

[10] Xue, W.; Choi, S.-I.; Roling, L. T.; Luo, M.; Ma, C.; Zhang, L.; Chi, M.; Liu, J.; Xie. J.; Herron, J. A.; Mavrikakis, M.; Xia, Y. *Nature Commun.* **2015**, *6*, 7594.

[11] Lv, T.; Yang, X.; Zheng, Y.; Huang, H.; Zheng, L.; Tao, J.; Pan, L.; Xia, Y. *J. Phys. Chem. C* **2016**, *120*, 20768–20774.

[12] Bian, T.; Zhang, H.; Jiang, Y.; Jin, C.; Wu, J.; Yang, H.; Yang, D. *Nano Lett.* **2015**, *15*, 7808–7815.

[13] Hobbs, K.; Cathcart, N.; Kitaev, V. *Chem. Commun.* **2016**, *52*, 9785–9788.

[14] Wang, X.; Vara, M.; Luo, M.; Huang, H.; Ruditskiy, A.; Park, J.; Bao, S.; Liu, J.; Howe, J.; Chi, M.; Xie, Z.; Xia, Y. *J. Am. Chem. Soc.* **2015**, *137*, 15036–15042.

[15] He, D. S.; He, D.; Wang, J.; Lin, Y.; Yin, P.; Hong, X.; Wu, Y.; Li, Y. *J. Am. Chem. Soc.* **2016**, *138*, 1494–1497.

[16] McEachran, M.; Keogh, D.; Pietrobon, B.; Cathcart, N.; Gourevich, I.; Coombs, N.; Kitaev, V. *J. Am. Chem. Soc.* **2011**, *133*, 8066–8069.

[17] Luo, M.; Huang, H.; Choi, S.-I.; Zhang, C.; Silva, R. R.; Peng, H.-C.; Li, Z.-Y.; Liu, J.; He, Z.; Xia, Y *ACS Nano* **2015**, *9*, 10523–10532.

[18] Luo, M.; Ruditskiy, A.; Peng, H.-C.; Tao, J.; Figueroa-Cosme, L.; He, Z.; Xia, Y. *Adv. Funct. Mater.* **2016**, *26*, 1209–1216.

[19] Huang, H.; Zhang, L.; Lv, T.; Ruditskiy, A.; Liu, J.; Ye, Z.; Xia, Y. *ChemNanoMat* **2015**, *1*, 246–252.

[20] Zheng, Y.; Zeng, Y.; Ruditskiy, A.; Liu, M.; Xia, Y. *Chem. Mater.* **2014**, *26*, 22–33.

[21] Xia, X.; Choi, S.-I.; Herron, J. A.; Lu, N.; Scaranto, J.; Peng, H.-C.; Wang, J.; Mavrikakis, M.; Kim, M. J.; Xia, Y. *J. Am. Chem. Soc.* **2013**, *135*, 15706−15709.

[22] Keunen, R.; Cathcart, N.; Kitaev, V. *Nanoscale* **2014**, *6*, 8045−8051.

[23] Baletto, F.; Ferrando, R. *Rev. Mod. Phys.* **2005**, *77*, 371–423.

[24] Barnard, A. S.; Young, N. P.; Kirkland, A. I.; van Huis, M. A.; Xu, H. *ACS Nano* **2009**, *3*, 1431–1436.

[25] Lan, Y.-K.; Su, C.-H.; Sun, W.-H.; Su, A.-C. *RSC Adv.* **2014**, *4*, 13768–13773.

[26] Lim, T. H.; McCathy, D.; Hendy, S. C.; Stevens, K. J.; Brown, S. A.; Tilley, R. D. *ACS Nano* **2009**, *3*, 3809–3813.

[27] Bisson, L.; Boissiere, C.; Nicole, L.; Grosso, D.; Jolivet, J. P.; Thomazeau, C.; Uzio, D.; Berhault, G.; Sanchez, C. *Chem. Mater.* **2009**, *21*, 2668–2678.

[28] Wang, F.; Richards, V. N.; Shields, S. P.; Buhro, W. E. *Chem. Mater.* **2014**, *26*, 5–21.

[29] Li, D.; Nielsen, M. H.; Lee, J. R. I.; Frandsen, C.; Banfield, J. F.; De Yoreo, J. J. *Science* **2012**, *336*, 1014–1018.

[30] Wang, Y.; Peng, H.-C.; Liu, J.; Huang, C. Z.; Xia, Y. *Nano Lett.* **2015**, *15*, 1445–1450.

[31] Wang, Q.; Wang, Y.; Guo, P.; Li, Q.; Ding, R.; Wang, B.; Li, H.; Liu, J.; Zhao, X. S. *Langmuir* **2014**, *30*, 440–446.

[32] Ruditskiy, A.; Zhao, M.; Gilroy, K. D.; Vara, M.; Xia, Y. *Chem. Mater.* **2016**, *28*, 8800–8806.

CHAPTER 4

OXIDATIVE ETCHING OF PALLADIUM DECAHEDRAL NANOCRYSTALS WITH A PENTA-TWINNED STRUCTURE AND ITS IMPACT ON THEIR GROWTH BEHAVIOR

4.1 Introduction

Oxidative etching is a commonly occurring electrochemical process, which is exemplified by the formation of iron rust in the presence of water and air. When applied to metallic nanocrystals, the power of this process can be harnessed to manipulate the properties of nanocrystals, including their size, shape, internal structure, and composition [1, 2]. This is typically achieved by employing an etchant pair, such as O_2/halide, to systematically remove atoms from a nanocrystal. Over the past decade or so, this approach has resulted in metal nanocrystals with a diverse array of morphologies, including octapods [3, 4], nanocages [5−8], and nanoframes [9−11]. The preferential etching of multi-twinned products has facilitated the preparation of single-crystal and single-twinned Ag nanocrystals with high purity [12, 13]. Moreover, the coupling of oxidative etching with reduction-based regrowth has allowed for the creation of a variety of structures from a single type of Pd nanocrystals [14]. A related approach has also been used to create Ag-Au alloyed nanostructures with hollow interiors, which would be otherwise difficult to fabricate [15].

Since metal nanocrystals are typically synthesized in an oxygenated environment, and often from halide-based precursors, oxidative etching is inevitable. As such, it would be sensible to systematically explore its impacts on the physical properties of metal nanocrystals. Alivisatos *et al.* used *in situ* transmission electron microscopy (TEM) to investigate the oxidative etching of various Au nanocrystals inside a graphene pocket [16]. Notably, the authors observed a non-equilibrium intermediate during the etching of a Au

nanocube, before the intermediate was converted to the expected spherical shape. In principle, one would expect to glean more information when moving from single-crystal nanocubes to nanocrystals with more complex internal twin structures. To this end, Pd decahedral nanocrystals would provide a rich platform for the study of oxidative etching due to the presence of a diversified set of surface features [8, 17]. These include the presence of twin boundaries, different types of facets, and multiple subtypes of edges and vertices. Such a wide variety of surface features potentially allows for the identification of sites most prone to oxidative etching, as well as a systematic study of etching in terms of initiation and propagation. Furthermore, Pd decahedra have shown potential as electrocatalysts [18], as well as a platform material for the creation of more complex structures, such as core-shell nanocrystals [7] and pentagonal nanorods [19−21], with notable catalytic and optical properties. Taken together, it can be concluded that understanding the effects of oxidative etching on decahedral nanocrystals is critical to their effective use in real-world applications.

In this Chapter, I report a systematic study of oxidative etching of Pd decahedra by the O_2/I^- etchant pair. This pair was chosen owing to its ability to effectively etch Pd nanocrystals at a controllable rate [14], allowing me to analyze the etching process over a reasonable timeframe. The etched samples were characterized using TEM, high-resolution TEM (HRTEM), and high-angle annular dark-field scanning transmission electron microscopy (HAADF-STEM) to ascertain the initiation and propagation of etching over time. The effects of the etching environment were also explored by conducting experiments in diethylene glycol (DEG) and deionized (DI) water, in conjunction with the introduction of various types of additives. Finally, I demonstrated the use of oxidative etching to modulate the growth behavior of Pd decahedral seeds and thus generate nanocrystals with more complex structures.

4.2 Results and Discussion

Figure 4.1 shows the effects of O_2/I^--based oxidative etching on Pd decahedral nanocrystals. Figure 4.1A shows a TEM image of the initial Pd decahedra used for the etching studies, which had an average size of ~17 nm, defined as the distance (*d*) between two vertices of a decahedron (see Figure 4.2). For clarity, I will henceforth refer to the five in-plane vertices as "equatorial" and the two remaining vertices as "axial". The red arrow in Figure 4.1A denotes an example of a decahedral nanocrystal imaged from the side. Figure 4.1B shows the HAADF-STEM image of an initial decahedron, highlighting the flat edges running along the equator of the structure, as well as the slight truncation at the equatorial vertices. Exposing the decahedra to O_2/I^- in DEG for 30 min at 90 °C yielded particles with a notably rounded profile, compared to the initially well-defined decahedra, as shown in Figures 4.1C and D. Moreover, the rounded particles that were imaged from the side (for example, denoted by the red arrow in Figure 4.1C) showed evidence of noticeable rounding at the axial vertices as well. Crucially, the penta-twinned structure of the starting nanocrystals was clearly preserved. After the etching, the average size of the rounded particles decreased by 2–3 nm, although the size polydispersity of the initial decahedra made an accurate comparison difficult.

Interestingly, increasing the reaction time and/or the temperature did not produce a noticeable difference in particle size or structure. As shown in Figures 4.3A and B, maintaining the temperature at 90 °C and increasing the reaction time to 60 and 90 min, respectively, resulted in rounded particles with sizes of 15 nm. Similar products were obtained after increasing the reaction temperature to 120 °C and subjecting the decahedra to etching for 60 and 90 min, as shown in Figures 4.3C and D, respectively. These results suggest that the rate of etching was slowed down significantly once the initial rounding of the decahedra was complete.

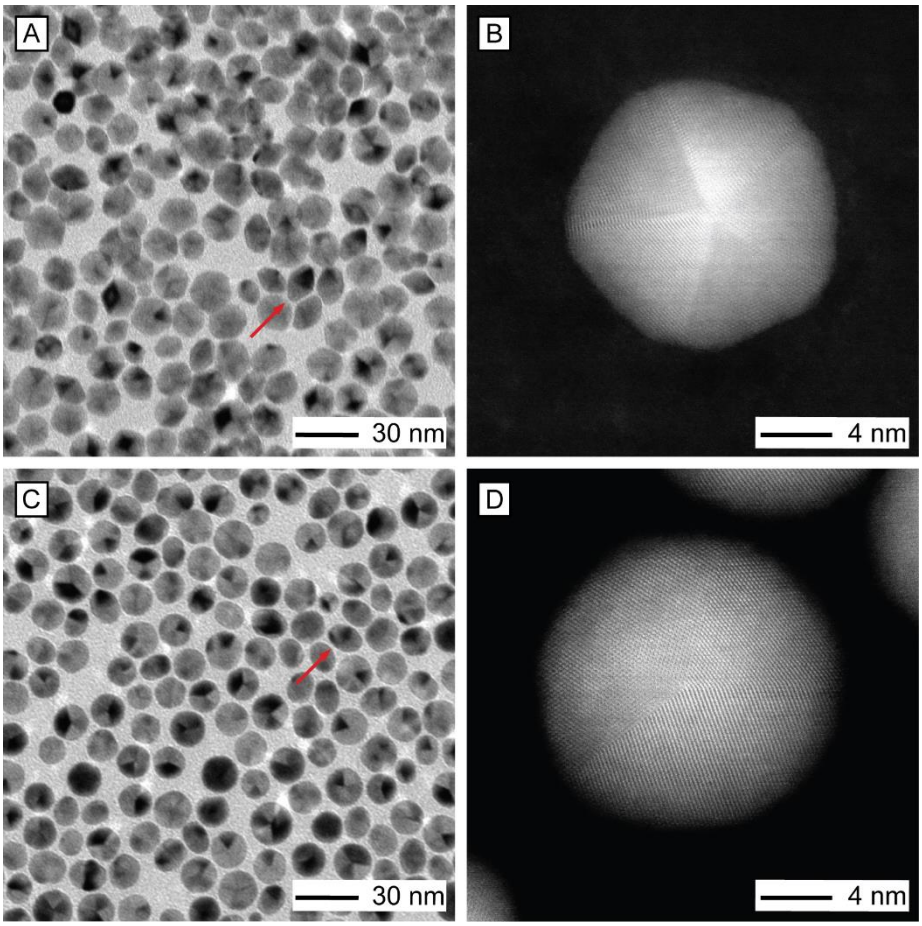

Figure 4.1. TEM and HAADF-STEM images of Pd decahedral nanocrystals (A, B) before and (C, D) after oxidative etching with O_2/I^- in DEG at 90 °C for 30 min. The etched nanocrystals show a significantly rounded profile, while retaining the penta-twinned structure. The red arrows denote examples of initial decahedra (A) and rounded particles (C) imaged from the side.

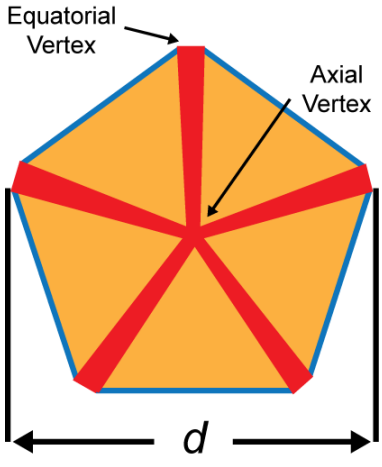

Figure 4.2. Definition of size (*d*) of a multi-twinned decahedral nanocrystal.

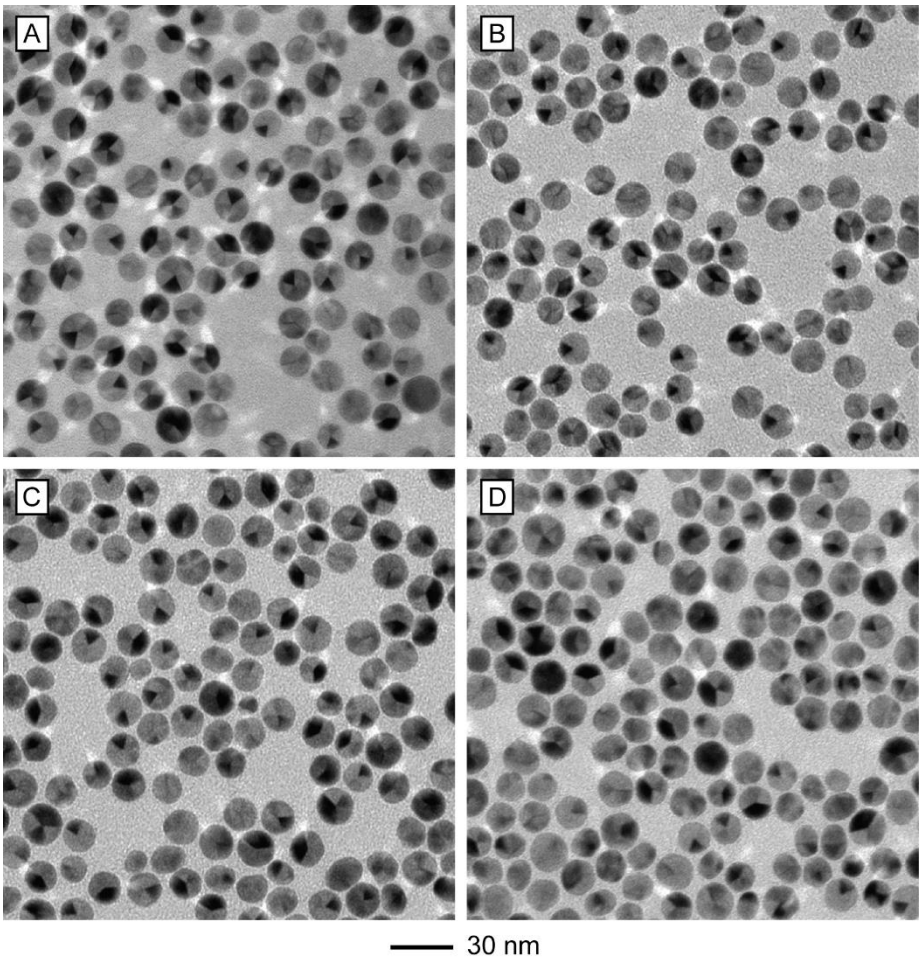

Figure 4.3. TEM images showing the effects of increasing temperature and reaction time on the etching of Pd decahedral nanocrystals. (A) 90 °C, 60 min, (B) 90 °C, 90 min, (C) 120 °C, 60 min, and (D) 120 °C, 90 min. All the etching experiments were conducted in DEG.

In order to gain a better understanding of the morphology of the rounded particles, further characterization was performed using TEM, HRTEM, and HAADF-STEM, as shown in Figure 4.4. TEM imaging (Figure 4.4A) revealed significant rounding at the equatorial vertices of the initial decahedra. Furthermore, new vertices could be clearly observed midway between the twinned boundaries, though not all of the particles showed this feature. The magnitude of the rounding can be clearly seen in the HAADF-STEM image (Figure 4.4B). The red lines represent the outlines of a regular decahedron with truncated equatorial vertices, aligned to the twin boundaries of the imaged particle. The

extent of truncation in the outline was estimated using measurements taken from Figure 4.1B. These images indicate that the etching process preferentially removed Pd atoms from the equatorial vertices and the adjacent, equatorial edges. A closer look at the equator of the rounded particles (Figures 4.4C and D) showed a smooth atomic edge with hexagonal packing, as well as evidence of a new vertex denoted by white lines in Figure 4.4D. Electron microscopy images without the overlays can be found in Figure 4.5.

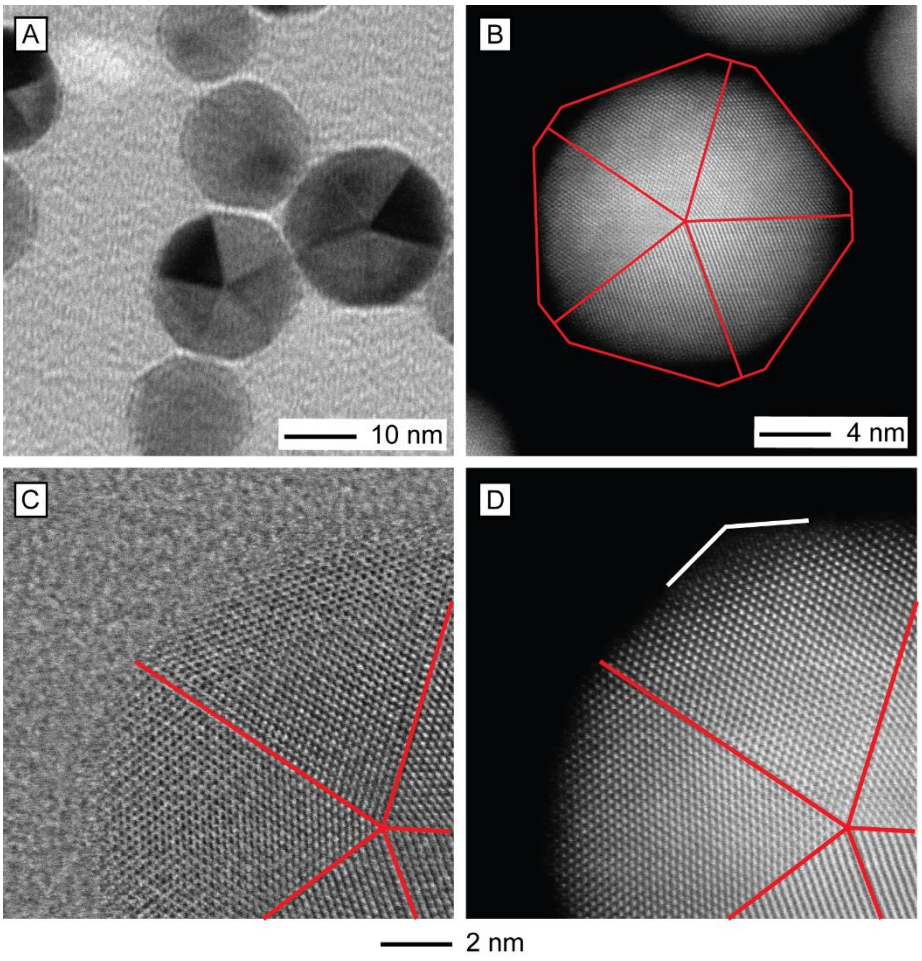

Figure 4.4. (A) Higher-resolution TEM and (B) HAADF-STEM images of rounded Pd decahedral nanocrystals. (C, D) Magnified HRTEM and HAADF-STEM images taken from the equatorial edge regions of the rounded Pd decahedron shown in (B). The red lines denote the outlines and twin boundaries of the decahedron. The extent of truncation in the outline was estimated by benchmarking to the image shown in Figure 4.1B. The white lines in (D) highlight the formation of a new vertex. A version of this Figure without the outlines can be found in Figure 4.5.

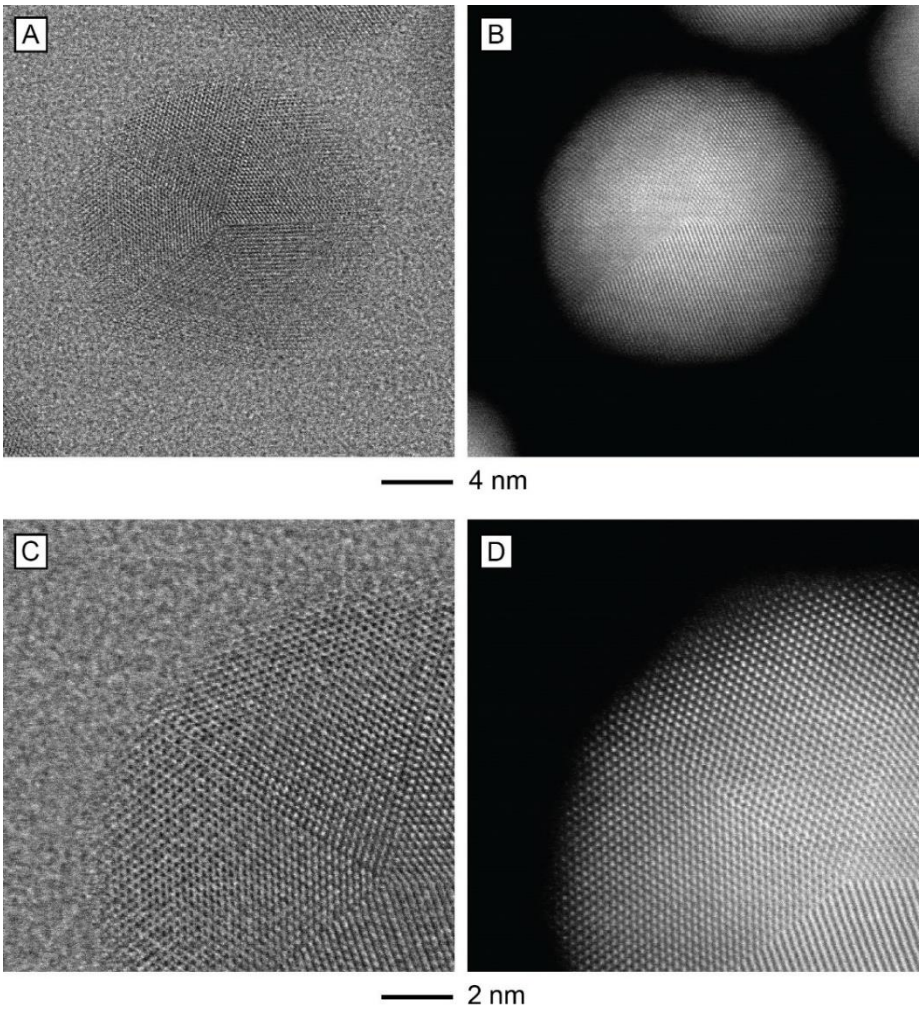

Figure 4.5. Version of Figure 4.4 without the red outlines. (A) HRTEM and (B) HAADF-STEM images of a rounded Pd decahedron. Magnified HRTEM and HAADF-STEM images taken from the equatorial edge of the rounded Pd decahedron are shown in (C) and (D), respectively.

The oxidative etching process utilized in this study can be summarized as an electrochemical reaction between the Pd^0 atoms on the particle surface and the O_2 gas molecules dissolved in the DEG, with the I^- anions serving as coordination ligands and charge carriers [1]. More specifically, the O_2 gas is reduced to oxide species, while the Pd^0 is consequently oxidized to Pd^{2+}. The metal cations are then rapidly complexed with I^- to form the highly stable PdI_4^{2-} [22]. This species is difficult to reduce back into Pd^0, thus reducing the concentration of free Pd^{2+} and driving the etching reaction forward. In general, the susceptibility of specific nanocrystal surface sites to oxidative etching depends on their

respective surface free energies, with higher energy sites being more prone to dissolution. In turn, the free energy of an atom is determined by the number of bonds connecting that atom with its nearest neighbors, as well as the extent of lattice strain those bonds experience. The former is known as the coordination number (CN), with the free energy of an atom increasing as the CN decreases. Lattice strain can be described as the expansive or compressive distortion in bond length, relative to the ideal bulk value, which results in higher free energies for the atoms involved [23]. This phenomenon is typically caused by tensions at the interface between two different phases within a crystal, such as those found at the boundaries between different facets or twin defect planes.

By combining these basic principles with the TEM observations of the etched Pd decahedra, I can posit a mechanism to account for the etching. A schematic illustration is shown in Figure 4.6. For a truncated regular decahedron, the atoms with the lowest CN are located at the equatorial (CN = 4) and axial (CN = 5) vertices, followed by those found at the {100} edges (CN = 6) [17]. Additionally, the {211}-enclosed twinned ridges separating the {111} facets experience increasing expansive strain with increasing radial distance from the decahedral center [8]. The combination of these two factors suggests that the etching process should begin at the equatorial vertices, likely forming re-entrant grooves at these sites. These features have been previously observed at the equatorial vertices of Pd@Pt core-shell concave decahedra, explained as a result of internal restructuring needed to relax lattice strain [8]. Limitations of TEM imaging make it difficult to ascertain whether re-entrant grooves were also formed at the axial vertices. However, the rounding of the axial vertices seen in Figure 4.1C suggests that these sites are likewise susceptible to dissolution by the O_2/I^- etchant. The Pd atoms present in the twinned ridges likely resist dissolution, despite their strain-induced high free energy, due to comparatively higher CN values (CN = 7-8), thus preserving the penta-twinned structure. The removal of Pd atoms during the formation of the re-entrant grooves at the equatorial vertices reduces the CN values for the adjacent edge atoms, making them highly susceptible to dissolution. As such,

the etching proceeds symmetrically away from the re-entrant grooves along the equatorial edges until the new vertices form midway between the twinned ridges. Finally, these low CN features are dissolved, thereby producing a fully rounded structure with similar CN values along the entire equatorial edge. This homogeneity may explain the apparent slowdown in the etching rate observed after the formation of the rounded particles.

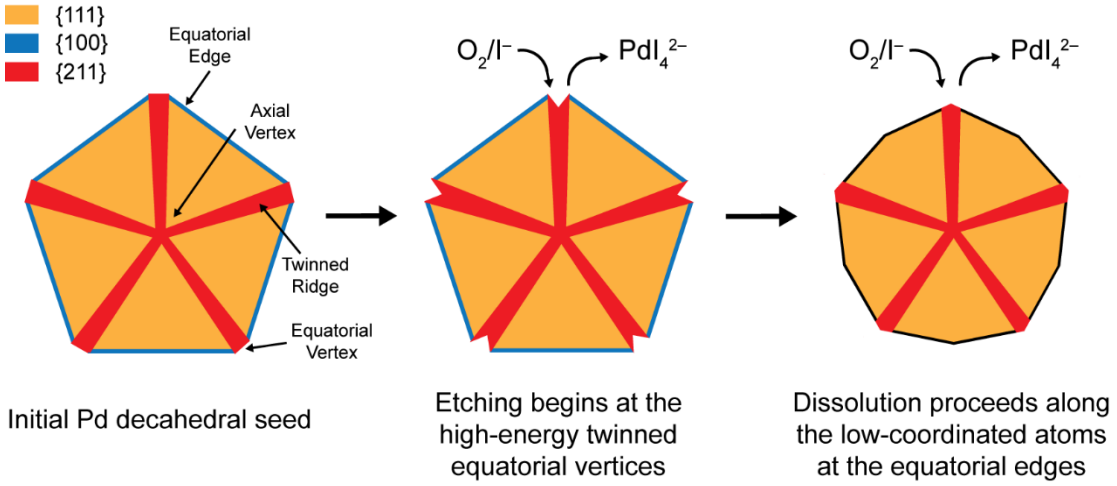

Figure 4.6. Schematic illustration of the etching process, which begins with the formation of re-entrant grooves at the equatorial vertices of a decahedron. The dissolution then proceeds by removing the low-coordination atoms along the equatorial edges of the particle until a rounded particle is formed.

Since the DEG possesses inherent reducing capability, it would be prudent to study the etching process in a more inert medium. To that end, the standard procedure was modified to use DI water as the solvent, instead of DEG. These experiments were performed with the same batch and concentration of the initial Pd decahedral nanocrystals, as well as the same batches of all chemicals involved. Both reactions were conducted at 90 °C for 30 min. While the etching of decahedra performed in DEG produced the expected rounded particles (Figure 4.1C), etching in an aqueous environment resulted in particles with well-preserved decahedral features (Figure 4.7A). This result is counterintuitive, since the reducing capability of DEG is expected to counteract the etching process. Thus, the products collected from the water-based reaction were expected to show evidence of more

extensive dissolution, when compared to the decahedra etched in DEG. There exist several potential reasons that may explain the disparate etching behaviors in DEG and water. Firstly, there exists a difference in O_2 gas solubility between the two solvents. Since the rate of the etching reaction depends on the concentration of the dissolved O_2 gas, a low solubility of O_2 in a solvent may result in depressed rates of etching, and *vice versa*. While there is a lack of data on the solubility of O_2 in DEG, I can attempt to approximate it by comparing the Ostwald coefficients for water and ethylene glycol (EG), a similar molecule also used as a reducing solvent. The Ostwald coefficient is defined as the ratio between the volume of dissolved gas and the volume of the solvent. At 25 °C, the Ostwald coefficient of O_2 in water (0.0347) is found to be approximately 14.5% higher than that of EG (0.0303) [24]. Since gas solubility decreases with increasing temperature, the O_2 solubility is expected to decrease substantially in both solvents at 90 °C. As such, the higher O_2 solubility in water, compared to EG, suggests that the difference in O_2 gas concentration cannot explain the unusual etching behavior. A second possible explanation lies in the other half of the etchant pair: the ion. DEG is known to contain trace impurities, present as byproducts of the chemical manufacturing and storage processes. According to the manufacturer's assay of the specific DEG batch used for these experiments, there was a measurable concentration of Cl^- (~2 mg/kg) and Fe^{3+} (~2 mg/kg) dissolved in the solvent. Both of these ions are known as strong etchants and would be absent in the filtered DI water (with a resistivity of 18.2 MΩ·cm) [1]. To test the impact of these impurities, equivalent concentrations of the ions in question were added to the DI water, in addition to the standard amount of I^-, by using NaCl and $FeCl_3$, respectively. Figures 5.7B and C show the results of the corresponding etching studies. In both cases, the pentagonal shape of the initial decahedra was still preserved, indicating that the impurities were not responsible for the observed differences in the etching products between DEG and water.

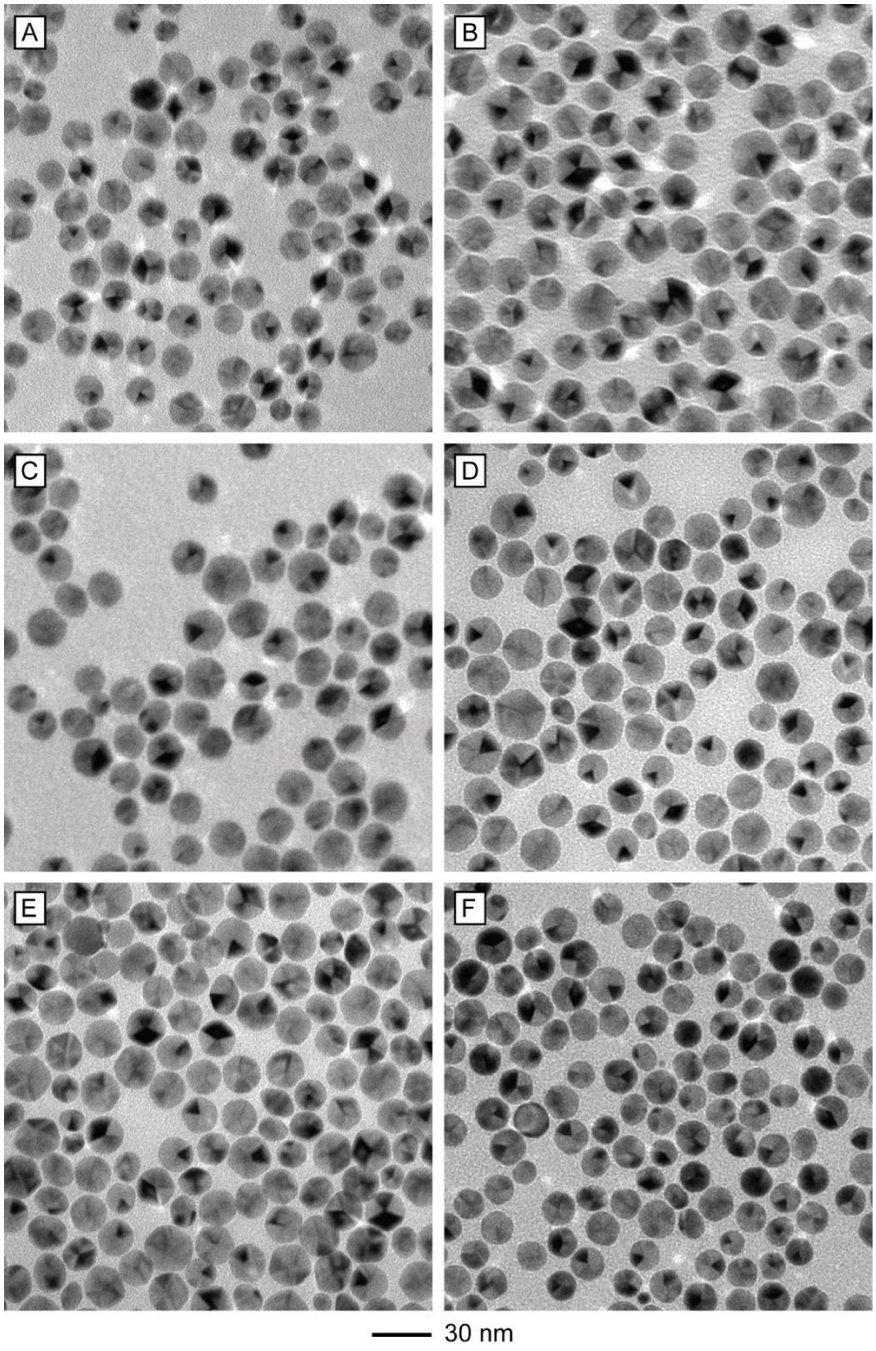

Figure 4.7. TEM images of Pd decahedral nanocrystals obtained by oxidative etching with O_2/I^- in DI water. (A) Replacement of DEG with DI water in the standard procedure. (B, C) Addition of 2 mg/mL of Cl^- and Fe^{3+} to the water-based etching solution, respectively. (D-F) Addition of 60, 100, and 300 mg of AA to the water-based etching solution, respectively. All experiments were conducted at 90 °C for 30 min, using the same batch of Pd decahedra at the same concentration.

Since the reducing capability of DEG is one of the primary differences between the two solvents, it would be sensible to explore its impact on the etching process. To that end, I introduced varying amounts of ascorbic acid (AA), a reducing agent, into the water-based etching solution. The experiments were conducted at 90 °C for 30 min. It should be noted that the reducing strength of a glycol increases with continued application of heat while in air, due to the oxidation of the glycol molecules into aldehyde derivatives [25]. For 60 mg of AA added, the collected products largely consisted of decahedra, as shown in Figures 4D. Addition of 100 mg of AA (Figure 4.7E), resulted in a mixture of decahedra and rounded particles. However, when the amount of AA was increased to 300 mg (Figure 4.7F), the products were largely comprised of rounded particles with distinct penta-twinned structures. These particles appear identical to those produced with DEG as the solvent, such as those shown in Figure 4.1C. These results suggest that a sufficiently reducing environment is crucial to the oxidative etching process. An explanation for this counterintuitive phenomenon may lie in the methods used for the cleaning and storage of the initial Pd decahedral nanocrystals. The decahedra were prepared, cleaned, and stored under exposure to air [26]. Furthermore, DI water was used to both purify and store the final nanocrystals. Exposure to such oxidative environments likely caused an oxide PdO layer to form on the particle surfaces [27]. As with bulk scale oxidative etching, an oxide surface layer can inhibit further oxidation of a structure. Based on this principle I hypothesize that a sufficiently strong reducing environment is necessary to remove the oxide layer, thereby making the nanocrystal susceptible to oxidative etching. This result has implications for general metal nanocrystal synthesis and storage, since it is commonly accepted that a reducing environment is favorable to preventing nanocrystal degradation over time. Instead, it may be more sensible to expose the newly prepared nanocrystals to a mildly oxidative environment in order to form an oxide shell and protect against further metal dissolution.

Finally, it would be interesting to explore the utility of the rounded particles as

platforms for the seeded growth of more complex structures. To achieve this, a recently developed seed-mediated synthesis of Pd pentagonal nanorods was adapted to use the rounded particles as growth surfaces [21]. Standard nanorods, produced through the seeded growth of the initial decahedra, are shown in Figure 4.8A. These structures are symmetric along their length and terminated by rounded ends. Employing the rounded particles as seeds resulted in the formation of asymmetric, tapered nanorods, with notably smaller diameters at one end of the structure than the other, as shown in Figure 4.8B. The lengths of tapered nanorods were measured to be 22 nm on average, compared with 30 nm for the standard nanorods. HAADF-STEM characterization of the ends (Figure 4.8C) and the sides (Figure 4.8D) of the rods, revealed that the penta-twinned structure was preserved throughout the nanorod after the Pd outgrowth. The sloped sides of the tapered rod were likely enclosed by high index facets, rather than the {100} facets found on the sides of the standard nanorods. Importantly, Figure 4.8C shows that the larger end of the tapered rod contained well-defined decahedral features, which were much sharper than those of the initial Pd decahedra used for the etching studies (Figure 4.1B). This information suggests that overgrowth not only occurred in the axial direction, but also radially along the etched equatorial edges of the rounded particles. Previous seeded growth syntheses of Pd-Ag and Pd-Cu nanorods [19, 20], utilizing Pd decahedra as seeds, showed that the axial growth proceeds from one side of a decahedron, i.e. one set of five {111} surfaces. Therefore, the initial seed remains at one of the ends of the final nanorod. In the case of the tapered rods, the axial growth initially occurs on one of the available {111} surface sets of the rounded particle. The radial growth along the dissolved edge occurs simultaneously, steadily adding new atomic sites for further axial growth. However, since these new sites begin axial growth after the initially available {111} surfaces, the result is the formation of a radial gradient along the length of the rod as it elongates, *i.e.* tapering. This gradient disappeared when the radial growth terminated upon producing a sharp decahedral configuration (Figure 4.8C), resulting in constant rod diameters at the wider end of the tapered structure.

This can be clearly seen in the longer tapered rods, shown in Figure 4.8B.

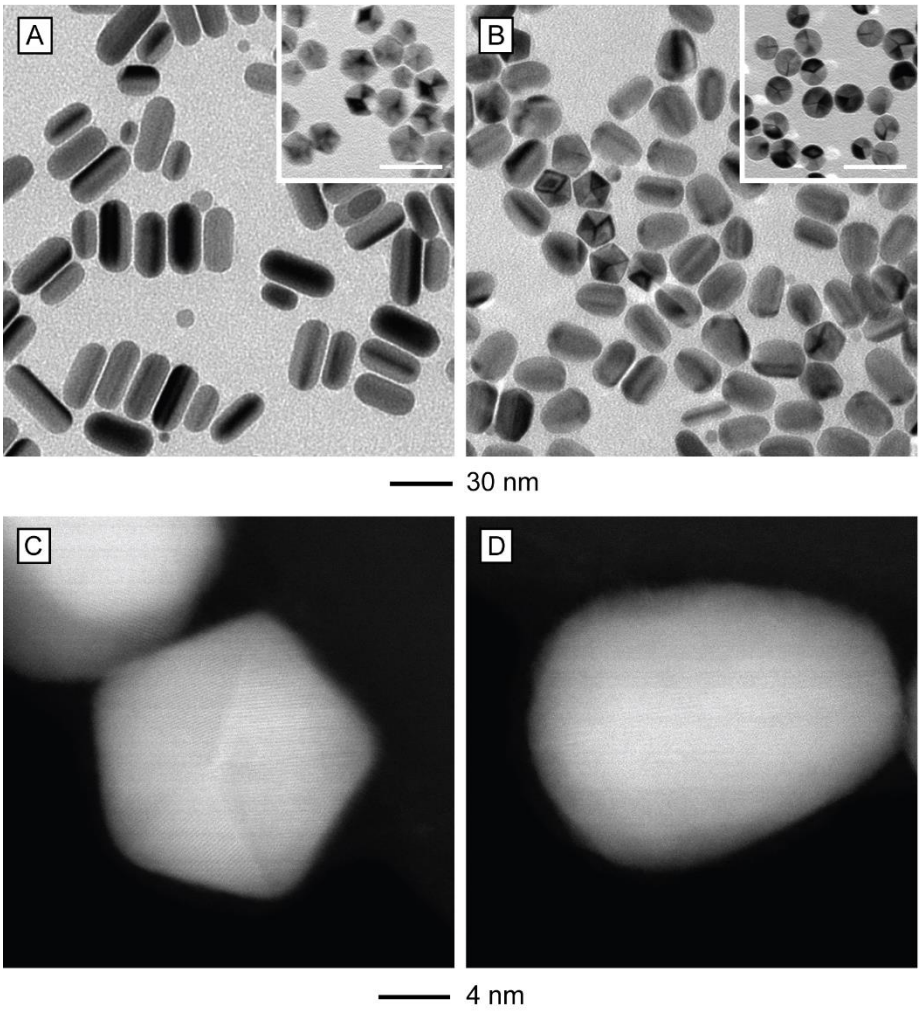

Figure 4.8. TEM images of Pd (A) standard and (B) tapered nanorods obtained through seeded growth from the original and rounded Pd decahedra, respectively. Insets show TEM images of the corresponding seeds (scale bars: 40 nm). (C, D) HAADF-STEM images of the end and side of a tapered nanorod, respectively.

4.3 Conclusion

In summary, I have carried out a systematic study to understand the oxidative etching of Pd decahedral nanocrystals by the O_2/I^- pair under different conditions. Electron microscopy analyses of the etched particles revealed significant rounding of the penta-twinned decahedra due to the removal of atoms from the equatorial vertices and edges. It was found that the etching began from the equatorial vertices, with the formation of re-

entrant grooves, and then proceeded along the equatorial edges by removing the low-coordination Pd atoms until a rounded structure was attained. The etching behaviors in DEG and DI water differed significantly, with the former producing rounded particles and the latter preserving the initial shape. The addition of a sufficient amount of AA into the water-based system resulted in the formation of rounded structures, revealing the need for an adequately reducing environment in order to initiate oxidative etching. This phenomenon can be attributed to the presence of a protective oxide layer on the surface of the Pd decahedra, which had to be removed first through reduction before etching could occur. Finally, I utilized the rounded particles as seeds for the growth of pentagonal Pd nanorods with asymmetric, tapered structures, due to the involvement of both axial and radial growth.

4.4 Experimental Section

Chemicals and Materials. DEG (≥99.0%, Lot #BCBP6902V), poly(vinyl pyrrolidone) (PVP, MW≈55 000), sodium sulfate (Na_2SO_4, ≥99.0%), sodium iodide (NaI, ≥99.5%), sodium chloride (NaCl, ≥99.0%), iron (III) chloride ($FeCl_3$, 97%), and ascorbic acid (AA, ≥99.0%) were all procured from Sigma-Aldrich. Sodium tetrachloropalladate (Na_2PdCl_4, ≥99.0%) was obtained from Acros Organics. All chemicals were used as received. DI water with a resistivity of 18.2 MΩ·cm was used throughout the experiment.

Synthesis of Pd Decahedra. In a typical synthesis, 174 mg of Na_2SO_4 was added into a 50 mL three-neck flask. Next, 8 mL of DEG-based PVP solution (20 mg/mL) was introduced, along with a 6 x 25 mm polygonal, Teflon-coated stirring bar. The flask was then placed in an oil bath set to 117.5 °C under magnetic stirring (450 rpm). Note that at this oil bath temperature, the temperature of the reaction solution was only measured to be 103.3 °C. Immediately after the stirring began in the flask, 4 mL of a DEG-based Na_2PdCl_4 solution (15.5 mg/mL) was introduced and the timer started. The reaction was terminated after 3 h by immersing the flask in an ice bath. The product was collected by adding acetone

in a 3:1 ratio to the reaction solution and centrifuging the mixture at 6000 rpm for 10 min. The precipitate was re-dispersed in DI water, centrifuged three times at 16000 rpm for 25 min, and finally stored in DI water.

Etching of Pd Decahedra. In a standard procedure, 52.5 mg of PVP and 10 mg of NaI were dissolved in 3.5 mL of DEG. The resultant solution was placed in a 20 mL dram vial with a 10 x 15 mm polygonal stirring bar. The vial was loosely closed and then heated in an oil bath set to 90 °C for 10 min under stirring (450 rpm). After the preheating was complete, 0.5 mL of the Pd decahedra suspension (1.35 mg Pd/mL) was injected with a pipette and the vial was capped again. The etching was allowed to proceed for 30 min and was terminated by immersion in an ice bath. The product was collected by adding acetone in a 3:1 ratio to the reaction solution and centrifuging at 6000 rpm for 10 min. The precipitate was re-dispersed in DI water, centrifuged three times at 16000 rpm for 25 min, and then stored in DI water.

Synthesis of Tapered, Penta-Twinned Pd Nanorods. In a typical process, 7 mL of DEG containing 105 mg of PVP, 100 mg of AA, and 100 mg of NaI was added into a 20 mL vial equipped with a 10 x 15 mm polygonal, Teflon-coated stirring bar. The vial was then capped and placed in an oil bath held at 160 °C under magnetic stirring (450 rpm). After 10 min, 1 mL of rounded particles in DEG was added, immediately followed by the introduction of 3 mL of a DEG solution of Na_2PdCl_4 (10 mg/mL). The reaction was allowed to proceed for 1 h and terminated by immersing the vial in an ice-water bath. The product was collected by adding acetone in a 3:1 ratio to the reaction solution and centrifuging at 6000 rpm for 10 min. The collected precipitate was re-dispersed in DI water and centrifuged three times at 16500 rpm for 25 min.

Instrumentation. TEM images were obtained on a Hitachi HT-7700 microscope operated at 120 kV. HRTEM and HAADF-STEM images were collected with a Hitachi HD-2700 operated at 200 kV. An Eppendorf centrifuge (5430) was used for the centrifugation and washing of all samples.

4.5 Notes to Chapter 4

Part of this chapter is adapted from the paper "Oxidative Etching of Pd Decahedral Nanocrystals with a Penta-twinned Structure and Its Impact on Their Growth Behavior" submitted for publication in *Chemistry of Materials*.

4.6 References

[1] Zheng, Y.; Zeng, J.; Ruditskiy, A.; Liu, M.; Xia, Y. *Chem. Mater.* **2014**, *26*, 22−33.

[2] Long, R.; Zhou, S.; Wiley, B.J.; Xiong, Y. *Chem. Soc. Rev.* **2014**, *43*, 6288−6310.

[3] Mulvihill, M.J.; Ling, X.Y.; Henzie, J.; Yang, P. *J. Am. Chem. Soc.* **2010**, *132*, 268−274.

[4] Zhang, H.; Jin, M.; Wang, J.; Li, W.; Camargo, P.H.C.; Kim, M.J.; Yang, D.; Xie, Z.; Xia, Y. *J. Am. Chem. Soc.* **2011**, *133*, 6078−6089.

[5] He, D. S.; He, D.; Wang, J.; Lin, Y.; Yin, P.; Hong, X.; Wu, Y.; Li, Y. *J. Am. Chem. Soc.* **2016**, *138*, 1494–1497.

[6] Zhang, L.; Roling, L.T.; Wang, X.; Vara, M.; Chi, M.; Liu, J.; Choi, S.-I.; Park, J.; Herron, J.A.; Xie, Z.; Mavrikakis, M.; Xia, Y.; *Science* **2015**, *349*, 412–416.

[7] Wang, X.; Figueroa-Cosme, L.; Yang, X.; Luo, M.; Liu, J.; Xie, Z.-X.; Xia, Y. *Nano Lett.* **2016**, *16*, 1467−1471.

[8] Wang, X.; Vara, M.; Luo, M.; Huang, H.; Ruditskiy, A.; Park, J.; Bao, S.; Liu, J.; Howe, J.; Chi, M.; Xie, Z.; Xia, Y. *J. Am. Chem. Soc.* **2015**, *137*, 15036–15042.

[9] McEachran, M.; Keogh, D.; Pietrobon, B.; Cathcart, N.; Gourevich, I.; Coombs, N.; Kitaev, V. *J. Am. Chem. Soc.* **2011**, *133*, 8066–8069.

[10] Chen, C.; Kang, Y.; Huo, Z.; Zhu, Z.; Huang, W.; Xin, H.L.; Snyder, J.D.; Li, D.; Herron, J.A.; Mavrikakis, M.; Chi, M.; More, K.L.; Li, Y.; Markovic, N.M.; Somorjai, G.A.; Yang, P.; Stamenkovic, V.R. *Science* **2014**, *343*, 1339−1343.

[11] Wang, X.; Ruditskiy, A.; Xia, Y. *Natl. Sci. Rev.* **2016**, *3*, 520–533.

[12] Wiley, B.; Herricks, T.; Sun, Y.; Xia, Y. *Nano Lett.* **2004**, *4*, 1733−1739.

[13] Wiley, B.J.; Xiong, Y.; Li, Z.-Y.; Yin, Y.; Xia, Y. *Nano Lett.* **2006**, *6*, 765–768.

[14] Wang, Z.; Wang, H.; Zhang, Z.; Yang, G.; He, T.; Yin, Y.; Jin, M. *ACS Nano* **2016**, *11*, 167–170.

[15] Yang, Y.; Zhang, Q.; Fu, Z.-W.; Qin, D. *ACS Appl. Mater. Interfaces* **2014**, *6*, 3750−3757.

[16] Ye, X.; Jones, M.R.; Frechette, L.B.; Chen, Q.; Powers, A.S.; Ercius, P.; Dunn, G.; Rotskoff, G.M.; Nguyen, S.C.; Adiga, V.P.; Zettl, A.; Rabani, E.; Geissler, P. L.; Alivisatos, A. P. *Science* **2016**, *354*, 874−877.

[17] Marks, L.D.; Peng, L. *J. Phys.: Condens. Matter* **2016**, *28*, 053001.

[18] Choi, S.-I.; Herron, J. A.; Scaranto, J.; Huang, H.; Wang, Y.; Xia, X.; Lv, T.; Park, J.; Peng, H.-C.; Mavrikakis, M.; Xia, Y. *ChemCatChem* **2015**, *7*, 2077–2084.

[19] Luo, M.; Huang, H.; Choi, S.-I.; Zhang, C.; Silva, R. R.; Peng, H.-C.; Li, Z.-Y.; Liu, J.; He, Z.; Xia, Y. *ACS Nano* **2015**, *9*, 10523–10532.

[20] Luo, M.; Ruditskiy, A.; Peng, H.-C.; Tao, J.; Figueroa-Cosme, L.; He, Z.; Xia, Y. *Adv. Funct. Mater.* **2016**, *26*, 1209–1216.

[21] Huang, H.; Zhang, L.; Lv, T.; Ruditskiy, A.; Liu, J.; Ye, Z.; Xia, Y. *ChemNanoMat* **2015**, *1*, 246–252.

[22] Griffith, W.P.; Robinson, S.D.; Swars, K. *Gmelin Handbook of Inorganic Chemistry, 8th Edition, Supplement Volume B 2, Pd Compounds*, Springer-Verlar, Berlin, Heidelberg, **1989**, 208–210.

[23] Sneed, B. T.; Young, A. P.; Tsung, C.-K. *Nanoscale* **2015**, *7*, 12248−12265.

[24] Yamamoto, H.; Tokunaga, J. *J. Chem. Eng. Data* **1994**, *39*, 544−547.

[25] Skrabalak, S.E.; Wiley, B.J.; Kim, M.; Formo, E.V.; Xia, Y. *Nano Lett.* **2008**, *8*, 2077–2081.

[26] Ruditskiy, A.; Zhao, M.; Gilroy, K.D.; Vara, M.; Xia, Y. *Chem. Mater.* **2016**, *28*, 8800–8806.

[27] Zemlyanov, D.; Klotzer, B.; Gabasch, H.; Smeltz, A.; Ribeiro, F.H.; Zafeiratos, S.; Teschner, D.; Schnorch, P.; Vass, E.; Havecker, M.; Knop-Gericke, A.; Schlogl, R. *Top Catal.* **2013**, *56*, 885–895.

CHAPTER 5

RATIONAL DESIGN AND SUCCESSFUL EXECUTION OF A PROTOCOL FOR THE ONE-POT SYNTHESIS OF PALLADIUM PENTA-TWINNED NANOWIRES

5.1 Introduction

Palladium nanocrystals have received considerable attention as a primary catalyst for the electro-oxidation of formic acid (FAO) and therefore the fabrication of direct formic acid fuel cells (DFAFCs) [1−3]. Tremendous efforts have been devoted to the synthesis of Pd nanocrystals with diversified shapes as a means to tailor their catalytic activity through surface structure engineering [4, 5]. To this end, Pd nanocrystals with a wide variety of shapes, including tetrahedra [6], cubes [7, 8], octahedra [9], decahedra [10], icosahedra [10, 11], right bipyramids [12], and penta-twinned nanorods or nanowires [13, 14], have all been reported in recent years. Among them, penta-twinned nanowires are particularly attractive as a viable electrocatalyst toward FAO owing to the presence of both {100} facets and twin boundaries on the surface. The one-dimensional morphology is also advantageous for the development of a support-free catalytic system with enhanced durability as compared to the conventional ultrafine particles [15].

Like other metals, there is no intrinsic driving force for Pd atoms to grow into nanowires (or nanorods) with a highly anisotropic morphology due to the isotropy in interaction among the atoms [4, 16]. As a result, it has been difficult to synthesize Pd penta-twinned nanowires as uniform samples in large quantities. Nevertheless, there exist several reports in literature. Using a hydrothermal process at 200 ^{o}C, Zheng and co-workers demonstrated the synthesis of Pd penta-twinned nanowires with an average diameter of 9 nm and lengths up to 3 μm [13]. Although it was a significant advance, the authors offered essentially no discussion of the underlying mechanism. Subsequently, Huang and co-

workers also prepared Pd penta-twinned nanowires using a hydrothermal route [14]. The authors attributed the success of their synthesis to good control over oxidative etching, caused by O_2/halides, through the introduction of small organic molecules to scavenge the halide ions, thus limiting their availability in the solution. Similar to what had been established for the synthesis of Ag nanowires [17], the suppression of oxidative etching could protect the twinned seeds from being oxidized and dissolved during the initial stage of the synthesis. However, no mechanistic insight was presented with regard to the formation of decahedral seeds [4, 16]. Indeed, the formation of decahedral seeds represents a critical step in the synthesis of penta-twinned nanowires. As established in recent studies, the reaction kinetics play a pivotal role in controlling the formation of Pd seeds with a decahedral structure [18]. It was further demonstrated that the Pd decahedral seeds could be employed to produce penta-twinned nanorods made of Pd, Ag, and Cu through seed-mediated growth [19−21]. In addition to the involvement of a two-step process, the aspect-ratios of these nanorods were typically limited to values below 10.

In this Chapter, my collaborator and I rationally designed and successfully implemented a one-pot protocol for the facile synthesis of Pd penta-twinned nanowires with an average diameter as thin as 7.8 nm and aspect-ratios up to 100. The protocol was based upon the reduction of a Pd(II) precursor by a combination of diethylene glycol and ascorbic acid. By controlling the amounts of NaI and HCl, introduced to form PdI_4^{2-} species and inhibit the dissociation of ascorbic acid, respectively, the initial reduction rate could be tuned into the right regime for the generation of Pd decahedral seeds. The relatively slow reduction rate associated with PdI_4^{2-} was also instrumental to the induction and continuation of one-dimensional growth along the penta-twinned axis of a decahedral seed. Furthermore, the I^- ions could serve as a selective capping agent toward the Pd(100) surface, thereby promoting the formation of penta-twinned nanorods and then nanowires. When the reaction time was prolonged, however, the nanowires were observed to evolve into multiply twinned particles without defined geometry. Our analysis implies that

oxidative etching was responsible for the destabilization of the penta-twinned nanowires when they were suspended in a solution phase containing halide ions and exposed to oxygen from the air at an elevated temperature. The penta-twinned Pd nanowires showed enhanced catalytic activity toward FAO, with a current density three times greater than the commercial Pd/C catalyst. Finally, using the as-prepared Pd nanowires as sacrificial templates, we also demonstrated the fabrication of Pd@Pt core-sheath nanowires and Pd-Pt nanotubes.

5.2 Results and Discussion

Characterizations of the Pd Nanowires. We first analyzed the as-obtained nanowires using XRD. As shown in Figure 5.1, all the peaks could be indexed to the diffraction from *fcc* Pd (JCPDS No. 46-1043). No other crystalline phases such as PdO were detected. As shown in the TEM image (Figure 5.2A), the Pd nanowires had an average length of 720 nm, together with a purity over 85%. Figure 5.2B shows another TEM image of the Pd nanowires recorded at a higher magnification, highlighting good uniformity along each nanowire, together with an average diameter of 7.8 nm. The HAADF-STEM image in Figure 5.2C further confirmed the good uniformity in diameter along the long axis of an individual nanowire. A closer look at the nanowire ends (Figure 5.2D) revealed the presence of a penta-twinned structure. A straight twin boundary could be seen running along the length of the nanowire, as marked by the red arrow. The lattice fringes only appeared on one side of the imaged nanowire, indicating that the direction of the incident electron beam was parallel to one of the five side faces, as schematically illustrated in the inset of Figure 5.2D. Such an orientation corresponds to the superposition of <110> and <111> zones [22]. The HRTEM image taken from the middle section of a nanowire (Figure 5.2E) clearly shows lattice fringes with spacing of 0.23 and 0.20 nm, which could be indexed to the {111} and {200} planes of *fcc* Pd, respectively. The Fourier transform (FT) pattern displayed in Figure 5.2F could be assigned to two sets of diffraction patterns

corresponding to the <110> and <111> zones of Pd, further confirming the existence of twinned planes in the nanowire. Taken together, we can conclude that the Pd nanowires possessed a penta-twinned structure bound by ten {111} facets at the two ends and five {100} side facets, which is a common feature of one-dimensional metal nanostructures composed of *fcc* metals such as Cu, Ag, and Au [22, 33].

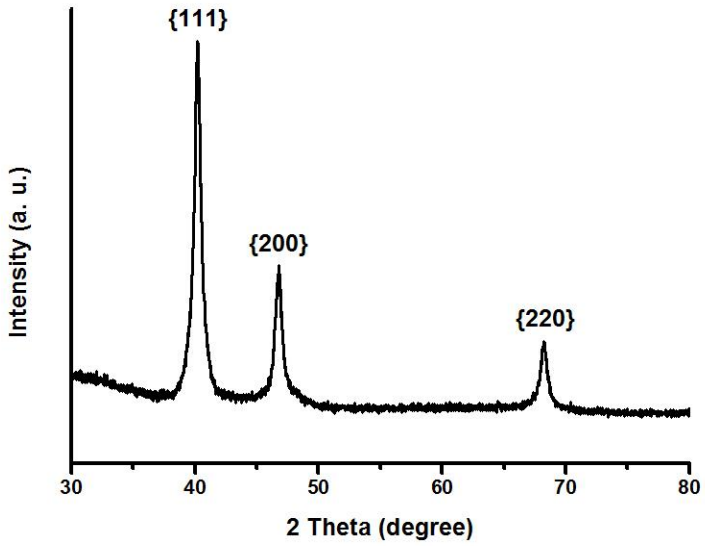

Figure 5.1. XRD pattern of the Pd nanowires obtained using the standard procedure with a reaction time of 1 h.

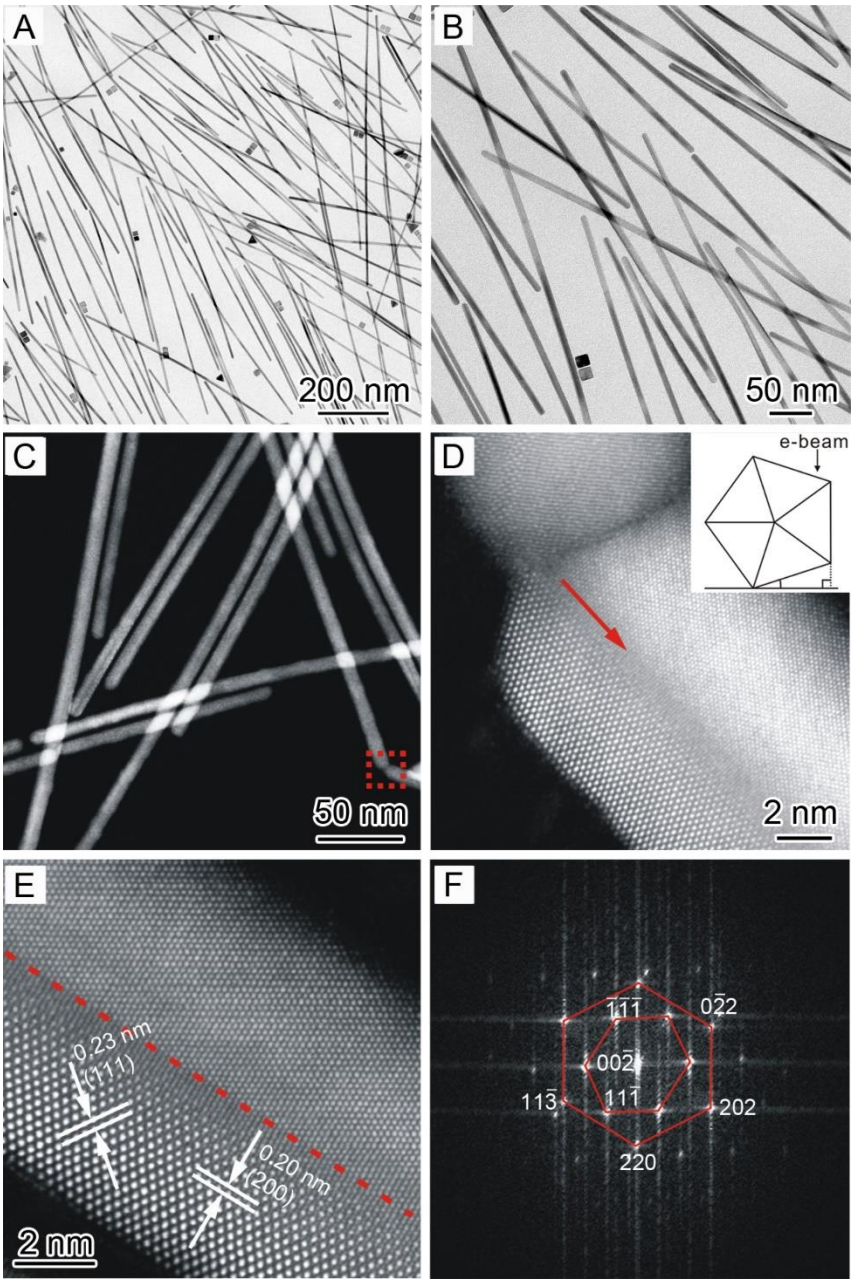

Figure 5.2. Morphological and structural characterization of the Pd nanowires obtained using the standard procedure. (A, B) TEM images at low and high magnifications, respectively, and (C) HAADF-STEM image. (D, E) HRTEM images of the region marked by a dashed box in (C) and the middle section of a nanowire, respectively. The red arrow and dotted line indicate the twin boundary running along the long axis of the nanowire. The inset in (D) illustrates the orientation of the electron beam relative to the nanowire. (F) Fourier transform pattern derived from the lattice fringes in (E).

The Effect of Reduction Kinetics on the Formation of Pd Nanowires. In order to elucidate the driving forces behind the initial formation of Pd decahedral seeds, we studied the reaction kinetics underlying the nanowire synthesis. Previous work has shown that the type of seed generated during the nucleation phase can be controlled by tuning the initial reduction rate of a salt precursor into the proper regime [18, 34]. The synthesis of Pd nanowires is a significantly more complicated system compared to those described in the previous reports on this subject. Specifically, in the nanowire synthesis, both DEG and AA served as reducing agents, with the reducing power of AA dependent on the concentration of HCl. However, since both of these components are in excess when compared to the Pd(II) precursor, we can approximate the reaction system as pseudo-first order. To quantify the kinetic parameters for the nanowire synthesis, we used UV-vis to measure the concentration of Pd(II) precursor remaining in the solution over the course of reaction. The experiment was conducted for both the standard synthesis and a modified procedure in which the I^- was substituted by a molar-equivalent of Br^- in order to quantify the impact of a specific halide on the reaction kinetics. Figure 5.3A shows a TEM image of the Pd nanostructures obtained by replacing I^- with Br^- in the standard synthesis. The products consisted of a mixture of decahedra (marked by the blue arrows), truncated right bipyramids (marked by the red arrows), and nanocubes. To better distinguish the shapes of a decahedron and a truncated right bipyramid, their corresponding 3D models are presented in Figures 5.3B and C, respectively.

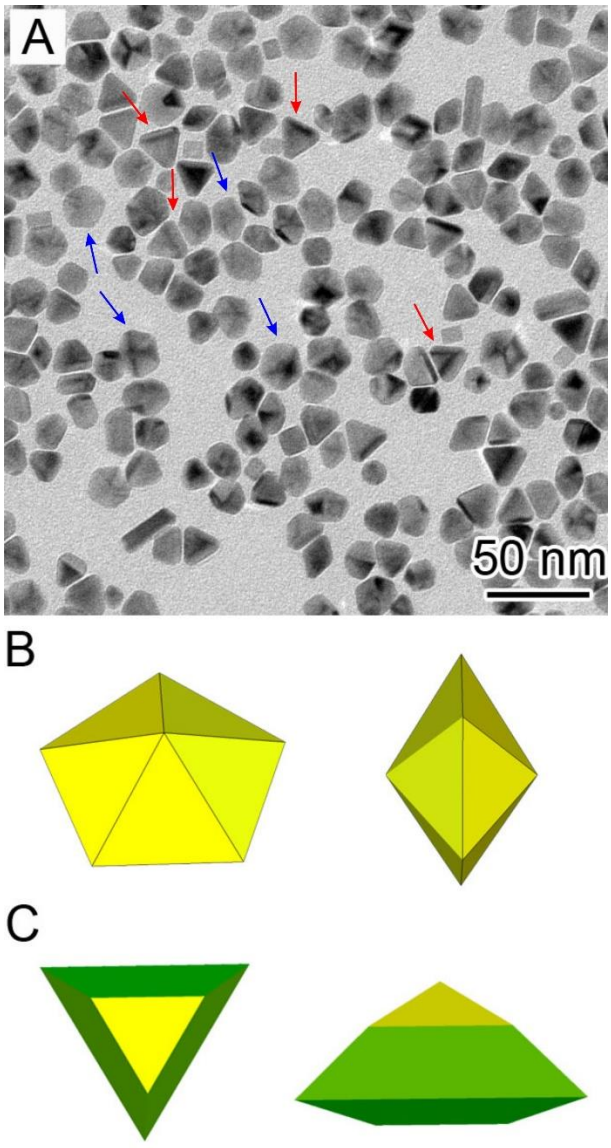

Figure 5.3. (A) TEM images of Pd nanostructures obtained using the standard procedure with the substitution of NaI by 69 mg of KBr. (B, C) 3D models of the decahedron and truncated bipyramid, respectively, and two different orientations.

When the initial $PdCl_4^{2-}$ precursor is exposed to an excess amount of Br^- or I^-, rapid ligand exchange will occur, generating a PdI_4^{2-} or a $PdBr_4^{2-}$ complex. This change is driven by the greater stability of the resultant complexes, with the stability trending in the order of $PdCl_4^{2-} < PdBr_4^{2-} < PdI_4^{2-}$ [25]. In the case of standard synthesis, the characteristic absorption peak of PdI_4^{2-} at 408 nm was used to track the Pd(II) precursor concentration,

while for the modified procedure the 332 nm absorption peak corresponding to $PdBr_4^{2-}$ was utilized. The reaction was sampled in 5 min intervals for the duration of one hour. The concentration of the Pd(II) precursor remaining in solution is directly proportional to the absorbance of the characteristic peak. Using this information, the rate constant for the reduction can be obtained by plotting the integrated form of the pseudo-first-order reaction rate law:

$$\ln[A]_t = -kt + \ln[A]_0 \quad (1)$$

where $[A]_0$ and $[A]_t$ represent the concentrations of the Pd(II) precursor at the beginning of a synthesis and at a specific time point, respectively; k is the rate constant; and t is time. The derived plots for both the iodide- and bromide-mediated nanowire syntheses are shown in Figure 5.4. The iodide-mediated synthesis showed a slow, linear decline in $\ln[Pd^{2+}]$ over the course of one hour, as expected from a pseudo-first order reaction. On the other hand, the decline in $\ln[Pd^{2+}]$ for the bromide-mediated reaction was comparatively rapid, with the characteristic absorption peak disappearing after 15 min of reaction. This result suggests a significantly more rapid reduction rate in the case of the bromide-mediated system, which is consistent with the relative stabilities of the PdI_4^{2-} and $PdBr_4^{2-}$ complexes. The k values, derived from the slope of the fitted lines, were found to be 4.82×10^{-5} and 1.75×10^{-3} s^{-1} for the iodide- and bromide-mediated reactions, respectively. The more than two orders of magnitude difference between the rate constants confirms the significantly faster reduction in the bromide-mediated system. Notably, the rate constant of the iodide-mediated reaction was nearly identical to that of the sulfate-mediated synthesis of Pd decahedra (5.95×10^{-5} s^{-1}), which was previously reported [18]. This result strongly suggests that Pd decahedral seeds are created in the initial stage of a nanowire synthesis, and the seeds subsequently evolve into pentagonal nanowires through axial overgrowth. When the k values are multiplied by the initial concentration of $PdCl_4^{2-}$ (9.27×10^{-3} M),

we obtain the initial reduction rates (r_o): 4.47×10^{-7} and 1.62×10^{-5} $M \cdot s^{-1}$ for the iodide- and bromide-mediated syntheses, respectively.

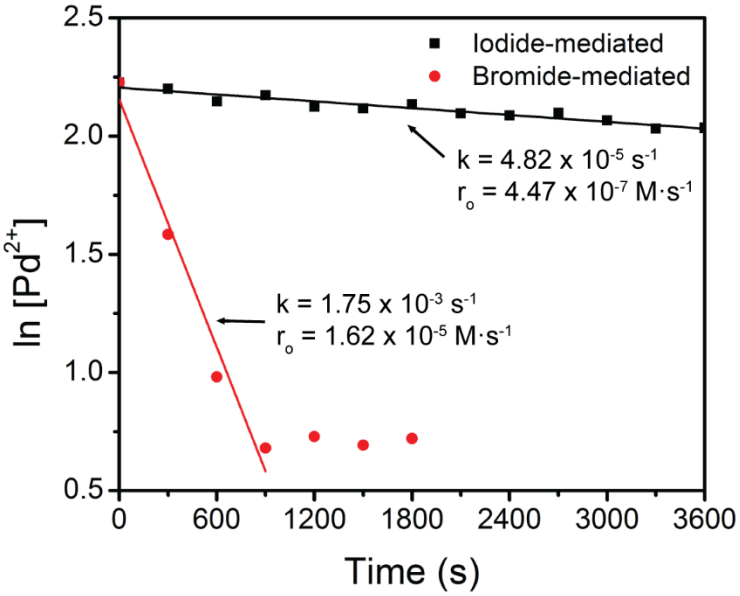

Figure 5.4. Plot showing the natural log of Pd(II) concentration over time for the iodide- and bromide-mediated nanowire syntheses. For the bromide-mediated synthesis, the characteristic peak of $PdBr_4^{2-}$ disappeared after 15 min due to the involvement of rapid reduction. The rate constant (k) and initial reduction rate (r_o) are labeled on the fitting curves.

To further study the impact of the reduction kinetics, we varied the concentrations of Na_2PdCl_4 and NaI. As shown in Figure 5.5A, increasing the amount of Na_2PdCl_4 to 45 mg produced a mixture of Pd nanocubes (with an average size of 14 nm) and right bipyramids (with an average size of 30 nm). When the amount of Na_2PdCl_4 was decreased to 25 mg, uniform Pd nanowires were obtained (Figure 5.5B). Further decreasing the amount of Na_2PdCl_4 to 15 mg resulted in no solid product in the reaction system, due to the very slow reduction rate. Variation in the amount of NaI added could also be used to adjust the reaction kinetics. Since PdI_4^{2-} is more stable than $PdCl_4^{2-}$, a high concentration of NaI would appreciably slow the reduction rate [26, 27]. As illustrated in Figures 5.5C and D, short Pd nanowires, as well as right bipyramids and small amounts of nanocubes, were produced if 150 mg of NaI was used. In contrast, the product contained 15% of right

bipyramids and 85% of nanocubes when the amount of NaI was reduced to 50 mg. All these results consistently indicate that the formation of Pd nanowires requires a relatively slow reduction rate for the precursor. It should be noted, however, that changing the concentration of I^- not only impacts the reduction kinetics, but also influences the capping of Pd(100) facets and the rate of oxidative etching.

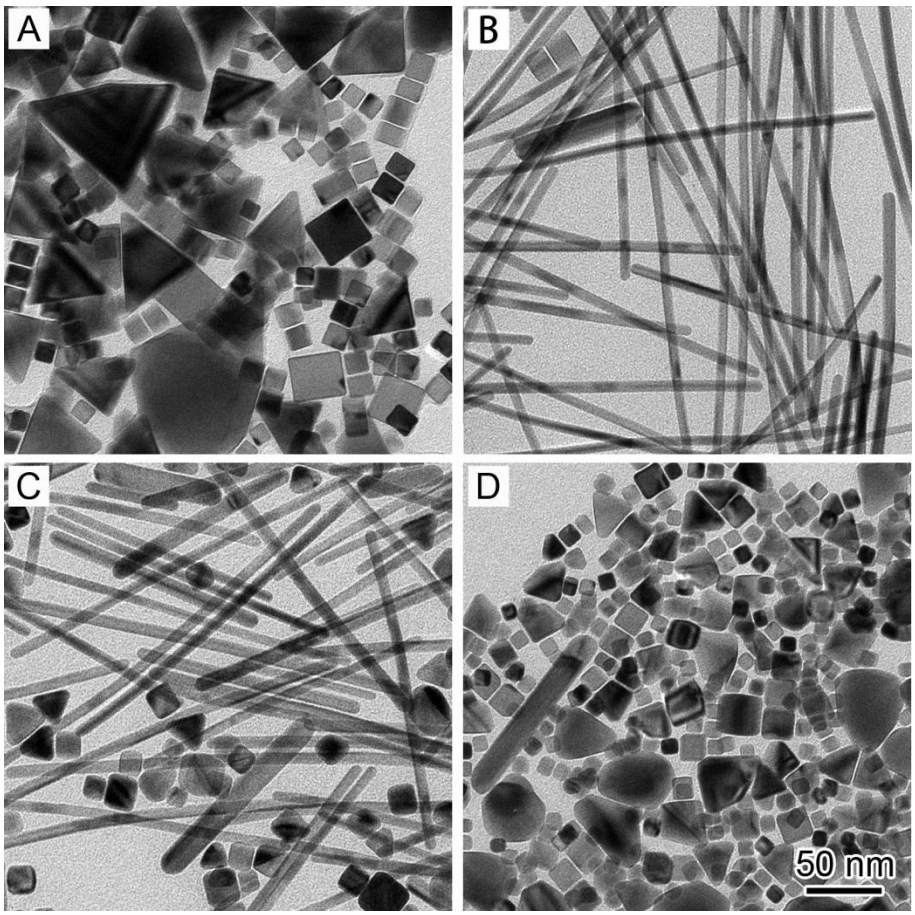

Figure 5.5. TEM images of Pd nanostructures obtained using the standard procedure with the addition of different amounts of Na_2PdCl_4: (A) 45 and (B) 25 mg, respectively; and different amounts of NaI: (C) 150 and (D) 50 mg, respectively.

On the basis of the experimental investigations described above, we can posit a mechanism for the formation of the Pd nanowires, summarized in Figure 5.6. Immediately after the injection of the Na_2PdCl_4 precursor into the reaction solution, the $PdCl_4^{2-}$ complex is converted to PdI_4^{2-} because of ligand exchange with the excess I^-. The PdI_4^{2-} complex

then undergoes reduction by the combination of DEG and AA, producing Pd(0) atoms. The reducing power of AA is moderated through the introduction of H^+ ions from HCl, which serve to inhibit the dissociation of AA into ascorbate monoanion, which is a much stronger reducing agent than AA. When the concentration of Pd(0) atoms reaches supersaturation, homogenous nucleation occurs, resulting in the formation of decahedral seeds. The remaining I^- ions act as a capping agent to passivate the Pd(100) facets of the decahedra, as previously observed for the seeded growth of Pd nanorods [19]. Consequently, the subsequent nucleation of Pd(0) is heterogeneous, occurring on the Pd(111) surfaces of the decahedra. Additionally, the slow reduction of PdI_4^{2-} limits the supply of Pd(0), further promoting the asymmetric overgrowth of the decahedra. The result is the axial growth of the decahedra along the <110> direction, thereby generating pentagonal nanorods and, after further growth, nanowires. This mechanism is consistent with those proposed for the syntheses of Cu and Ag nanowires with a pentagonal cross-section [17, 22, 23].

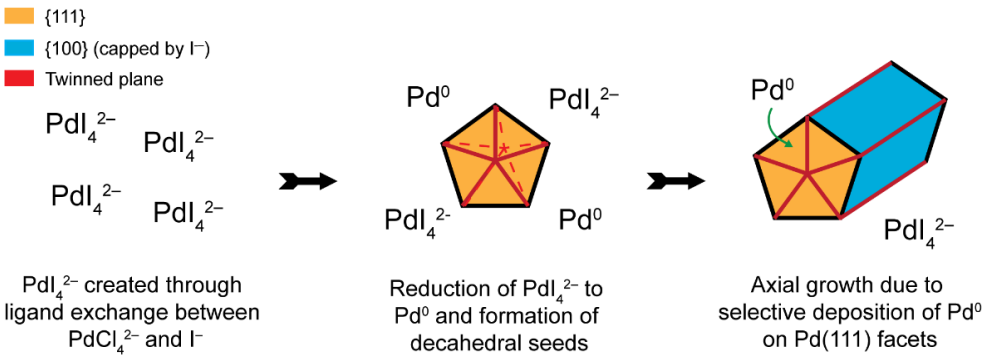

Figure 5.6. A schematic illustration of the nucleation and growth pathway for the formation of Pd nanowires with a penta-twinned structure. Homogeneous nucleation of Pd atoms initially produces decahedral seeds. The capping of the Pd(100) facets by I^- induces selective deposition of Pd atoms on the Pd(111) facets, resulting in the formation of pentagonal nanowires.

Oxidative Etching and Stability of the Pd Nanowires. As mentioned in the introduction, previous attempts to synthesize Pd nanowires showed product instability at long reaction times. In order to follow the structural evolution of Pd nanowires, we

characterized the products sampled at different stages of a synthesis by TEM. At t = 0.5 h (Figure 5.7A), the sample mainly contained nanowires with an average diameter of 7.5 nm and an average length of 450 nm. As the reaction time was extended to t = 1.5 h, however, a small number of irregular particles appeared, as shown in Figure 5.7B. These particles exhibited a tadpole-like geometry (with one end being significantly larger than the other), together with a multiply twinned structure. Upon closer examination by TEM (Figure 5.8), it was found that most of these particles were positioned at the ends of short Pd nanowires. As the reaction continued, the number and size of such irregular particles also increased. At t = 2 h (Figure 5.7C), the tadpole-like particles grew to 200-400 nm in length while the average length of the nanowires could reach 2 μm. At t = 4 h (Figure 5.7D), essentially all of the Pd nanowires disappeared, with only multiply twinned particles remaining in the sample. The XRD pattern (Figure 5.9) recorded from these multiply twinned particles only showed peaks corresponding to *fcc* Pd, indicating that the particles and nanowires had the same composition. These observations clearly indicate that the penta-twinned Pd nanowires were not stable in the reaction solution under ambient conditions at an elevated temperature. Zheng and co-workers also reported that their Pd nanowires would first shrink to Pd nanorods and then transform into multiply twinned particles as the reaction time was extended to 24 h [13]. However, no detailed mechanistic discussion was provided in that report. The intrinsic instability of the penta-twinned Pd nanowires is likely responsible for the limited number of reports on their synthesis in the literature.

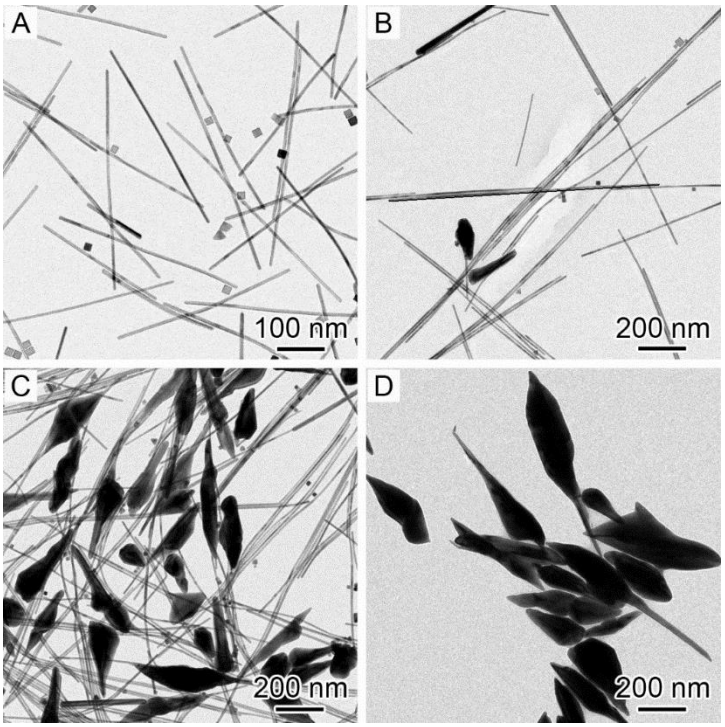

Figure 5.7. TEM images of the samples obtained at various reaction times for a standard nanowire synthesis: (A) 0.5, (B) 1.5, (C) 2, and (D) 4 h, respectively.

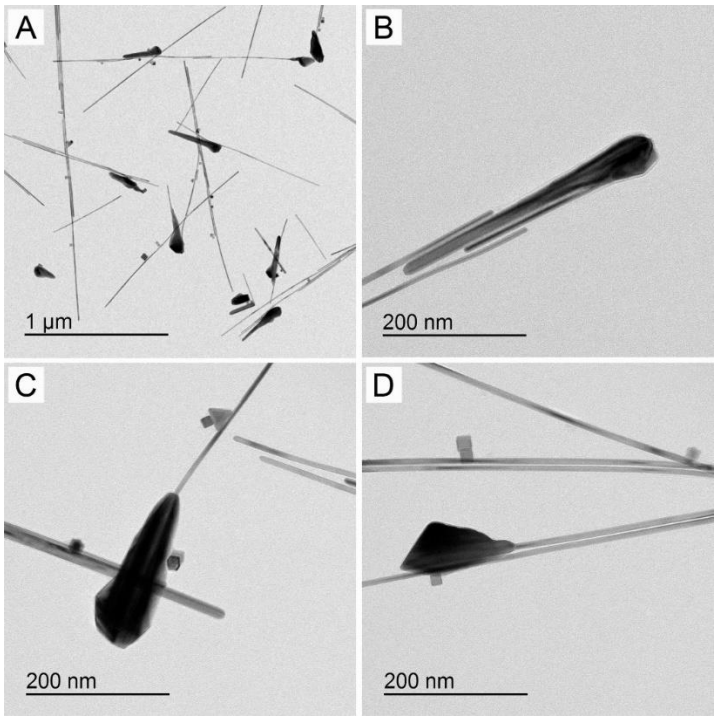

Figure 5.8. (A) Low- and (B-D) high-magnification TEM images of the Pd nanostructures obtained using the standard procedure with a reaction time of 1.5 h.

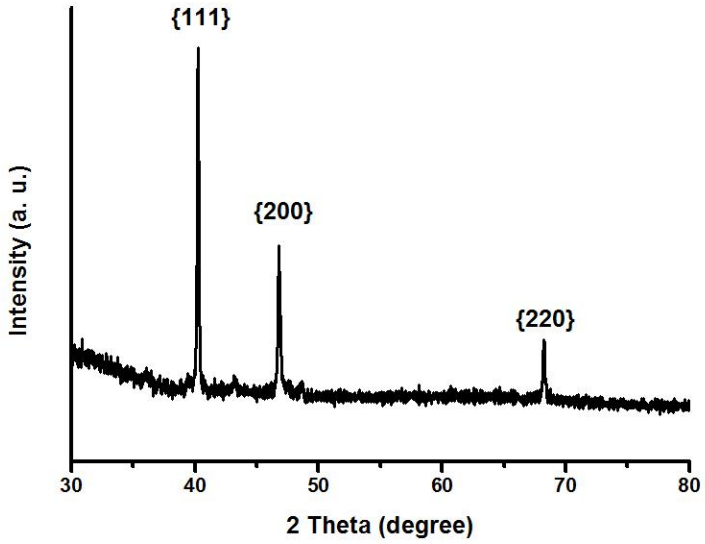

Figure 5.9. XRD pattern of the irregular twinned nanostructures (shown in Figure 5.4D) obtained using the standard procedure with a reaction time of 4 h.

To elucidate the mechanism responsible for the instability of Pd nanowires, we designed and conducted a set of experiments. To simplify the study, we dispersed the purified Pd nanowires prepared using the standard procedure in DEG containing different chemical species and then monitored their morphological changes as a function of aging time. As shown in Figure 5.10A, the shape of the nanowires was retained after aging at 160 ^{o}C for 4 h in the presence of PVP (15 mg/mL). When the aging time was extended to 12 h, short nanorods with varying diameters and rough surfaces were observed (Figure 5.10B). In contrast, most of the Pd nanowires were quickly broken into small particles after aging in a DEG solution containing NaI (50 mg/mL), PVP (15 mg/mL), and HCl (30 mM) for just 10 min (Figure 5.10C). If the aging time was increased to 60 min, Pd particles much larger in size would be formed, as shown in Figure 5.10D. The TEM image in the inset reveals that the as-obtained particles possessed a multiply twinned structure. These observations indicate that the presence of NaI and HCl was responsible for the instability of the penta-twinned Pd nanowires suspended in a solution phase. Similar to Cl^{-}, I^{-}

contributes to the oxidative etching of Pd nanostructures by promoting the formation of a PdI_4^{2-} stable complex and acting as a charge carrier, according to the following reaction equation [10, 28, 29]:

$$Pd + O_2 + 4I^- + 4H^+ \longrightarrow PdI_4^{2-} + 2H_2O \quad (2)$$

From eq(2), it is clear that O_2 could act as an oxidant and play a critical role in destabilizing the Pd nanowires. To validate the proposed mechanism, we bubbled argon through the DEG solution containing PVP (15 mg/mL), NaI (50 mg/mL), and HCl (30 mM). Figure 5.10E shows a TEM image of the products obtained after aging at 160 °C for 60 min, revealing that most of the Pd nanowires were retained. Although argon was bubbled into the DEG system, there was still a minor oxidative etching effect, as shown in Figure 5.11F. Some of the nanowires were found to have roughened side faces (boxed by the large dashed rectangle) as well as fractures (boxed by the small dashed rectangle). Considering these observations, we believe that the oxidative etching likely began at the high-energy twinned boundaries running along the sides of the Pd nanowires, causing fragmentation of the Pd nanowires into short nanorods and small particles, as the synthesis was continued.

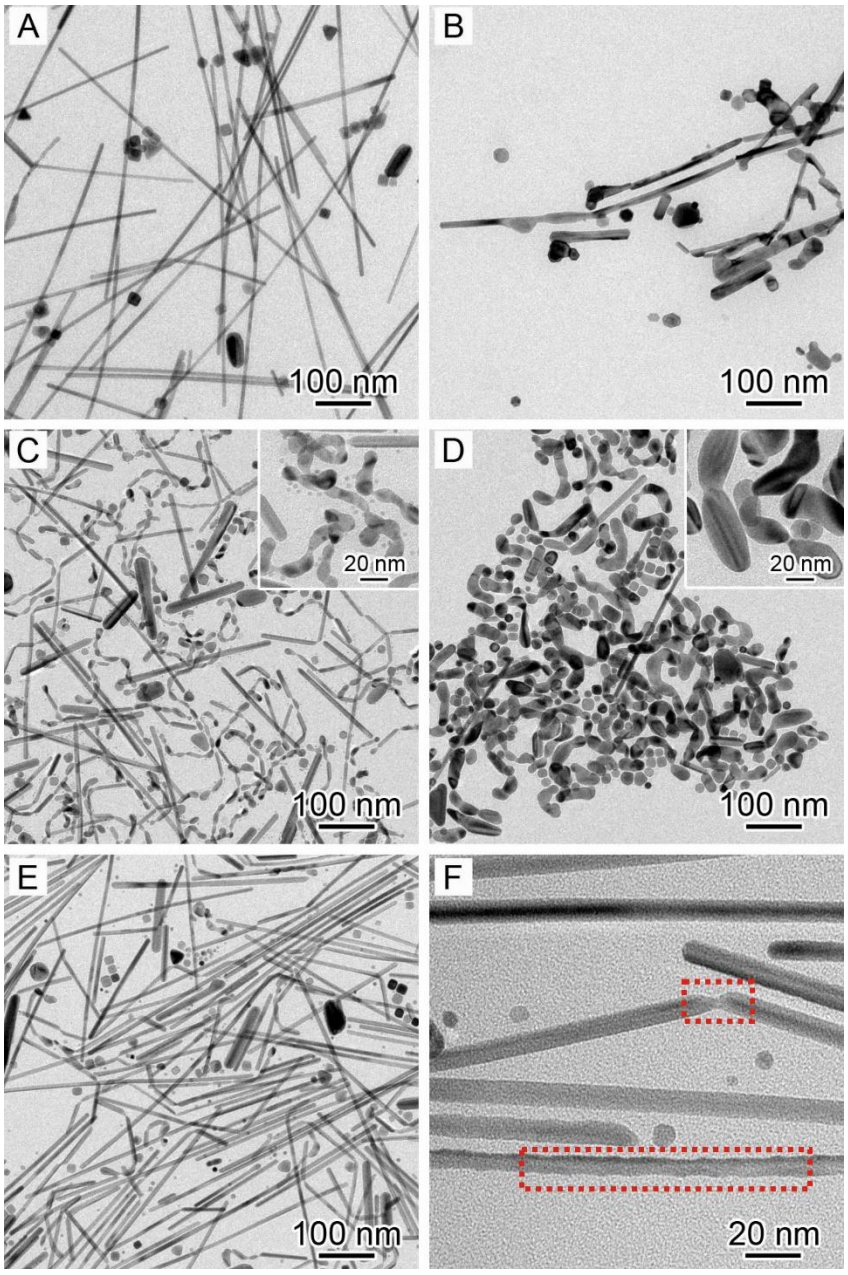

Figure 5.10. TEM images of the products obtained by aging the Pd nanowires at 160 ºC. The nanowires were dispersed in different solutions and aged under various conditions: (A, B) in DEG containing PVP (15 mg/mL) for 4 and 12 h, respectively; (C, D) in DEG containing NaI (50 mg/mL), PVP (15 mg/mL), and HCl (30 mM) for 10 and 60 min, respectively; (E) in DEG containing NaI (50 mg/mL), PVP (15 mg/mL), and HCl (30 mM) for 60 min, with argon being bubbled into the solution; (F) TEM image of the product shown in (E) at a higher magnification. The dashed boxes in (F) highlight the roughened side surface and fragmentation of the Pd nanowires caused by the aging.

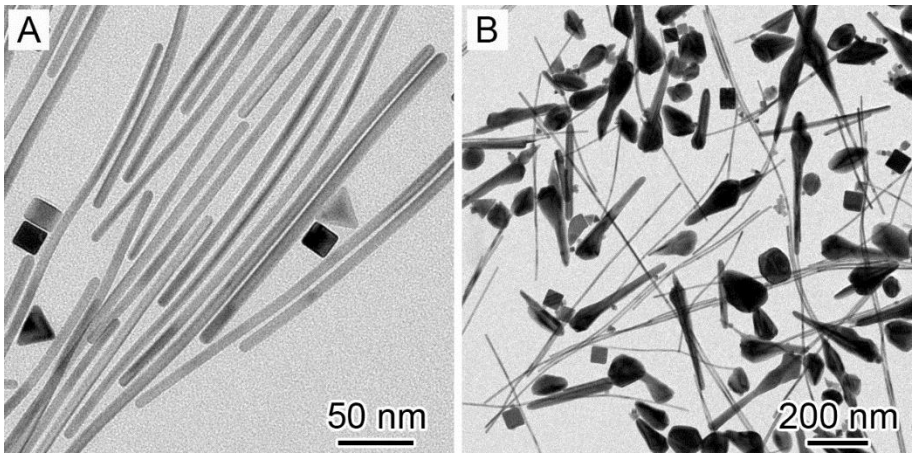

Figure 5.11. TEM images of Pd nanostructures obtained using the standard procedure at a different reaction temperature (150 ^{o}C) and for different reaction times: (A) 1 and (B) 6 h, respectively.

On the basis of experimental observations described above, we can propose a plausible mechanism for the time-dependent shape evolution of Pd nanowires. Pd nanorods are formed from initial decahedral nuclei, followed by their growth along the <110> direction into longer nanowires. At longer time periods, two reactions occur in solution. The first is the reduction of Pd^{2+} ions into Pd(0) atoms and their subsequent deposition onto the {111} facets at the ends of the Pd nanowires, which results in the longer nanowires observed in Figure 5.7C. The second is the fracturing of the Pd nanowires into smaller parts, such as nanorods, through oxidative etching. We expect that the newly formed fracture is enclosed by high-index facets, rather than the {111} facets found at the ends of standard nanowires. The preferential deposition of Pd at these high-energy sites serves to lower the total surface energy, resulting in the formation of a roughly spherical segment at the site of fracture. Upon further surface diffusion and Pd atom deposition the tadpole-like particle is subsequently created. Eventually, all of the nanowires are transformed into the irregular, twinned particles owing to the combination of oxidative etching, reduction of the released Pd^{2+} ions, and their deposition on the surface of the irregular particle, as shown in Figure 5.7D.

It is well known that the strength of oxidative etching is strongly correlated with the

reaction temperature [30]. Therefore, as the reaction temperature is decreased, the rate of oxidative etching should be observably slowed. On the basis of this argument, we carried out another series of experiments conducted at 150 ^{o}C to verify the proposed mechanism for the shape evolution of the Pd nanowires. As expected, Pd nanowires, with average length of 350 nm and average diameter of 8 nm, were obtained at t = 1 h, as shown in Figure 5.11A. After extending the reaction time to t = 6 h, Pd nanowires and tadpole-like particles were produced (Figure 5.11B). Because of the relatively slow rate of the oxidative etching at lower temperature, when compared to standard procedure, the Pd nanowires could be retained even after t = 6 h.

Evaluation of Electrocatalytic Properties. Based on previous reports, it is expected that the penta-twinned Pd nanowires should exhibit significant catalytic activity toward FAO owing to the existence of {100} facets and twin boundaries on the side faces [31–33]. we benchmarked the catalytic activity of the nanowires against a commercial Pd/C under identical measurement conditions (Table 5.1). Cyclic voltammograms (CVs) were recorded to characterize the catalytic activity of the catalysts. As shown by the Cu_{UPD} curves in Figure 5.12, there was a major difference in electrochemical behavior between the Pd nanowires and Pd/C. For the nanowires, a single peak appeared at 0.56 V, corresponding to the Cu_{UPD} on Pd(100) facets [34]. The polycrystalline Pd/C showed multiple peaks due to the presence of different types of facets on the surface [34]. We derived the electrochemically active surface areas (ECSAs), of these catalysts to be 10.7 and 67.0 m^2 g_{Pd}^{-1}, respectively, by integrating the stripping charges for Cu_{UPD} (420 and 460 μC cm^{-2} for the Pd nanowires and Pd/C, respectively) [34].

Table 5.1. Comparison of the catalytic activities of the Pd nanowires and commercial Pd/C toward the formic acid oxidation reaction.

Catalysts	$ECSA_{Cu}$ ($m^2\ g_{Pd}^{-1}$)	Anodic potential peak (V)	SA at the anodic potential ($mA\ cm^{-2}$)
Pd nanowires	10.7	0.51	2.45
Commercial Pd/C	67.0	0.47	0.78

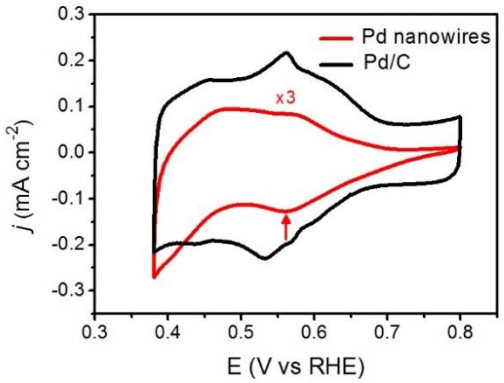

Figure 5.12. CVs of the Pd nanowires (red), and commercial Pd/C (black), which were recorded at room temperature in a N_2-saturated aqueous solution containing 0.05 M H_2SO_4 and 0.05 M $CuSO_4$ at a scan rate of 5 mV s^{-1}. The currents were normalized to the geometric area of the glassy carbon electrode (0.07065 cm^2).

Figure 5.13 shows the CVs of these two catalysts for FAO. The specific activity (SA, *j* / mA cm^{-2}) was normalized to the ECSA of the catalyst derived from the Cu_{UPD} charges. The potential peaks for the Pd nanowires and Pd/C were positioned at 0.51 and 0.47 V, with specific current densities of 2.45 and 0.78 mA cm^{-2}, respectively (Table 5.1). We also conducted a stability test of the Pd nanowires and Pd/C in a solution containing 0.5 M HCOOH and 0.5 M $HClO_4$ for 1,000 seconds with the potential fixed at 0.4 V. The chronoamperometric curves indicate that the initial and limiting currents of the Pd nanowires were both higher than those of the Pd/C (Figure 5.14). All of the electrocatalytic results reveal a greatly enhanced catalytic ability toward FAO for the Pd nanowires when compared with those of the commercial Pd/C.

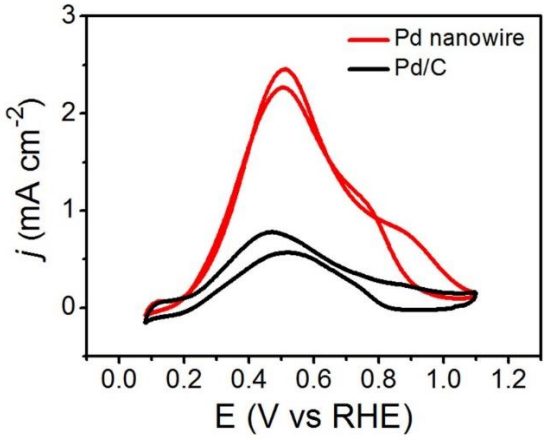

Figure 5.13. CVs of Pd nanowires (red) and a commercial Pd/C catalyst (black) for the FAO reaction recorded in a N_2-saturated aqueous solutions containing 0.5 M $HClO_4$ and 0.5 M HCOOH at a scan rate of 50 mV s^{-1}. The currents were normalized to their corresponding ECSAs.

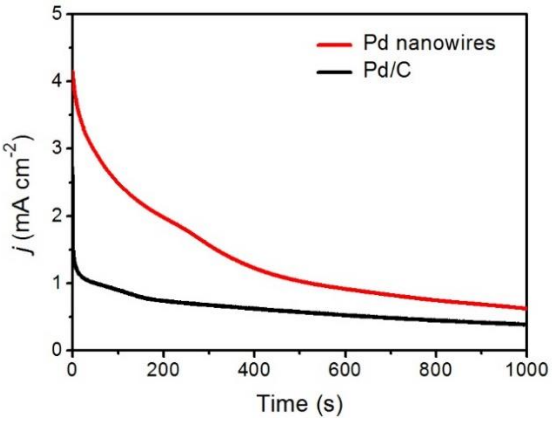

Figure 5.14. Chronoamperometric curves of the Pd nanowires and commercial Pd/C obtained in 0.5 M HCOOH and 0.5 M $HClO_4$ solution after 1,000 seconds. The potential was fixed at 0.4 V *vs.* RHE.

Syntheses of Pd@Pt Core-Sheath Nanowires and Pd-Pt Bimetallic Nanotubes. Pt-based one-dimensional nanostructures have been demonstrated as effective electrocatalysts towards the oxygen reduction reaction (ORR) [35–37]. However, it remains a challenge to produce Pt-based one-dimensional nanostructures. To this end, we employed the Pd nanowires, obtained using the standard procedure, as seeds to generate the Pd-Pt bimetallic one-dimensional nanostructures. The seeded overgrowth was conducted by injecting

Na_2PtCl_6 with a syringe pump into an EG-based mixture of PVP, AA, KBr, and Pd nanowires at 200 ºC (see experimental section for details). As shown in Figure 5.15A, bimetallic nanowires with an average diameter of 10.3 nm were obtained. The thicker diameter of the bimetallic nanowires corresponds to the deposition of Pt shells onto the surface of the Pd nanowires. EDX-mapping shown in Figure 5.15B confirms the formation of Pd@Pt core-sheath nanowires. Since Pt is more resistant to chemical oxidation when compared to Pd, we could selectively remove the Pd from the Pd@Pt core-sheath nanowires by using the Fe^{3+}/Br^- etchant pair (see experimental section for details). As shown in Figures 5.15C and D, hollow nanotubes were obtained after selectively etching the Pd cores from the Pd@Pt core-sheath nanowires. The composition of the nanotubes was subsequently determined by ICP-MS. As shown in Table 5.2, the significantly lower weight percentage of Pd in the final nanotubes, when compared to the initial nanowires, demonstrates the selective removal of Pd from the Pd@Pt core-sheath nanowires. Notably, a significant amount of Pd was retained in the nanotubes after etching, suggesting the formation of a Pd-Pt alloyed shell. The inset in Figure 5.15D shows a HRTEM image captured at a section of a nanotube wall (marked by the dashed box in Figure 5.15D). The wall was composed of six atomic layers with a thickness of about 1.2 nm, which is the approximate thickness of the Pt shell deposited on the Pd nanowires.

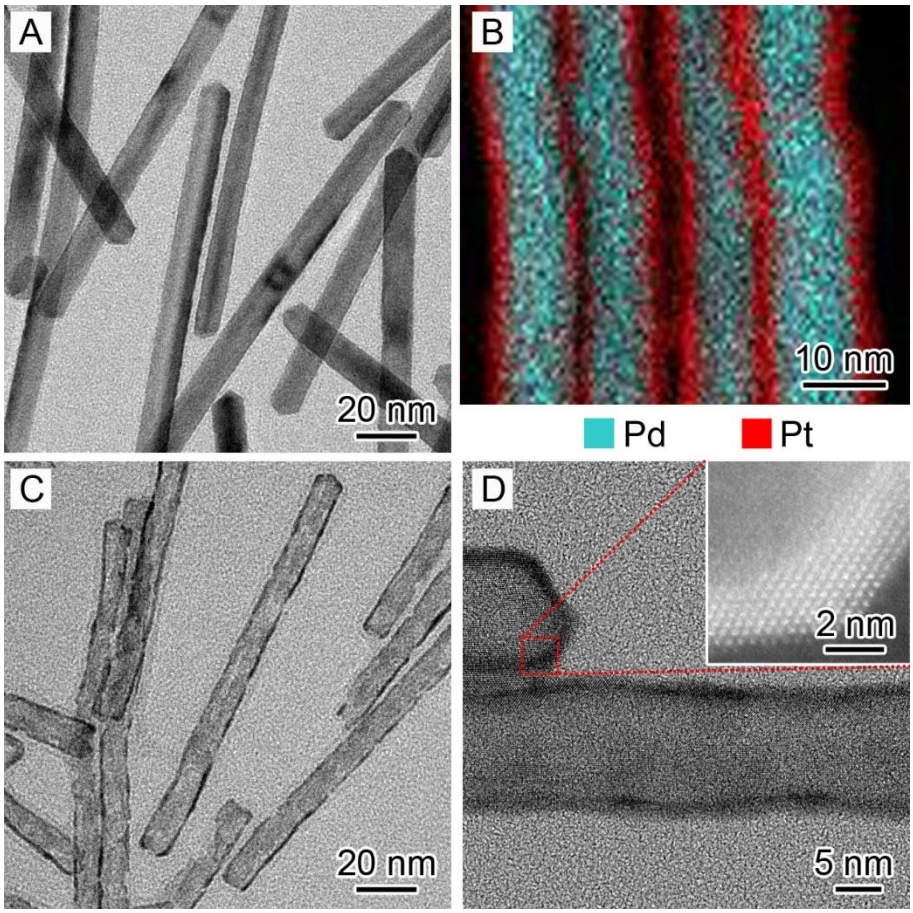

Figure 5.15. Morphological and compositional characterization of the Pd@Pt core-sheath nanowires, as well as the Pd-Pt nanotubes prepared by selectively etching away the Pd cores. (A) TEM image and (B) EDX mapping of the Pd@Pt core-sheath nanowires. (C) Low-magnification and (D) high-magnification TEM images of the Pt-based nanotubes. The inset in (D) shows a HRTEM image of the boxed region.

Table 5.2. The weight percentage (wt %) of Pd and Pt in the Pd@Pt core-sheath nanowires and Pd-Pt nanotubes calculated from ICP-MS data.

Sample	Wt % of Pd	Wt % of Pt
Pd@Pt core-sheath nanowires	49.79	50.21
Pd-Pt nanotubes	14.25	85.75

5.3 Conclusion

In summary, we have successfully synthesized ultrathin, penta-twinned Pd nanowires, with an average diameter of 7.8 nm and an average length of up to 720 nm using a one-pot approach. Adjusting the reduction rate of the Pd(II) precursor into the appropriate regime, in combination with Pd(100) capping by I^- ions, was found to be crucial to the success of such a synthesis. The Pd nanowires were found to evolve into irregular, multiply twinned particles if the reaction time was prolonged beyond 1.5 h. Further investigation revealed that this instability originated from oxidative etching induced by the O_2 from the air in combination with I^- ions. The as-prepared Pd nanowires were demonstrated to possess enhanced electrochemical catalytic activity toward the FAO. Finally, Pd@Pt core-sheath nanowires were synthesized by using the Pd nanowires as templates. Subsequent selective removal of Pd from these bimetallic structures produced well-defined Pd-Pt bimetallic nanotubes. We believe that the extensive understanding of the formation of Pd penta-twinned nanowires, as well as the facile approach to the production of Pd and Pd-Pt one-dimensional nanostructures, presented here can greatly advance the utility of noble-metal nanocrystals.

5.4 Experimental Section

Chemicals and Materials. Diethylene glycol (DEG, ≥99.0%, lot no. BCBK6125V), sodium tetrachloropalladate(II) (Na_2PdCl_4, 99.998%), hexachloroplatinate(IV) hexahydrate ($Na_2PtCl_6 \cdot 6H_2O$, 98.0%), poly(vinyl pyrrolidone) (PVP, $M_W \approx 55{,}000$), aqueous HCl solution (37 wt.% or 12 M), iron(III) chloride ($FeCl_3$, 97%), L-ascorbic acid (AA, ≥99.0%), sodium iodide (NaI, ≥99.5%), and potassium bromide (KBr, ≥99.0%) were all obtained from Sigma-Aldrich. Ethylene glycol (EG, lot no. K43B24) was purchased from J. T. Baker. All the chemicals were used as received. Deionized (DI) water with a resistivity of 18.2 MΩ·cm was used throughout the experiments.

Synthesis of Pd Nanowires in DEG. In a standard synthesis, 105 mg of PVP, 100 mg of AA, 100 mg of NaI, and 5 μL of aqueous HCl (12 M) were dissolved in 8 mL of DEG hosted in a 24-mL vial and heated at 160 °C in an oil bath for 15 min under magnetic stirring. Subsequently, 3 mL of DEG containing 30 mg Na_2PdCl_4 was added in one shot through a pipette. After the reaction had proceeded for 1 h, it was terminated by immersing the vial in an ice-water bath. Finally, the product was collected by centrifugation (12000 rpm, 10 min), washed with ethanol three times, and re-dispersed in water.

Synthesis of Pd@Pt Core-Sheath Nanowires. In a typical procedure, 2.0 mL of the Pd nanowires (0.20 mg/mL), 100 mg of AA, 66.6 mg of PVP, 54 mg of KBr, and 13 mL of EG were mixed in a 50 mL three-neck flask and heated at 110 °C for 15 min under magnetic stirring. The reaction temperature was then quickly ramped to 200 °C within 30 min. Meanwhile, 1.2 mg of $Na_2PtCl_6 \cdot 6H_2O$ was dissolved in 12 mL of EG and this solution was then injected into the flask using a syringe pump at a rate of 4 mL/h. After completion of the injection, the reaction mixture was kept at 200 °C for another 10 min. The reaction was quenched by immersing the flask in an ice bath. The products were collected by centrifugation (12000 rpm, 10 min), washed with ethanol three times, and re-dispersed in DI water.

Synthesis of Pt-based Nanotubes. In a typical process, 0.5 mL of the aqueous suspension of Pd@Pt core-sheath nanowires (0.48 mg/mL), 25 mg of $FeCl_3$, 0.15 mL of HCl (37%), 50 mg of PVP, 300 mg of KBr, and 7 mL of DI water were mixed in a 20 mL vial. The vial was then immersed in an oil bath held at 95 °C under magnetic stirring. After 2 h, the products were collected by centrifugation (12000 rpm, 10 min), washed with ethanol, and re-dispersed in water.

Kinetic Studies of the Pd Nanowire Synthesis. During a standard Pd nanowire synthesis, 100 μL aliquots were drawn with a micropipette in 5 min intervals over 1 h, with the first aliquot drawn immediately after the injection of the Na_2PdCl_4 precursor. The aliquots were thoroughly mixed with 1.4 mL of ice-cold aqueous NaI solution (200

mg/mL). The resultant mixture was centrifuged at 16500 rpm for 15 min to remove the solid product. 100 μL of the resultant supernatant was injected into 0.9 mL of aqueous NaI (200 mg/mL) inside a cuvette and the Pd(II) concentration was measured using UV-vis spectroscopy.

Electrochemical Measurements. The Pd nanowires (0.2 mg) or a commercial Pd/C (2.0 mg, 10 wt% of Pd) were dispersed in 1 mL of DI water and treated by ultrasonication for 10 min. The working electrode was prepared by drop-casting 10 μL of an aqueous suspension of the Pd catalysts onto a pre-cleaned, glassy carbon electrode (Bioanalytical Systems Inc.). Upon drying in an oven at 50 ^{o}C for 10 min, the electrode was covered with 5 μL of Nafion aqueous solution (0.05%) and allowed to dry in the same oven for another 10 min. The electrode was then treated with plasma etching for 30 min to remove the surfactants remaining on the Pd nanowires. An Ag/AgCl electrode and a Pt mesh were used as the reference and counter electrodes, respectively. All potentials are given with reference to the reversible hydrogen electrode (RHE). Prior to electrochemical measurements, the samples loaded on electrodes were cycled between 0.08 and 1.5 V for 50 cycles in a N_2-saturated aqueous solution containing $HClO_4$ (0.1 M) at a scan rate of 50 mV s^{-1} to remove the surface ligand such as I^- ions. The activity of each catalyst for FAO was obtained by cycling the potential between 0.08 and 1.1 V for 3 cycles in a N_2-saturated aqueous solution containing $HClO_4$ (0.5 M) and HCOOH (0.5 M) at a scan rate of 50 mV s^{-1}. The CV for Cu underpotential deposition (Cu_{UPD}) was obtained in an aqueous solution containing H_2SO_4 (0.05 M) and $CuSO_4$ (0.05 M) at a scan rate of 5 mV s^{-1}.

Instrumentation. The X-ray diffraction (XRD) patterns were obtained on a diffractometer (Paralytical XRD-600) operated at 40 kV and 40 mA with filtered Cu Kα radiation at λ=0.154 nm. The transmission electron microscopy (TEM) images were obtained using a Hitachi HT7700 microscope operated at 120 kV. The high-resolution TEM (HRTEM) and high-angle annular dark-field scanning TEM (HAADF-STEM) images were acquired using a JEOL JEM 2200FS STEM/TEM microscope equipped with a CEOS

(Heidelberg, Germany) probe corrector to provide a nominal image resolution of 0.07 nm. Elemental analysis of products was conducted using an inductively-coupled plasma mass spectrometer (ICP-MS, Perkin Elmer, NexION 300Q). UV-Vis absorption spectra were recorded with a Lambda 750 spectrometer (PerkinElmer). Cyclic voltammograms (CVs) were obtained with CHI 600E potentiostat (CH Instruments, USA).

5.5 Notes to Chapter 5

Part of this chapter is adapted from the paper "Rational Design and Successful Execution of a Protocol for the One-Pot Synthesis of Pd Penta-Twinned Nanowires" to be submitted for publication.

5.6 References

[1] Rice, C.; Ha, S.; Masel, R. I.; Waszczuk, P.; Wieckowski, A.; Barnard, T. *J. Power Source* **2002**, *111*, 83–89.

[2] Rice, C.; Ha, S.; Masel, R. I.; Wieckowski, A. *J. Power Source* **2003**, *115*, 229–235.

[3] Zhang, H.; Jin, M.; Xiong, Y.; Lim, B.; Xia, Y. *Acc. Chem. Res.* **2013**, *46*, 1783–1794.

[4] Xia, Y.; Xiong, Y.; Lim, B.; Skrabalak, S. E. *Angew. Chem., Int. Ed.* **2009**, *48*, 60–103.

[5] Habas, S. E.; Lee, H.; Radmilovic, V.; Somorjai, G. A.; Yang, P. *Nature Mater.* **2007**, *6*, 692–697.

[6] Wang, Y.; Xie, S.; Liu, J.; Park, J.; Huang, C. Z.; Xia, Y. *Nano Lett.* **2013**, *13*, 2276–2281.

[7] Chang, G.; Oyama, M.; Hirao, K. *Acta Mater.* **2007**, *55*, 3453–3456.

[8] Jin, M.; Liu, H.; Zhang, H.; Xie, Z.; Liu, J.; Xia, Y. *Nano Res.* **2011**, *4*, 83–91.

[9] Niu, W.; Zhang, L.; Xu, G. *ACS Nano* **2010**, *4*, 1987–1996.

[10] Xia, X.; Choi, S.; Herron, J. A.; Lu, N.; Scaranto, J.; Peng, H.; Wang, J.; Mavrikakis, M.; Kim, M. J.; Xia, Y. *J. Am. Chem. Soc.* **2013**, *135*, 15706–15709.

[11] Huang, H.; Wang, Y.; Ruditskiy, A.; Peng, H.-C.; Zhao, X.; Zhang, L.; Liu, J.; Ye, Z.; Xia, Y. *ACS Nano* **2014**, *8*, 7041–7050.

[12] Li, C.; Sato, R.; Kanehara, M.; Zeng, H.; Bando, Y.; Teranishi, T. *Angew. Chem., Int. Ed.* **2009**, *48*, 6883–6887.

[13] Huang, X.; Zheng, N. *J. Am. Chem. Soc.* **2009**, *131*, 4602–4603.

[14] Lu, N.; Chen, W.; Fang, G.; Chen, B.; Yang, K.; Yang, Y.; Wang, Z.; Huang, S.; Li, Y. *Chem. Mater.* **2014**, *26*, 2453–2459.

[15] Ruditskiy, A.; Peng, H.-C.; Xia, Y. *Annu. Rev. Chem. & Biomol. Eng.* **2016**, *7*, 327−348.

[16] Elechiguerra, J. L.; Reyes-Gasga, J.; Yacaman, M. J. *J. Mater. Chem.* **2006**, *16*, 3906–3919.

[17] Sun, Y.; Gates, B.; Mayers, B.; Xia, Y. *Nano Lett.* **2002**, *2*, 165–168.

[18] Ruditskiy, A.; Zhao, M.; Gilroy, K.D.; Vara, M.; Xia, Y. *Chem. Mater.* 2016, *28*, 8800–8806.

[19] Huang, H.; Zhang, L.; Lv, T.; Ruditskiy, A.; Liu, J.; Ye, Z.; Xia, Y. *ChemNanoMat* **2015**, *1*, 246–252.

[20] Luo, M.; Huang, H.; Choi, S.-I.; Zhang, C.; Silva, R. R.; Peng, H.-C.; Li, Z.-Y.; Liu, J.; He, Z.; Xia, Y. *ACS Nano* **2015**, *9*, 10523–10532.

[21] Luo, M.; Ruditskiy, A.; Peng, H.-C.; Tao, J.; Figueroa-Cosme, L.; He, Z.; Xia, Y. *Adv. Funct. Mater.* **2016**, *26*, 1209–1216.

[22] Johnson, C. J.; Dujardin, E.; Davis, S. A.; Murphy, C. J.; Mann, S. *J. Mater. Chem.* **2002**, *12*, 1765–1770.

[23] Jin, M.; He, G.; Zhang, H.; Zeng, J.; Xie, Z.; Xia, Y. *Angew. Chem., Int. Ed.* **2011**, *50*, 10560–10564.

[24] Wang, Y.; Peng, H.-C.; Liu, J.; Huang, C. Z.; Xia, Y. *Nano Lett.* **2015**, *15*, 1445–

1450.

[25] Griffith, W.P.; Robinson, S.D.; Swars, K. *Gmelin Handbook of Inorganic Chemistry, 8th Edition, Supplement Volume B 2, Pd Compounds*, Springer-Verlar, Berlin, Heidelberg, **1989**, 208–210.

[26] Achard, T.; Benet-Buchholz, J.; Escudero-Adan, E. C.; Riera, A.; Verdaguer, X. *Organometallics* **2011**, *30*, 3119–3130.

[27] Wang, C.; Wang, L.; Long, R.; Ma, L.; Wang, L.; Li Z.; Xiong, Y. *J. Mater. Chem.* **2012**, *22*, 8195–8198.

[28] Liu, M.; Zheng, Y.; Zhang, L.; Guo, L.; Xia, Y. *J. Am. Chem. Soc.* **2013**, *135*, 11752–11755.

[29] Xiong, Y.; Chen, J.; Wiley, B.; Xia, Y. *J. Am. Chem. Soc.* **2005**, *127*, 7332–7333.

[30] Zheng, Y.; Zeng, J.; Ruditskiy, A.; Liu, M.; Xia, Y. *Chem. Mater.* **2014**, *26*, 22−33.

[31] Lv, T.; Wang, Y.; Choi, S.; Chi, M.; Tao, J.; Pan, L.; Huang, C. Z.; Zhu, Y.; Xia, Y. *ChemSusChem* **2013**, *6*, 1923–1930.

[32] Jin, M.; Zhang, H.; Xie, Z.; Xia, Y. *Energy Environ. Sci.* **2012**, *5*, 6352–6357.

[33] Choi, S.-I.; Herron, J. A.; Scaranto, J.; Huang, H.; Wang, Y.; Xia, X.; Lv, T.; Park, J.; Peng, H.-C.; Mavrikakis, M.; Xia, Y. *ChemCatChem* **2015**, *7*, 2077–2084.

[34] Shao, M.; Odell, J.; Humbert, M.; Yu, T.; Xia, Y. *J. Phys. Chem. C* **2013**, *117*, 4172–4180.

[35] Jiang, S.; Ma, Y.; Jian, G.; Tao, H.; Wang, X.; Fan, Y.; Lu, Y.; Hu, Z.; Chen, Y. *Adv. Mater.* **2009**, *21*, 4953–4956.

[36] Guo, S.; Dong, S.; Wang, E. *Energy Environ. Sci*. **2010**, *3*, 1307–1310.

[37] Koenigsmann, C.; Santulli, A. C.; Gong, K.; Vukmirovic, M. B.; Zhou, W.; Sutter, E.; Wong, S. S.; Adzic, R. R. *J. Am. Chem. Soc.* **2011**, *133*, 9783–9795.

CHAPTER 6

CONCLUSIONS AND FUTURE DIRECTIONS

6.1 Conclusions

This dissertation covers a number of strategies for controlling the size and shape of noble-metal nanocrystals. I began by developing a polyol-based method for generating well-defined Ag nanocubes with edge lengths below 15 nm. The success of this method relied on a combination of the effective capping of small Ag{100} facets by Br^- ions and control over the number of nuclei initially formed in the reaction system. The latter was enabled by a new understanding of the mechanistic effects of SH^- additives, achieved over the course of this work. The substitution of HCl by NaCl as the chloride source, improved upon previous synthetic methods, greatly enhancing the effectiveness of the SH^- additive in controlling the nucleation of Ag atoms. As a result, the variation of SH^- concentration was shown to be the most effective means for controlling the edge length of Ag nanocubes. The Br^- ions acted both as a capping agent toward the Ag(100) surface, and as a kinetic regulator by limiting the number of free Ag^0 atoms present in the reaction solution. The resultant Ag nanocubes are both smaller and sharper at corners/edges when compared with those reported in previous work. The edge length of the nanocubes could be readily varied from 13 to 23 nm by quenching the synthesis after different periods of growth. The nanocube yield was estimated to be ~90%, and subsequent experiments have shown this approach to be both highly reproducible and readily scalable.

Next, I carried out a systematic, quantitative study of the sulfate-mediated polyol synthesis of Pd decahedra. ICP-MS characterization of the various product fractions revealed that only 26% of the initial Pd precursor was converted into the collected decahedra, with the rest lost to the discarded smaller particles and unreacted precursor. TEM analysis of the products sampled at different reaction times suggested that the size

distribution was likely due to the coalescence of some of the initially formed nuclei during the first few minutes of the synthesis. This data, combined with the information gathered from a kinetic study, allowed me to propose a mechanism to account for the formation of Pd decahedra. Building on these mechanistic insights, I was able to increase the yield of the collected decahedra to ~67% by introducing ascorbic acid as a second reducing agent meant to rapidly consume the unreacted precursor, thus growing the smaller Pd particles into the desired decahedra.

My coworkers and I applied the knowledge gained during the above studies to synthesize ultrathin, penta-twinned Pd nanowires, with an average diameter of 7.8 nm and an average length of up to 720 nm using a one-pot approach. Adjusting the reduction rate of the Pd(II) precursor into the appropriate regime, in combination with Pd(100) capping by I^- ions, was found to be crucial to the success of a nanowire synthesis. The Pd nanowires were found to evolve into irregular, multiply twinned particles if the reaction time was prolonged beyond 1.5 h. Further investigation revealed that this instability originated from oxidative etching induced by the O_2 from the air in combination with I^- ions. The as-prepared Pd nanowires were demonstrated to possess enhanced electrochemical catalytic activity toward the formic acid oxidation. Furthermore, Pd@Pt core-sheath nanowires were synthesized by using the Pd nanowires as templates. Subsequent selective removal of Pd from these bimetallic structures produced well-defined Pd-Pt bimetallic nanotubes.

Finally, I carried out a systematic study to understand the oxidative etching of Pd decahedral nanocrystals by the O_2/I^- pair under different conditions. Electron microscopy analyses of the etched particles revealed significant rounding of the penta-twinned decahedra due to the removal of atoms from the equatorial vertices and edges. It was found that the etching began from the equatorial vertices, with the formation of re-entrant grooves, and then proceeded along the equatorial edges by removing the low-coordination Pd atoms until a rounded structure was attained. The etching behaviors in DEG and DI water differed significantly, with the former producing rounded particles and the latter

preserving the initial shape. The addition of a sufficient amount of AA into the water-based system resulted in the formation of rounded structures, revealing the need for an adequately reducing environment in order to initiate oxidative etching. This phenomenon could be attributed to the presence of a protective oxide layer on the surface of the Pd decahedra, which had to be removed first through reduction before etching could occur. Moreover, I utilized the rounded particles as seeds for the growth of pentagonal Pd nanorods with asymmetric, tapered structures, due to the involvement of both axial and radial growth.

My research has advanced the understanding of the impacts of trace additives, reaction kinetics, and oxidative etching on the size and shape evolution of colloidal noble-metal nanocrystals. The mechanistic insights contribute to the rational design of synthetic protocols and further improve the commercial viability of these nanomaterials.

6.2 Future Directions

The mechanistic strategies described in this dissertation seek to guide the evolution of noble-metal nanocrystals by controlling atomic nucleation, growth, and oxidative etching. Despite these accomplishments, a number of open questions remain.

Firstly, it is often difficult to disentangle the influence of additives on surfaces capping from their impact on reduction kinetics. For example, in the synthesis of Pd nanowires described in Chapter 4, I^- ions acted as both the capping agent for the Pd(100) surface and a means to slow the reduction kinetics through the formation of the PdI_4^{2-} complex. However, the relative impacts of these factors on the growth of the nanowires could not be resolved. These issues can be avoided by performing nanocrystal syntheses on substrates without the presence of growth-directing capping agents, while controlling kinetics. This method has been successfully used to prepare a number of nanocrystal morphologies, ranging from prisms to nanoframes, composed of a wide range of noble-metal compositions [1−3].

The dependence of internal twin structure of seeds on the initial reduction kinetics has

been one of the most interesting recent developments in the field nanocrystal shape control [4]. This method should be systematically applied to the syntheses of Pd nanocrystals with other shapes, such as right bipyramids [5]. Furthermore, it would be interesting to compile such correlation maps for other metals, such as Ag, Au, and Pt, in order to understand the broader impact of in the kinetic control over the seed structure across different elements.

Frequently, mechanistic hypotheses are formed based on the observed initial components and final products only, without any information with regard to the intermediate structures and their temporal transformation. The development of *in situ* TEM techniques will allow researchers to gain those crucial insights. For instance, Alivisatos *et al.* performed a set of experiments by observing the *in situ* oxidative etching of various Au nanocrystals inside a graphene pocket [6]. Notably, they observed a non-equilibrium intermediate during the etching of a Au nanocube, before the intermediate was etched away to generate the expected spherical particle. Further development in microscopy techniques may shed new light on what we used to think of as well-understood systems [7, 8].

Developing etching methods that do not rely on the relative free energies of surface atoms for targeting would significantly increase the usefulness of oxidative etching. Qin *et al.* demonstrated that a H_2O_2 etchant can be produced by enzymes affixed to the surface of a Ag nanocube [9]. Further development of methods for attaching such moieties to specific sites of the surface, such as edges or particular facets, as well as controlling the local etchant concentration, would provide a more precise and powerful tool for carving at the nanoscale. Finally, it may be prudent to move beyond wet chemistry as a means to facilitate oxidative etching. For example, the work by Ling *et al.* has shown that galvanic replacement can be initiated under dry conditions by using an elastomer stamp infused with etchant metal ions [10].

6.3 Notes to Chapter 6

Parts of this chapter are adapted from "The Science and Art of Carving Metal Nanocrystals" published in *ACS Nano* [11], "Toward the Synthesis of Sub-15 nm Ag Nanocubes with Sharp Corners and Edges: The Roles of Heterogeneous Nucleation and Surface Capping" published in the *Journal of the American Chemical Society* [12], and "Toward a Quantitative Understanding of the Sulfate-mediated Synthesis of Pd Decahedral Nanocrystals with High Conversion and Morphology Yields" published in the *Chemistry of Materials* [13].

6.4 References

[1] Gilroy, K. D.; Farzinpour, P.; Sundar, A.; Hughes, R. A.; Neretina, S. *Chem. Mater.* **2014,** *26*, 3340−3347.

[2] Hajfathalian, M.; Gilroy, K. D.; Hughes, R. A.; Neretina, S. *Small* **2016**, *12*, 3444−3452.

[3] Gilroy, K. D.; Sundar, A.; Hajfathalian, M.; Yaghoubzade, A.; Tan, T. Sil, D.; Borguet, E.; Hughes, R. A.; Neretina, S. *Nanoscale* **2015**, *7*, 6827−6835.

[4] Wang, Y.; Peng, H.-C.; Liu, J.; Huang, C.Z.; Xia, Y. *Nano Lett.*, **2015**, *15*, 1445–1450.

[5] Xia, X.; Choi, S.-I.; Herron, J. A.; Lu, N.; Scaranto, J.; Peng, H.-C.; Wang, J.; Mavrikakis, M.; Kim, M. J.; Xia, Y. *J. Am. Chem. Soc.* **2013**, *135*, 15706–15709.

[6] Ye, X.; Jones, M.R.; Frechette, L.B.; Chen, Q.; Powers, A.S.; Ercius, P.; Dunn, G.; Rotskoff, G.M.; Nguyen, S.C.; Adiga, V.P.; Zettl, A.; Rabani, E.; Geissler, P. L.; Alivisatos, A. P. *Science* **2016**, *354*, 874−877.

[7] Jiang, Y.; Zhu, G.; Lin, F.; Zhang, H.; Jin, C.; Yuan, J.; Yang, D.; Zhang, Z. *Nano Lett.* **2014**, *14*, 3761−3765.

[8] Jungjohann, K. L.; Bliznakov, S.; Sutter, P. W.; Stach, E. A.; Sutter, E. A. *Nano*

Lett., **2013**, *13*, 2964–2970.

[9] Wang, C.-W.; Sun, X.; Chang, H.-T.; Qin, D. *Chem. Mater.* **2016**, *28*, 7519−7527.

[10] Zhang, Q.; Lee, Y. H.; Phang, I.Y.; Pedireddy, S.; Tjiu, W. W.; Ling, X. Y *Langmuir*, **2013**, *29*, 12844−12851.

[11] Ruditskiy, A.; Xia, Y. *ACS Nano*, **2017**, *11*, 23–27.

[12] Ruditskiy, A.; Xia, Y. *J. Am. Chem. Soc.* **2016**, *138*, 3161–3167.

[13] Ruditskiy, A.; Zhao, M.; Gilroy, K. D.; Vara, M.; Xia, Y. *Chem. Mater.* **2016**, *28*, 8800–8806.